Optofluidic dye Lasers

Gersborg-Hansen, Morten

Publication date:
2008

Document Version
Publisher's PDF, also known as Version of record

Optofluidic dye lasers

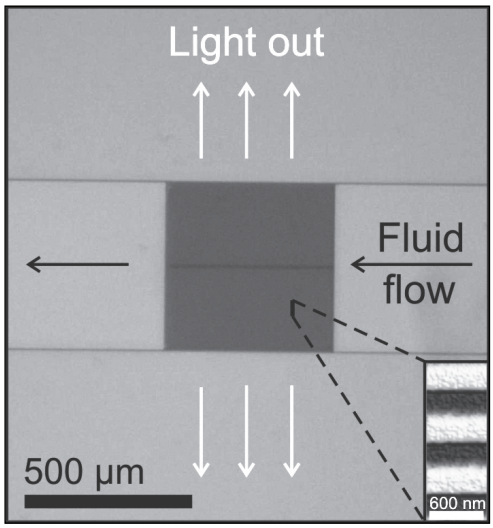

Morten Gersborg-Hansen
Ph.D. Thesis

Department of Micro- and Nanotechnology
Technical University of Denmark

December 14, 2007

ABSTRACT

In recent years, the field of optofluidics has emerged as a combination of microfluidics and optics. In this thesis, the author investigates optofluidic dye lasers suitable for lab-on-a-chip applications. In particular, distributed feedback (DFB) laser resonators are promising candidates for obtaining low threshold and tunable lasing.

In this work, optofluidic dye lasers have been designed, fabricated, characterized, and modeled. The basic underlying theory of planar waveguiding and DFB lasers is presented and a transmission matrix model for the design of optofluidic DFB lasers is described. Finite element method simulations are used to study the cavity modes of an optofluidic dye ring laser.

The fabricated optofluidic DFB dye lasers are based on a nanostructured SU-8 polymer film and a third order DFB laser resonator with a central $\pi/2$ phase shift. The devices are fabricated by fast and flexible combined electron beam and UV lithography in SU-8 and adhesive polymer wafer bonding. The materials used allow for potentially cheap wafer-scale fabrication.

For the characterization, the laser dye rhodamine 6G is dissolved in a liquid and the laser resonator is filled by capillary action, omitting the need for external fluidic handling apparatus. By employing a third order DFB laser resonator, (i) narrow linewidth emission (< 0.15 nm), (ii) low laser thresholds down to ~ 7 μJ/mm^2, and (iii) a large tunability are obtained. A wavelength tunability of 45 nm is achieved by changing the grating period and through optofluidic functionality by altering the liquid refractive index.

In addition, a novel dye replenishment mechanism to compensate for dye bleaching in optofluidic dye lasers based on diffusion is demonstrated. When pumping only a small fraction of the available dye solution through a narrow slit, the lifetime of an optofluidic light source is dramatically increased due to diffusion compared to a pumping configuration where the entire volume of dye solution is homogeneously pumped. The results potentially allow for a significant simplification of optofluidic dye laser device layouts.

Optofluidic dye lasers are easily integrated with waveguides and microfluidic components and may be applied in chemical or biochemical lab-on-a-chip systems or in adaptive optics where narrow linewidth and widely tunable visible light is desired.

RESUMÉ

I løbet af de senere år er forskningsfeltet optofluidik opstået som en kombination af mikrofluidik og optik. I denne afhandling undersøger forfatteren optofluide farvestoflasere, som er velegnede til anvendelser indenfor lab-on-a-chip teknologi. Laserresonatorer med distribueret feedback (DFB) har vist sig at være lovende kandidater til at opnå lasing med lav tærskel og mulighed for tuning.

Dette arbejde har bestået i at designe, fabrikere, karakterisere og modellere optofluide farvestoflasere. Grundlæggende teori vedrørende planare bølgeledere og DFB lasere præsenteres og en transmissionsmatricemodel til design af optofluide DFB lasere beskrives. Simulationer med den endelige element metode bruges til at studere de optiske tilstande i en optofluid ring-laser.

De fabrikerede optofluide DFB farvestoflasere er baseret på en nanostruktureret SU-8 polymerfilm og en tredje ordens DFB laserresonator med et centralt $\pi/2$ faseskift. Komponenterne blev fabrikeret med hurtig og fleksibel kombineret elektronstråle- og UV-litografi og efterfølgende forseglet vha. en klæbende polymer. De anvendte materialer tillader potentielt set billig wafer-skala fabrikation.

For at karakterisere komponenterne blev laserresonatoren fyldt vha. kapillærkræfter med en væske indeholdende laserfarvestoffet rhodamin 6G. Derved afskaffes behovet for apparatur til ekstern væskehåndtering. Ved at anvende en tredje ordens DFB laserresonator opnås (i) emission af lys med smal linjebredde (< 0.15 nm), (ii) lav lasertærskel ned til ~ 7 μJ/mm^2 og (iii) stor tunebarhed. Bølgelængden blev tunet 45 nm ved at ændre gitterets periode og ved at skifte brydningsindekset af væsken.

Derudover demonstreres en ny mekanisme, baseret på diffusion, til at komplettere farvestoffet for at kompensere for blegning i optofluide farvestoflasere. Når blot en lille brøkdel af den tilgængelige farvestofopløsning pumpes optisk gennem en smal spalte, forøges levetiden af en optofluid lyskilde dramatisk sammenlignet med homogen pumpning.

Optofluide farvestoflasere integreres let med bølgeledere og mikrofluide komponenter og kan finde anvendelser indenfor kemiske og biokemiske lab-on-a-chip systemer eller indenfor adaptiv optik – hvorend synligt lys med smal linjebredde og gode muligheder for tuning ønskes.

PREFACE

This thesis is submitted in partial fulfillment of the requirements for obtaining the degree of Philosophiae Doctor (Ph.D.) at the Technical University of Denmark (DTU). The thesis presents my work during the last 3 years as a Ph.D. student in the Optofluidics group at MIC – Department of Micro and Nanotechnology. The Ph.D. project was financed by DTU and the work was carried out at DTU; at MIC and at the DANCHIP clean room facility.

I gratefully acknowledge the help and support from my enthusiastic supervisor Assoc. Prof. Anders Kristensen with whom I have had many stimulating discussions both at MIC and under the palm trees in Europe and the U.S. I also thank him for introducing me to the art of sushi.

I thank the Optofluidics Vikings, everybody at MIC, the DANCHIP staff, and the Friday Bar for providing a pleasant and constructive working environment. In particular, I acknowledge past and present Ph.D. students in the Optofluidics Vikings, especially my officemates Theodor Nielsen and Fredrik Persson and the laser-dudes Søren Balslev and Mads Brøkner Christiansen, with whom I have tried to unravel the mysteries of optofluidic dye lasers.

Lasse Højlund Thamdrup and Andrej Mironov are acknowledged for their work during a special course project on nanoimprint lithography which has contributed to this project. Niels Asger Mortensen is gratefully acknowledged for stimulating discussions on and insight in the theoretical aspects of optofluidics.

For proofreading of the thesis and rock-solid support I am in debt to Malene Erup Larsen. Allan Roulund Gersborg is saluted for proofreading and good brotherhood. I thank my family and friends for supporting me throughout the project.

Finally, Otto Mønsteds Fond and Familien Hede Nielsens Fond are acknowledged for travel support, making it possible for me to attend and present my results at a number of international conferences.

Morten Gersborg-Hansen
December 14, 2007

CONTENTS

Abbreviations

AFM	atomic force microscope
CEUL	combined electron beam and UV lithography
DFB	distributed feedback
EBL	electron beam lithography
FD-BPM	finite difference beam propagation method
FEM	finite element method
FSR	free spectral range
IPA	iso-propyl alcohol
NIL	thermal nanoimprint lithography
PDMS	polydimethylsiloxane
PGMEA	propylene glycol monomethyl ether acetate
PMMA	polymethylmethacrylate
R6G	rhodamine 6G
SEM	scanning electron microscope
cf.	compare with (latin: confer)
e.g.	for example (latin: exempli gratia)
et al.	and others (latin: et alii)
i.e.	that is (latin: id est)

Notation

c	scalar quantity (italic), e.g. the speed of light
$\mathbf{E}$	vector quantity (boldface), e.g. the electric field
$\hat{\mathbf{T}}$	matrix quantity, e.g. a transmission matrix

1. INTRODUCTION

1.1 Lab-on-a-Chip systems

Devices and consumer products that rely on functionality on the micrometer-scale have in recent years penetrated our everyday life. The advancement of microfabrication techniques pushed forward by the semiconductor industry has enabled the realization of micro-electromechanical systems (MEMS). An example is pressure sensors based on silicon membranes with electrical readout which have been applied in microphones for mobile telephones. Another example is miniaturized accelerometers applied in air-bag sensors based on microfabricated cantilevers. MEMS technology is also applied in ink-jet printer heads for rapid and reproducible forming of ink droplets.

The application of microsystems for chemical sensing was proposed in 1990 by Manz *et al.* [1]. The idea of such a miniaturized total analysis system, or lab-on-a-chip system, is to miniaturize and integrate all elements needed to perform a certain chemical analysis onto a single microfluidic chip. There are several advantages of lab-on-a-chip systems: (i) They are compact and hence portable compared to standard laboratory apparatus, i.e. the analysis may be carried out at the point-of-care, (ii) the polymer materials typically used are cost-effective compared to semiconductor materials, (iii) diffusion dominates the reaction dynamics, and (iv) only a small sample volume is needed which may prove an environmental advantage since this may reduce the required amount of hazardous compounds.

The role of diffusion is inherent to microfluidic systems where the diffusion constant of molecules in a solution remains constant when the dimensions of the fluidic system are scaled down. Thus the typical reaction time it takes for two molecular species to diffuse around until they collide and react is reduced dramatically [2]. Although lab-on-a-chip technology holds a large potential for widespread use in analysis and diagnostics in chemistry, biochemistry, environmental technology, and life sciences, a substantial effort is required for each new application in order to outperform existing technologies and enable profitable commercialization.

As examples of lab-on-a-chip systems, three products from the field of biotechnology are mentioned here. The first is the Agilent 2100 Bioanalyzer,

Fig. 1.1: Example of a successfully commercialized lab-on-a-chip system: Agilent 2100 Bioanalyzer electrophoresis system. From www.agilent.com

see Fig. 1.1, which is the first commercial microfluidics-based platform for the analysis of DNA, RNA, proteins, and cells. It provides good-quality data within 30 minutes and replaces labour-intensive gel-electrophoresis for a number of experiments, e.g. for measuring the purity and integrity of RNA samples and for protein expression analysis [2]. The success and reliability of the Agilent 2100 Bioanalyzer are reflected in the 4500 reference publications in which it has been cited since it was launched in 1999 and demonstrate the success of downscaling for chemical separation [2].

The second example is the Affymetrix GeneChip microarray system which is widely used worldwide. Semiconductor fabrication techniques are integrated with chemistry and molecular biology to create arrays with millions of probes for DNA-RNA hybridization experiments on a single device. By 2005 more than 4200 publications cited the use of the Affymetrix GeneChip in many different areas, e.g. sequence analysis and gene expression analysis, and for several organisms [2]. The Affymetrix GeneChip microarray system is the result of successful cross-disciplinary efforts yielding an efficient lab-on-a-chip system.

The final example is the eXpress Blood Counter from Chempaq in Denmark, founded in 1999 as a spin-off company from the Technical University of Denmark (DTU). By means of microfluidics and impedance measurements, the device is able to perform a cell-counting analysis of a patient's blood, counting five constituents using a single 20 µL drop of blood. The analysis is useful for diagnosis of patient infections and is performed within 3 minutes at the point-of-care.

1.2 What is optofluidics?

Following the advancement of microfluidics and microfabrication techniques in recent years, the multidisciplinary research field of optofluidics has emerged by integrating microfluidics with optical components and methods. By adding fluidics to optical devices, novel functionalities emerge that have not been achievable earlier. This has resulted in novel methods for creating reconfigurable devices and adaptive optical components. Recently, several review papers on the field of optofluidics have been published by Psaltis *et al.* [3], Monat *et al.* [4], and Levy and Shamai [5].

The advantages of applying microfluidics in optical devices include new possibilities with regards to tunability due to the wide range of refractive indices available compared to solid-state optical devices. Fluids can be mixed easily by on-chip mixing, thereby providing real-time tunability and modulation of optical signals [6]. Since viscous forces dominate over inertial forces in microfluidic systems, the flow is laminar and mixing is done by diffusion. Gain and absorption can be easily added to fluids by mixing in dyes (absorbing, amplifying, or non-linear), quantum dot materials, scattering particles, or other compounds of interest.

Liquid interfaces generally have smooth sidewalls which can provide low propagation losses for waveguide applications [7], and novel ways of tuning devices, e.g. by the thermo-optical effect [8], have been demonstrated. Optofluidic tuning can also be achieved by altering the optical path of the light, either by changing the physical path of the light or the refractive index experienced by the light, as it propagates through the device. Finally, modulation of the polarization state of the light provides means for optofluidic tuning.

The above-mentioned properties of optolfuidics illustrate the flexibility gained by introducing liquids into optical systems and hold a promise for novel adaptive optofluidic components in integrated systems. To illustrate the wide range of applications of optofluidics, four examples are reviewed here, see [3–5] for a broader selection.

Erickson *et al.* [9] demonstrated optofluidic tuning of a photonic crystal waveguide structure, see Fig. 1.2. The photonic crystal (triangular lattice, hole radius $r = 140$ nm, period $a = 434$ nm, height $h = 207$ nm) with a line-defect was fabricated on a silicon-on-insulator platform whereas the fluidic network was fabricated in polydimethylsiloxane (PDMS) using multi-layer soft lithography. The fluids chosen for the operation of the device were deionized water (refractive index $n = 1.33$) and 5 mol/L aqueous $CaCl_2$ solution ($n = 1.44$), in order to yield a suitable index contrast and still be compatible with the PDMS material. The transmission spectrum of the waveguide

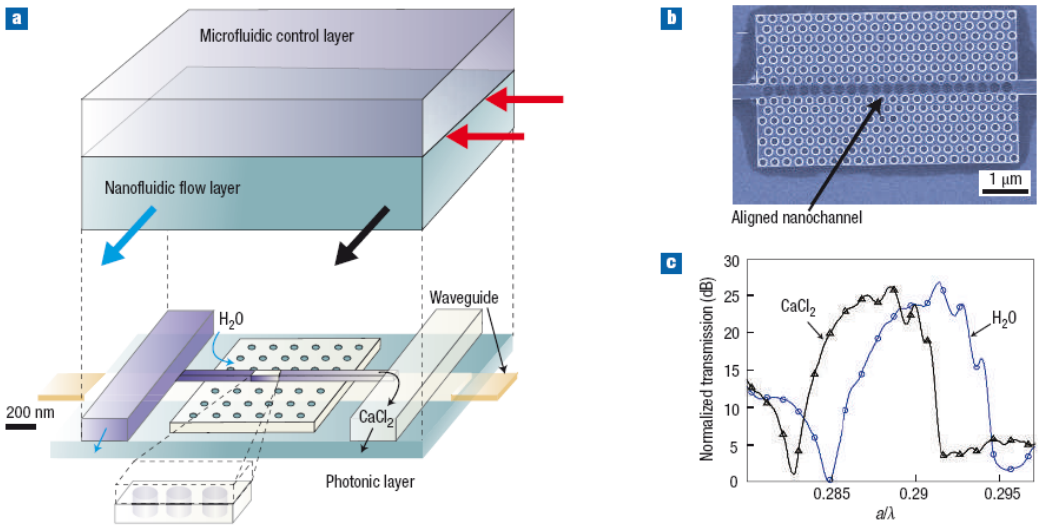

Fig. 1.2: Optofluidic tuning of a photonic crystal waveguide structure [9]. **(a)** Overall schematic of the fluidic network bonded to the photonic crystal chip. **(b)** SEM micrograph of photonic crystal with the central row selectively filled with liquid. **(c)** Transmission of the photonic crystal waveguide with the row of holes filled with water and $CaCl_2$, respectively. From [4].

measured at a wavelength around $\lambda \sim 1.5$ μm shifted approximately 10 nm when exchanging the liquid from water to $CaCl_2$ solution. In this way an optofluidic switch was demonstrated at 1.491 μm by changing the fluid between water and $CaCl_2$ solution with a switching time around 1 minute and an extinction of approximately 19 dB.

Heng *et al.* [10] demonstrated an optofluidic microscope, which may provide a compact alternative to optical microscopy for microfluidic samples, see Fig. 1.3. A 90 nm thick Al film was deposited on a quartz substrate and a row of holes (diamater 600 nm, spacing 5 μm) was defined by electron beam lithography and subsequent reactive ion etch. On top of the holes, a 30 μm wide and 15 μm tall microfluidic channel was fabricated at a small angle relative to the holes by soft lithography in PDMS.

By infusing a fluidic sample through the channel, the sample can be imaged by shining white light from the top, illuminating the sample, and collecting the light through the holes of the array. As the holes are at a small angle to the microfluidic channel, every hole will acquire light from a different part of the sample and as the sample passes the whole array (at constant velocity), and the sample will be completely imaged. The detection of the light was not performed directly on the chip in this demonstration, as a

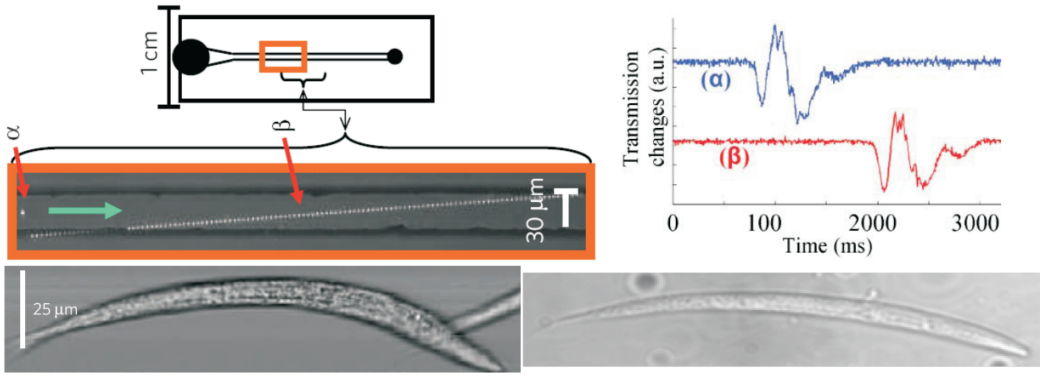

Fig. 1.3: Optofluidic microscope [10]. **Upper panel**: Sketch of device and sample measurement signals from holes marked α and β, respectively. **Lower panel**: Optofluidic (left) and conventional microscope (right) images of *C. elegans* worms. From [3].

standard optical microscope was used as relay for detection. The system has a resolution limit of approximately 500 nm and worms of the simple species *C. elegans* of approximate length 225 µm were imaged with a throughput of approximately 40 worms/min. In future applications, the chip may be integrated with a linear CCD array to yield a compact system, however, the viscous nature and boundary conditions of laminar flow in micro and nanofluidic channels complicate the application of the device when aiming for imaging at the nanometer-scale, since the device relies on constant flow velocity throughout the device.

Domachuk *et al.* [11] demonstrated all-optical beam manipulation in optofluidics, see Fig. 1.4. By optically trapping a 13 µm silica microsphere in a microfluidic channel between two single mode optical fibres, they achieved tunable attenuation of the transmission between the two fibers up to approximately 10 dB at $\lambda = 1.5$ µm. The microsphere functioned as a spherical lens for the light traversing the microchannel. The channel was defined by cutting a single mode fiber which was buried in a layer of cured photo-polymer on a glass substrate using a dicing saw. The channel was between 60-100 µm wide and approximately 500 µm deep. In this way, the two parts of the single mode fiber remain aligned, however, the method is only suitable for the fabrication of straight, deep, and cm-long channels. For the optical trapping, an 1.064 µm laser of average power 800 mW was focused on the sample in an optical tweezers-like setup. Although all-optical beam control has promising applications in all-optical networks, manipulation through optical tweezers remains a serial process and limits the scalability of such systems.

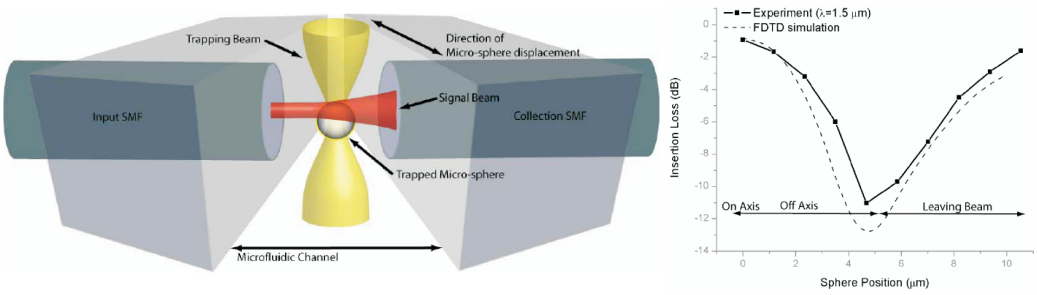

Fig. 1.4: All-optical beam manipulation in optofluidics. By steering an optically trapped beam in a microfluidic channel, the attenuation of light across the channel between two single mode fibres is controlled (maximum attenuation ~ 10 dB). From [11].

The most common and commercialized application involving optofluidics today is the liquid crystal display (LCD). In a LCD pixel, liquid crystal molecules are attached to two transparent electrodes, between two perpendicular linear polarizers. When unpolarized white light is transmitted through the LCD pixel, the light is linearly polarized by the first polarizer. Depending on the voltage applied to the electrodes, the birefringent liquid crystals rotate the polarization of the light, such that it is either transmitted (on-state) or reflected/absorbed (off-state). Depending on the initial configuration of the liquid crystals, the pixel can be transmissive in its on-state or off-state. See Schadt [12] for a review of liquid crystal materials and displays.

1.3 Applications of optofluidic dye lasers

Optical techniques have proven powerful in chemical and biochemical analysis. This has stimulated a large effort in development of light sources which can be integrated on a chip for sensing applications [13].

For these applications, dye lasers are of particular interest due to their flexibility of tuning the lasing wavelength in the visible region. Several commercial laser dyes are available, with emission wavelengths in the interval 400 nm – 900 nm, capable of lasing by means of flashlamp excitation. The typical spectral width of the gain region for each dye is around $50 - 100$ nm, enabling tuning of the lasing wavelength within this region. These advantages have stimulated the development of miniaturized fluidic dye lasers, also referred to as optofluidic dye lasers, in which a liquid laser dye solution is pumped through a microfluidic channel with an embedded optical resonator.

Integrated optofluidic dye lasers are easy to operate since there are no

parts to manually align and they are optically pumped by exciting the dye molecules in the on-chip laser cavity using an external, potentially cheap, light source. By integrating the laser during chip fabrication, no costly or time-consuming alignment of external optical fibres or hybridization steps are necessary. As optofluidic dye lasers are typically fabricated in polymer materials, the cost of materials is low compared to semiconductor diode lasers.

Few optofluidic sensor systems with integrated light sources have been demonstrated. Balslev *et al.* [14] integrated an optofluidic dye laser ($\lambda = 576$ nm) with waveguides, fluidic channels, passive diffusion mixers which were all defined in one layer of SU-8 polymer and photodiodes embedded in the silicon substrate. The device demonstrated on-chip absorption measurements with electrical read-out using two xylenol orange dye solutions with different concentrations.

Other demonstrations of integrated systems capable of performing absorption measurements, although not with as high a level of integration, are Bilenberg *et al.* [15] and Galas *et al.* [16]. Bilenberg *et al.* [15] used thermal nanoimprint lithography (NIL) to fabricate devices integrating an optofluidic dye laser with waveguides, diffusion mixer, and an absorbance cell in a cyclic olefin copolymer (COC) by a parallel fabrication technique. Galas *et al.* [16] performed absorption measurements using methylene blue dye in a system consisting of microfluidic channels in PDMS and a dye-based light source (spectral width ~ 6 nm) composed of two optical fibres with metallized end facets.

Apart from absorption measurements, other sensor concepts have been proposed using integrated devices, e.g. evanescent field sensing, intra-cavity sensing, and interference-based sensing such as differential light beating [17]. The technological success of a sensor device is determined by its sensitivity and specificity, two challenging issues which have not yet in been investigated in detail for the demonstrated devices. For a recent review on optical sensing systems for microfluidics, see Kuswandi *et al.* [18], for a recent review on nanobiosensors, see Erickson *et al.* [19].

1.4 Optofluidic dye lasers

This section briefly reviews the development towards optofluidic dye lasers suitable for lab-on-a-chip systems. The starting point of this review is the invention of the laser in 1960, followed by the first distributed feedback (DFB) lasers, and quickly arriving at optofluidic dye lasers and focusing on optofluidic DFB dye lasers. Recently, Li and Psaltis have reviewed pre-microfluidics era dye lasers and optofluidic dye lasers [20].

The first lasers

In 1960 Maiman published the first experimental demonstration of a laser [21], presenting stimulated emission in ruby at $\lambda = 694$ nm by flashlamp excitation of a ruby rod in a Fabry–Perot cavity. The discovery opened up a whole new field of research which has grown immensely during the following decades. Applications of the laser have spread to virtually every corner in society and industry, spanning from personal items such as laser pointers and DVD players to one of the key elements in telecommunication and industrial applications such as laser welding.

The first report of a dye laser using an organic dye as active medium was that of Sorokin and Lankard in 1966 [22]. They used an ethanolic solution of chloro-aluminum phthalocyanine placed in a glass cell in a macroscopic optical cavity and a giant-pulse ruby laser as pump source. Dye lasers were also demonstrated independently by other groups in 1966 and 1967, see [23, 24] for references. In 1967, Sorokin and Lankard reported the first flashlamp-pumped dye laser [25]. This is an important achievement in an optofluidic context, since it enables the optical pumping of optofluidic dye lasers by means of flashlamps in contrast to larger (and more expensive) pump laser systems.

The first DFB lasers

The first DFB laser was demonstrated in 1971 by Kogelnik and Shank [26]. In a DFB laser, the active material is distributed in the structure providing feedback in the laser resonator, corresponding to the mirrors in a Fabry–Perot cavity. By creating a spatial modulation of the refractive index or gain of the laser structure, light is coupled between backward and forward propagating waves by Bragg scattering. DFB lasers are compact devices as no external optical cavity is needed. The wavelength selectivity of the DFB structure yields narrow linewidth emission and high wavelength stability.

The DFB laser consisted of a gelatin film, which was doped with the organic dye rhodamine 6G (R6G). A periodic modulation of the refractive index of gelatin was achieved by holographic lithography using the interference pattern of two coherent UV laser beams from a He-Cd laser, resulting in a fringe spacing of approximately 300 nm. Subsequently, the gelatin structure was dyed with R6G by soaking the structure in R6G solution to allow the dye molecules to penetrate into the porous gelatin structure. The DFB laser device was pumped by a N_2 UV laser and lasing was achieved around 630 nm.

Later in 1971, Shank *et al.* demonstrated the first tunable DFB laser

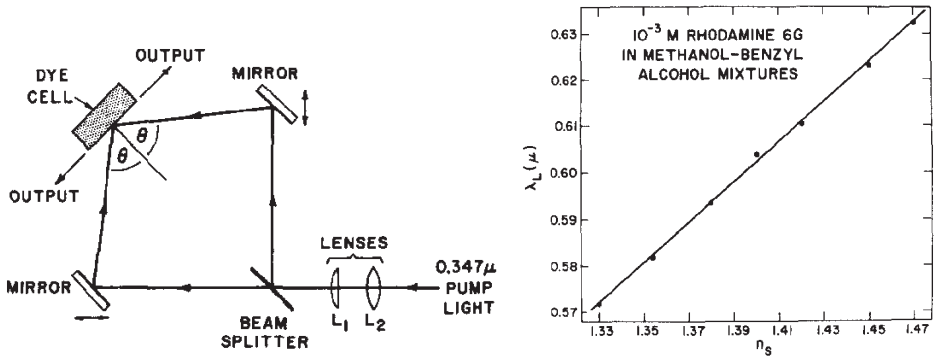

Fig. 1.5: First tunable DFB and first fluidic DFB laser by Shank *et al.* **Left**: Sketch of dye laser. A dye cell was pumped by two coherent beams at incidence angle θ, forming the interference fringes of the DFB laser. **Right**: Tuning results for different solvent refractive indices n_s using different mixtures of methanol and benzyl alcohol ($\theta = 53.8°$). From [27].

which was also the first fluidic DFB laser [27], see Fig. 1.5. The active medium was R6G dissolved in a solvent contained in a glass cell. Feedback was obtained by the fringes formed by the interference of two coherent beams from a frequency doubled ruby laser at $\lambda_p = 347$ nm in a pumped region of approximate dimensions 1.6 cm $\times$ 300 μm. The output dye laser wavelength λ was dependent on the angle of incidence θ of the two incoming pump beams and the refractive index of the solvent n_s through the relation

$$\lambda = \frac{n_s \lambda_p}{\sin\theta} \tag{1.1}$$

A wavelength tunability of 64 nm was demonstrated by variation of n_s and θ. n_s was varied from 1.33 to 1.55 by using different mixtures of methanol and benzyl alcohol as dye solvents. Single mode operation was obtained with a narrow linewidth (< 1 pm) at low pumping intensities. At high pumping intensities, multiple closely-spaced modes appeared, sensitive to the pumping intensity.

A periodic modulation of the *refractive index* throughout the structure with no central phase shift results in two resonances symmetrically spaced (in frequency) around the Bragg frequency. In the case of a *gain* modulated DFB laser, a single resonance is present at the Bragg frequency. The necessity of using a central phase shift when using index gratings as opposed to gain gratings in order to obtain a single resonance at the Bragg frequency was explained in 1972 by Kogelnik and Shank [28] using coupled wave theory. In Chapter 2.3, the role of the phase shift for refractive index modulated DFB

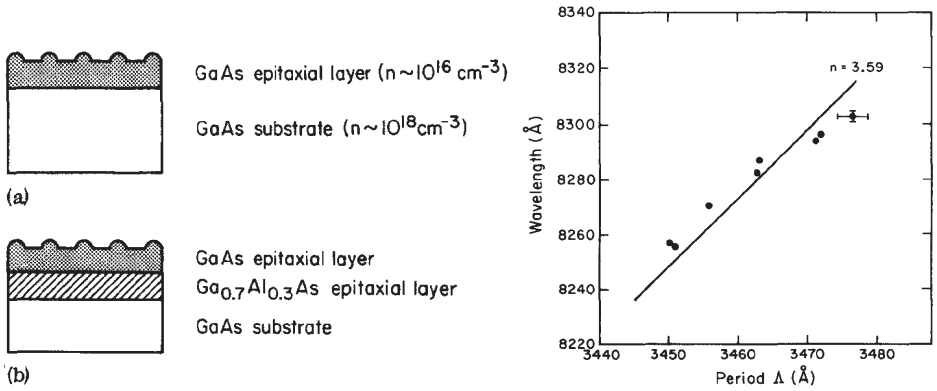

Fig. 1.6: Semiconductor waveguide lasers in GaAs with corrugation feedback by Nakamura *et al.* **Left**: Sketch of devices. **Right**: Demonstration of tuning of the laser wavelength $\sim$ 4.5 nm by changing the corrugation period. From [30].

lasers is discussed.

In 1973, Nakamura *et al.* demonstrated the first semiconductor DFB laser [29], see Fig. 1.6, using corrugation feedback through a periodic modulation of the device surface and thus the refractive index throughout the structure. The corrugations were fabricated by holographic lithography and subsequent ion beam milling on a GaAs substrate. The Bragg condition for feedback is

$$m\lambda = 2\tilde{n}\Lambda, \qquad m = 1, 2, \ldots \qquad \text{(Bragg condition)} \tag{1.2}$$

where m is the reflection order, $\tilde{n}$ is the refractive index of the guided mode, and Λ is the period of the corrugation. Nakamura *et al.* used the third Bragg reflection order ($m = 3$) with a period of $\Lambda \sim 350$ nm without a central phase shift to generate feedback. The use of the first Bragg reflection order ($m = 1$) would have required a grating period of $\Lambda \sim 120$ nm which is experimentally challenging. Using a higher order grating introduces losses in the structure due lower order modes that couple to substrate radiation modes. The sample was cooled to 77 K during characterization and laser light emitted at 832 nm was observed using a pulsed ruby laser as optical pump source.

Later that year, Nakamura *et al.* demonstrated tuning of GaAs waveguide lasers with corrugation feedback by changing the grating period [30], see Fig. 1.6. The laser devices were fabricated by the same fabrication method and pumped by a pulsed dye laser. A tuning range of $\sim$ 4.5 nm of the emitted laser wavelength was demonstrated by changing the grating period.

Since the 1970's, immense research has taken place in the field of fluidic dye lasers and today they are widely used as tunable laser sources in numerous applications, e.g. for optical pumping, laser cooling, parametric processes, and spectroscopy in the visible range. Although dye lasers are very popular light sources for laboratory use, they have not yet penetrated the consumer or health-care markets. Perhaps the development of optofluidic dye lasers can advance optical sensing and provide novel sensor concepts, enabling the breakthrough for dye lasers in everyday-life products.

Optofluidic dye lasers

In 2003, Helbo *et al.* demonstrated the first optofluidic dye laser [31]. The microfabricated device realized a miniaturized Fabry–Perot resonator by evaporating two gold mirrors on the top and bottom of a microfluidic channel. The active medium was R6G dissolved in ethanol, the laser was pumped at 532 nm by a frequency doubled Nd:YAG laser and emitted laser light around 570 nm. The light was emitted vertically up, perpendicular to the chip plane with a broad linewidth of 5.7 nm. The device was further investigated in [32] where a wavelength tunability of 28 nm by variation of the dye concentration was demonstrated.

For lab-on-a-chip systems, a laser resonator with lateral emission in the chip plane is preferred since such a laser is easy to integrate with other components. Of different laterally emitting device layouts, DFB laser resonators have proven particularly suitable for obtaining single mode and low threshold lasing.

The first optofluidic DFB dye laser was demonstrated by Balslev and Kristensen in 2005 [33], see Fig. 1.7. The device was also the first optofluidic dye laser to emit light laterally in the chip plane and in a single mode. The laser cavity was defined by UV lithography as a high order Bragg grating ($m \sim 130$) with a central $\pi/2$ phase shift by alternating SU-8 polymer bars and microfluidic channels. R6G dissolved in ethanol was infused as the active medium through the resonator. Single mode lasing $\lambda = 577$ nm (spectrometer resolution 0.15 nm) with a threshold fluence of approximately 20 $\mu J/mm^2$ was obtained due to transverse-mode selective losses in a multimode waveguide structure where light was not guided in the microfluidic channels.

The laser was integrated with SU-8 output waveguides [33], following the simple idea of Mogensen *et al.* [34], and the integration of the laser with waveguides, fluidic channels, diffusion mixers, and photodiodes into a lab-on-a-chip system was demonstrated [14]. Further, the laser design has been realized in COC by NIL [35] and integrated with imprinted waveguides and fluidics for absorption measurements [15].

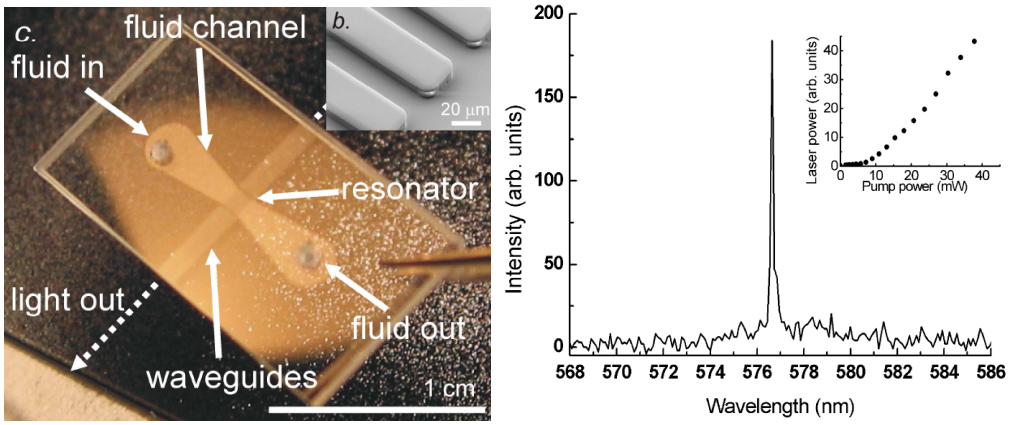

Fig. 1.7: First optofluidic DFB dye laser by Balslev and Kristensen. **Left**: Overview of the dye laser chip. Insert shows SEM micrograph of the ~ 130'th order Bragg grating resonator. **Right**: Single mode emission at $\lambda = 577$ nm and laser threshold fluence of ~ 20 μJ/mm^2. From [33].

Vezenov *et al.* [36] demonstrated the first optofluidic laser employing a liquid-core/liquid-cladding waveguide, using a high refractive index dye-dissolved liquid as waveguide core and a low refractive index liquid as cladding in a PDMS-based device. By covering the end facets of a 1 cm long channel with 100 nm Au, light was emitted around $\lambda \sim 625$ nm with a spectral width of approximately 4 nm.

Taking advantage of the liquid waveguide concept, Li *et al.* demonstrated the first optofluidic liquid-core DFB dye laser [37], see Fig. 1.8. By exploiting the low refractive index of PDMS and a high refractive index dye-dissolved liquid, light was guided in the liquid. A 15'th order Bragg grating with a central $\pi/2$ phase shift was fabricated by soft lithography in a single mode waveguide structure and single mode lasing was emitted at $\lambda = 567.3$ nm with a threshold fluence of approximately 8 μJ/mm^2. An array of five lasers with different grating periods emitting at corresponding wavelengths was also demonstrated [38].

Using the same device, continuous wavelength tuning was achieved demonstrating a novel tuning concept by altering the physical path of the light by changing the length of the grating period through mechanical deformation of the elastic PDMS material [38], see Fig. 1.8. A tuning range of 29 nm was achieved using a single laser dye (R6G), and a total tuning range of 55 nm between 565 and 638 nm was demonstrated by employing two different laser dyes (R6G and rhodamine 101). The laser oscillated at the wavelength of the Bragg order $m = 15$ when using R6G and at the wavelength of the

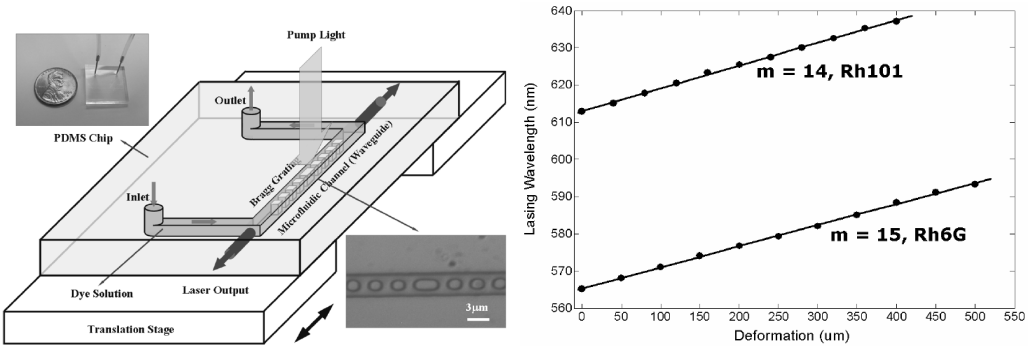

Fig. 1.8: First optofluidic liquid-core DFB dye laser. **Left**: Overview of device and setup for mechanical tuning. **Right**: Mechanical tuning using two different rhodamine dyes and the $m = 14$ and $m = 15$ Bragg reflection orders. Threshold ~ 8 μJ/mm^2. From [38].

Bragg order $m = 14$ when using rhodamine 101.

The distance to the neighboring reflection order is given by the free spectral range (FSR), see Chapter 2.2, which for the $m = 15$ Bragg reflection order is $FSR \sim 40$ nm. Lasing occurs in the mode spectrally closest to the dye gain maximum. As lasing with neither of the two dyes was not reported in a 19 nm gap from 594 nm to 613 nm, one may suspect mode-hopping to take place in this region, as a neighboring mode could be closer to the gain maximum of the dye when the device is stretched or compressed above a certain limit.

Higher order Bragg gratings, such as the ones employed in the two optofluidic DFB lasers reviewed above [33, 37, 38], exhibit losses due to scattering of lower order reflection modes out of the chip plane. These losses can be reduced, enabling a lower threshold for lasing, by employing a lower order Bragg grating, see Chapter 2.2. The requirement for liquid-core waveguiding of a high refractive index liquid and low refractive index polymer [36–38] may be relaxed by reducing the dimensions of the resonator segments by entering the sub-wavelength regime [39].

Table 1.1 summarizes the key features of the reviewed optofluidic dye lasers. Ideally, a first order Bragg grating combined with (liquid-core) waveguiding in the polymer film could be used in order to achieve narrow linewidth, low threshold, and tunable lasing.

Other laser cavity geometries than the ones described above have been demonstrated. Cheng *et al.* [40] demonstrated an optofluidic dye laser (spectral width ~ 10 nm fabricated by femtosecond laser processing in glass, relying on total internal reflection. Gersborg-Hansen *et al.* [41] demonstrated

First author	Resonator type	Linewidth	Q_{th} $[\frac{\mu J}{mm^2}]$	Tuning
Helbo [31,32]	Fabry–Perot	5.7 nm	~ 34	28 nm
Balslev [33]	DFB, $m \sim 130$	< 0.15 nm	~ 20	n/a
Vezenov [36]	Fabry–Perot†	~ 4 nm	~ 11	17 nm
Li [37,38]	DFB†, $m = 14, 15$	< 0.21 nm	~ 8	29/25 nm

Tab. 1.1: Summary of key features of the reviewed optofluidic dye lasers (chronologically listed). Q_{th} is the threshold fluence for lasing and the 'Tuning' column states the reported wavelength tunability. Low order DFB lasers are promising candidates for obtaining narrow linewidth, low threshold, and tunable lasing. († liquid-core waveguiding)

an optofluidic dye ring laser which exhibited multi-mode lasing and was tunable by means of changing the dye solvent and concentration. The cavity design of [41] was integrated with a microfluidic mixer by Galas *et al.* [42] who demonstrated a tunability of 8 nm by changing the R6G concentration. Bilenberg *et al.* [6] integrated an optofluidic light source with a microfluidic diffusion mixer and achieved real-time continuous wavelength tuning range of 10 nm by means of concentration tuning using R6G in ethanol. Kou *et al.* [43] demonstrated multi longitudinal-mode dual-color lasing, each with an overall spectral width of ~ 4 nm by infusing an ethanolic dye solution containing two different dyes in an optofluidic Fabry–Perot cavity composed of two metallized fibre ends with a 140 µm wide microfluidic channel in-between. Peroz *et al.* [44] realized a multi-mode optofluidic 4'th order distributed Bragg reflector laser, fabricated using an UV nanoimprint lithography-based technique. Vasdekis *et al.* [45] presented multi-mode narrow linewidth lasing from pieces of optical fibre which were filled with a dye solution through capillary action. Shopova *et al.* [46] demonstrated whispering gallery mode lasing from dye-filled thin-walled capillary tubes which were coupled to a tapered optical fiber.

Overview

The reported optofluidic dye lasers miniaturize some of the attractive features of macroscopic dye lasers. Using relatively cheap polymer materials, tunable, narrow linewidth, and low threshold lasing in the visible wavelength region has been obtained. The key features of the reviewed optofluidic dye lasers are summarized in Tab. 1.1. Device designs employing planar DFB laser resonators have proven particularly efficient with respect to these parameters and are suitable for integration onto compact lab-on-a-chip systems.

The efficient wavelength selection of the DFB laser resonators results in

narrow linewidth, possibly single mode, emission. By reducing the grating order and increasing the confinement of light to the waveguide core region, the scattering and propagation losses are reduced, reducing the threshold for lasing. Further, reduction of the grating order yields an increase in FSR, enabling a larger wavelength tunable range.

Two tuning principles have been employed in the demonstrations: Tuning by changing the concentration and solvent of the laser dye, and mechanical deformation of the polymer structure, thereby altering the length of the physical path of the light through the resonator.

The optofluidic dye lasers are all pulsed in order to have a short interaction time between the dye molecules and the pump light, thus suppressing the formation of triplet states unsuitable for lasing. This contrasts macroscopic continuous wave dye lasers where the suppression is mediated by a jet flow of the dye solution with typical velocities of several m/s [24]. Employing a similar strategy at the micrometer-scale remains a challenge due to the large hydrodynamic resistance of laminar flow in microfluidics.

Miniaturization of the optical pump sources used to excite the dye molecules in the devices is necessary for the realization of compact optofluidic dye laser systems. Until now, bulky frequency doubled Q-switched flashlamp-pumped Nd:YAG lasers have been the most popular choice. However, as laser thresholds have decreased, it has become possible to use compact diode-pumped laser systems, e.g. a frequency doubled Q-switched diode-pumped Nd:YVO_4 laser as in [45].

Future development in this direction points towards using compact pulsed high power semiconductor laser diodes. Such a pumping scheme employing a GaN laser diode and a pulsed power supply has recently been demonstrated by Karnutsch *et al.* for pumping solid-state organic semiconductor laser devices [47]. Ultimately, a potentially cheap pulsed white light source which even need not be coherent, such as Xe flashlamps, could be used to excite the dye and produce coherent output from optofluidic dye lasers.

Degradation of dye molecules, called dye bleaching, imposed by the external optical pumping is a major concern for the lifetime of organic dye based light sources. In general, the problem is addressed by employing a continuous convective flow of dye solution which replenishes the dye in the cavity.

The flow is typically generated by means of bulky fluidic handling apparatus external to the laser devices, such as syringe pumps, thereby compromising the cost, portability, and miniaturization of optofluidic dye lasers. Simplification of fluidic handling through development of compact and autonomous dye replenishment concepts is important for the successful commercialization of optofluidic dye lasers.

1.5 This thesis

This thesis explores three themes of optofluidic dye lasers:

(i) Improving the efficiency of the resonators in order to reduce the laser threshold.

(ii) Enhancing the tunability of the narrow linewidth dye laser emission.

(iii) Simplification of the fluidic handling.

The threshold for lasing is a key parameter for the feasibility of optofluidic dye lasers in a future technology. In this thesis, we explore device designs employing low order Bragg grating DFB lasers. By reducing the Bragg reflection order, we obtain low out-of-plane scattering losses and achieve low laser thresholds. Although the fluidic resonator segments of the laser resonators are not waveguiding, the sub-wavelength dimensions of the resonator segments yield low losses which ensure low thresholds for lasing.

The tunability of optofluidic dye lasers is an appealing property from macroscopic dye lasers that can be transferred to miniaturized systems and open up a wide field of applications. To enhance the tunability of optofluidic dye lasers, we explore optofluidic refractive index tuning by flowing dye-dissolved liquids of different refractive indices through the laser cavities, thereby fine-tuning the laser wavelength by means of optofluidic functionality. Tuning is also investigated by changing the period of the Bragg grating resonator (coarse-tuning). Further, by employing a low order Bragg grating in the DFB laser resonators, a large FSR is obtained which yields a large wavelength tunability, limited by the spectral width of the gain of the chosen laser dye.

In order to facilitate compact optofluidic dye laser systems suitable for commercial applications, simplification of fluidic handling is necessary. We demonstrate such simplifications by filling the cavity with dye solution through capillary action. This approach, suitable for single-use devices, completely removes the need for fluidic handling apparatus such as syringe pumps, hoses, fittings, valves, etc. Further, we propose a novel dye replenishment mechanism based on diffusion which potentially allows for the operation of optofluidic dye lasers for days without the need for a convective flow.

Reading guidelines

This thesis is organized as follows:

This Chapter comprises an introduction to lab-on-a-chip systems, optofluidics, and optofluidic dye lasers. The Chapter describes the motivation for the work and reviews the development of optofluidic dye lasers.

Chapter 2 introduces the theory necessary for understanding the design and operation of the optofluidic dye laser devices presented in this thesis. Further, the Chapter describes the numerical models developed during this thesis work. A transmission matrix model suitable for design of optofluidic DFB lasers is presented. Finite element simulations of the cavity modes of an optofluidic dye ring laser, which have been published in [48], are described.

Chapter 3 presents the main materials used in this work: The dye R6G and polymer materials SU-8 and PMMA. For R6G, emphasis is on the lasing scheme, fluorescence quantum yield, and absorption/emission characteristics. For the polymers, the focus is on the optical properties, especially dispersion and waveguide propagation loss.

Chapter 4 presents the nanofabrication methods applied in this thesis work. It is concentrated on electron beam lithography (EBL), combined electron beam and UV lithography (CEUL), and nanoimprint lithography (NIL). CEUL in SU-8 is a newly developed fabrication method suitable for functional polymer devices and pattern transfer applications. The main results on CEUL and NIL have been published in [49].

Chapter 5 presents capillary driven tunable optofluidic DFB dye lasers. The DFB lasers rely on light-confinement in a thin SU-8 polymer film and third order Bragg reflection. The lasers exhibit low thresholds and the emission wavelength is tunable over 45 nm by changing the grating period and through optofluidic tuning by varying the refractive index of the dye solvent. The main results of the Chapter have been published in [50, 51].

Chapter 6 presents a novel dye replenishment mechanism for optofluidic dye lasers, based on diffusion rather than convection. For miniaturized systems, diffusion becomes important and by optically pumping a dye solution through a narrow slit, dye molecules are replenished through diffusion alone, omitting the need for fluidic handling apparatus. Diffusive dye replenishment opens up for compact optofluidic dye laser systems with lifetimes on the time-scale of days. The main results of the Chapter have been published in [52].

Chapter 7 concludes the thesis and provides ideas for improvements and applications.

At the end of the thesis, a list of references, list of publications, and an index are available.

2. THEORY AND MODELING

This Chapter describes the basic theory of planar waveguiding and DFB lasers, and the models applied to study the fabricated optofluidic dye lasers. In the models, only the passive resonator structure is investigated, as a reliable incorporation of the spectrally varying and concentration dependent dye gain remains difficult.

For the DFB laser resonators, grating order, free spectral range, and out-of-plane scattering losses are reviewed. A quasi-one dimensional model is developed as a laser device design tool and the role of the central phase shift is investigated.

For an optofluidic dye ring laser, the cavity modes are studied using the finite element method (FEM) and compared to a ray-tracing model. The results have been published in *Journal of Optics A: Pure and Applied Optics*, volume **8**, pages 17–20 (2006) [48].

2.1 Planar dielectric waveguides

Consider the basic layered structure of a dielectric waveguide shown in Fig. 2.1. The middle core layer has a higher refractive index n_{core} than that of the neighboring top and bottom cladding layers n_{top} and n_{bot}, respectively. In the generic waveguide, the layers extend to infinity in the x and y directions, and in the z direction, the top cladding extends to $+\infty$ and the bottom cladding extends to $-\infty$ to avoid reflections from the external boundaries.

The guiding of light in the structure is governed by Maxwell's wave equa-

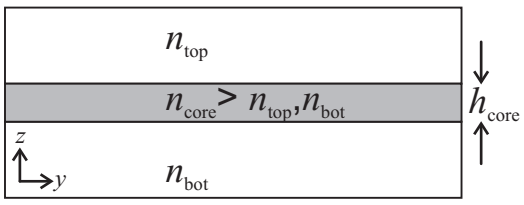

Fig. 2.1: Planar dielectric waveguide.

tion [53]

$$\nabla^2 \mathbf{E}(\mathbf{r},t) = \frac{n^2(\mathbf{r})}{c^2} \frac{\partial^2 \mathbf{E}(\mathbf{r},t)}{\partial t^2} \tag{2.1}$$

For TM-polarized plane waves traveling in the y direction, $H_y = 0$, and the non-zero field components are H_x, E_z, and E_y. From H_x, the remaining two can be determined [53]. H_x has solutions of the form

$$H_x(y,z,t) = \mathcal{H}_x(z) e^{i(\omega t - \beta y)} \tag{2.2}$$

where β is the propagation constant and ω is the frequency of the light. The transverse magnetic component $\mathcal{H}_x$ is given by

$$\mathcal{H}_x(z) = \begin{cases} -C\left[\frac{r}{\bar{q}}\cos(rh_{\text{core}}) + \sin(rh_{\text{core}})\right]\exp\left[p(z+h_{\text{core}})\right]\ ; & -\infty < z \le -h_{\text{core}} \\ C\left[-\frac{r}{\bar{q}}\cos(rz) + \sin(rz)\right]\ ; & -h_{\text{core}} \le z \le 0 \\ -C\frac{r}{\bar{q}}\exp\left[-qz\right]\ ; & 0 \le z < \infty \end{cases} \tag{2.3}$$

where C is a normalization constant and p, $\bar{p}$, q, $\bar{q}$, r, and k are defined by[1]

$$\begin{aligned} q &= \sqrt{\beta^2 - n_{\text{top}}^2 k^2} & \bar{q} &= \tfrac{n_{\text{core}}^2}{n_{\text{top}}^2} q \\ r &= \sqrt{n_{\text{core}}^2 k^2 - \beta^2} & & \\ p &= \sqrt{\beta^2 - n_{\text{bot}}^2 k^2} & \bar{p} &= \tfrac{n_{\text{core}}^2}{n_{\text{top}}^2} p \\ k &= \tfrac{\omega}{c} & & \end{aligned} \tag{2.4}$$

where k is the wave number and c is the speed of light in vacuum.

Employing the boundary conditions of the Maxwell equations, $\mathcal{H}_x$ must be continuous and differentiable at $z = -h_{\text{core}}$, and hence β must fulfill the transcendental equation

$$\tan(rh_{\text{core}}) = \frac{r(\bar{p}+\bar{q})}{r^2 - \bar{p}\bar{q}} \tag{2.5}$$

Only the discrete solutions β_m of Eq. (2.5) correspond to a solution of Eq. (2.1) of the form (2.3) in the waveguide structure and the discrete values β_m correspond to the modes of the waveguide. If only one solution exists, the waveguide is denoted single mode, when multiple modes exist it is denoted multimode. For TE-polarized plane waves, the derivation is parallel, see Ref. [53].

[1] Note the typographical error in Eq. (3.1.5) of [53].

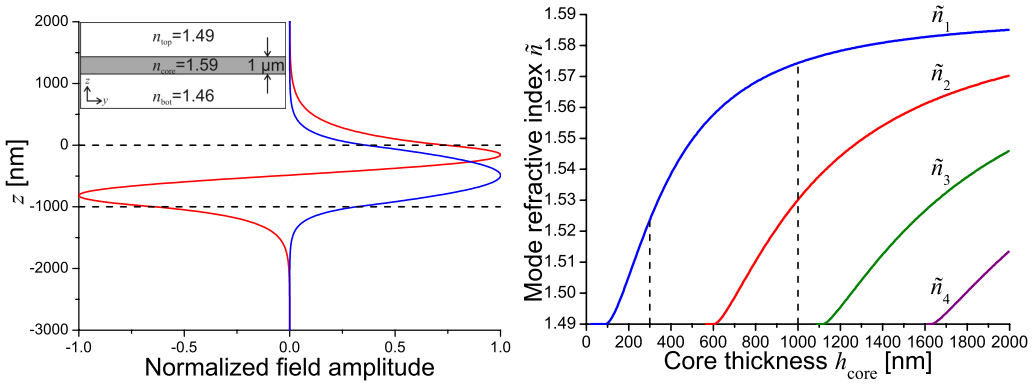

Fig. 2.2: Polymer waveguides. **Left**: Field distributions according to Eq. (2.3) for a waveguide with a 1 µm core. **Right**: Mode refractive indices as a function of core thickness for the different modes of a polymer waveguide.

Equation (2.5) can be solved numerically and from the values of β_m, the mode refractive indices $\tilde{n}_m$ can be determined as

$$\tilde{n}_m = \frac{\beta_m}{k} = \frac{c}{\omega}\beta_m = \frac{\lambda}{2\pi}\beta_m \tag{2.6}$$

where λ is the wavelength of the light. The mode index describes how much of the field is confined to the waveguide core layer, since $\tilde{n} \rightarrow n_{\text{core}}$ for $h_{\text{core}} \rightarrow \infty$.

The left part of Fig. 2.2 shows the field distributions $\mathcal{H}_x(z)$ calculated using Eq. (2.3) for the two modes of a polymer waveguide with $h_{\text{core}} = 1$ µm ($n_{\text{top}} = 1.49$, $n_{\text{core}} = 1.59$, $n_{\text{bot}} = 1.46$). In the core layer, the oscillating field is well-confined and in the cladding regions the field decays exponentially. The confinement renders planar waveguides a key component within integrated optics.

The right part of Fig. 2.2 shows how the mode indices $\tilde{n}_m$ varies with h_{core} for the different modes of the polymer waveguide, according to Eq. (2.6). Higher order modes appear above $h_{\text{core}} \sim 600$ nm. The dashed line at $h_{\text{core}} = 300$ nm in the single mode regime indicates the approximate core thickness used in the fabricated optofluidic dye laser devices.

2.2 Distributed feedback lasers

In DFB lasers, the feedback is generated by interference in the refractive index (or gain) distribution throughout the laser structure. This is attractive for integrated optics compared to a Fabry–Perot cavity, as the fabrication and alignment of mirrors are avoided [53, 54].

The function of a DFB laser resonator is based on Bragg reflection. Bragg reflection occurs when plane waves are reflected in phase from a periodic grating structure of alternating refractive index, see Fig. 2.3(a). In order to achieve constructive interference of plane waves reflected by the dielectric interfaces of neighboring grating periods, the accumulated phase must equal an integer number of wavelengths

$$m\lambda_m = 2\Lambda_{\mathrm{op}}\,, \qquad m = 1, 2, 3, \ldots \qquad \text{(Bragg condition)} \qquad (2.7)$$

where $\Lambda_{\mathrm{op}} = \tilde{n}_1 L_1 + \tilde{n}_2 L_2$ is the optical path length of a grating period, m is the grating order, and λ_m is the corresponding Bragg wavelength. $\tilde{n}_j$, L_j ($j = 1, 2$) are the refractive index and length of layer j, respectively, and $\Lambda = L_1 + L_2$ is the grating period.

In the two-dimensional (2D) laser structure of Fig. 2.3(b), the determination of the refractive indices is more complicated. The core of a polymer waveguide structure ($n_{\mathrm{bot}} = 1.46$, $n_{\mathrm{top}} = 1.49$) is modified with a DFB structure with the refractive index alternating between n_1 and n_2. A simple approach is to approximate the structure with a one-dimensional (1D) structure similar to that of Fig. 2.3(a) and employ the mode refractive indices of the corresponding infinite planar waveguides for the two materials $\tilde{n}_1$, $\tilde{n}_2$, calculated by means of Eqs. (2.1)-(2.6). A transmission matrix model is developed along these lines in Chapter 2.3.

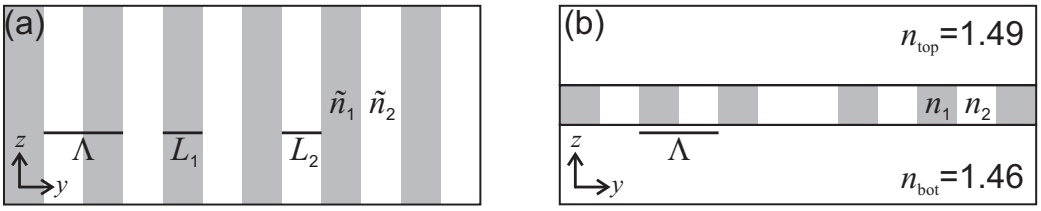

Fig. 2.3: Sketch of DFB lasers. **(a)** 1D Bragg grating. **(b)** 2D DFB laser structure with central phase shift based on a planar waveguide structure (discussed in Chapter 2.3).

Free spectral range

The free spectral range (FSR) of the DFB laser resonator is defined as the distance between two neighboring modes

$$FSR = \lambda_{m-1} - \lambda_m \qquad m = 2, 3, \ldots \tag{2.8}$$

By employing the Bragg condition (2.7), this can be rewritten as

$$FSR = 2\Lambda_{\text{op}} \left(\frac{1}{m-1} - \frac{1}{m} \right) = \frac{2\Lambda_{\text{op}}}{m} \frac{1}{m-1} = \frac{\lambda_m}{m-1} \tag{2.9}$$

Figure 2.4 shows the spectral position of grating resonances for gratings of different grating orders with the m'th resonance situated at $\lambda_m = 580.6$ nm. The resonances are calculated using Eq. (2.7). The FSR is calculated using Eq. (2.9), and the results for the gratings of Fig. 2.4 are listed in Tab. 2.1. As the grating order is decreased, so is Λ_{op}, and the FSR increases dramatically. In each plot of Fig. 2.4, the measured fluorescence spectrum of R6G solution in ethylene glycol with the gain maximum situated at $\lambda \sim 565$ nm is shown.

For a laser with modes of equal loss, the laser will oscillate in the mode with highest gain, i.e. the mode which is spectrally closest to the gain maximum. If multiple modes are situated close to the gain maximum, as for the gratings of order $m = 130, 15$ in Fig. 2.4(a),(b), and the wavelength is tuned so that a neighboring mode is closer to the gain maximum, mode-hopping will occur and the laser will begin to oscillate in the neighboring mode. For a tunable single mode laser, the FSR yields the maximum achievable wavelength tunability without mode-hopping.

For the $m = 130, 15$ order Bragg gratings in Fig. 2.4(a),(b), multiple resonances are located within the gain region, and the tunability is limited by the FSR, see Tab. 2.1. For the $m = 3$ grating, see Fig. 2.4(c), the tunability is no longer limited by the FSR but the width of the gain region of the chosen laser dye.

m	Λ_{op} [μm]	FSR [nm]
130	75.478	4.5
15	8.709	41.5
3	1.742	290.3

Tab. 2.1: Calculated Λ_{op} and FSR for Bragg gratings of different order m using Eqs. (2.7) and (2.9), respectively, with $\lambda_m = 580.6$ nm.

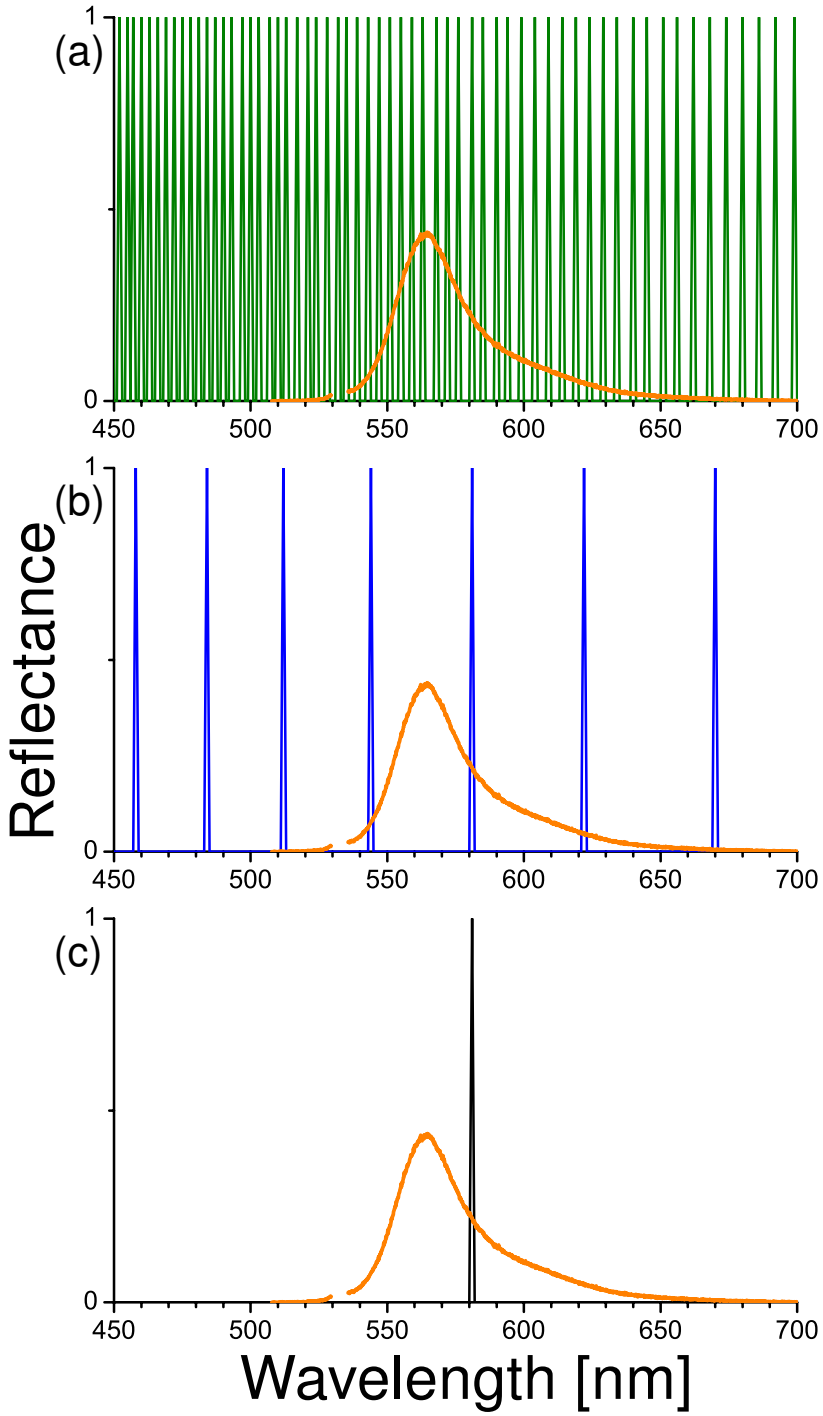

Fig. 2.4: Spectral distribution of resonances for Bragg gratings of different orders m. The orange curve shows a measured fluorescence spectrum of a R6G solution. **(a)** $m = 130$ with $\lambda_{130} = 580.6$ nm. **(b)** $m = 15$ with $\lambda_{15} = 580.6$ nm. **(c)** $m = 3$ with $\lambda_3 = 580.6$ nm.

Out-of-plane scattering

Higher order Bragg gratings are subject to out-of-plane scattering [53]. The corrugated waveguide structure shown in Fig. 2.5 represents such a grating. Consider a waveguide mode of mode refractive index $\tilde{n}$ traveling towards the right in the structure. For waves scattered off successive teeth in the grating to be in phase, their optical path length must be an integer multiple of the wavelength. Defining b as in Fig. 2.5, this yields the phase condition

$$\ell'\lambda = \tilde{n}\,(b + \Lambda) \qquad \ell' = 1, 2, \ldots \tag{2.10}$$

From Fig. 2.5, b can be expressed by the grating period Λ and the angle θ as the side of a right triangle

$$b = \Lambda \sin\theta \tag{2.11}$$

where θ is defined as the angle that the scattered wavefront makes with the plane of the waveguide. Angles in the range $\theta \in [-90°; 90°]$ may be obtained. θ is also the angle between the direction of the scattered rays and the normal to the waveguide plane. Combination of Eqs. (2.10) and (2.11) yields an expression for θ

$$\sin\theta = \frac{\ell'\lambda}{\tilde{n}\Lambda} - 1\,, \qquad \ell' = 0, 1, 2, \ldots, m \tag{2.12}$$

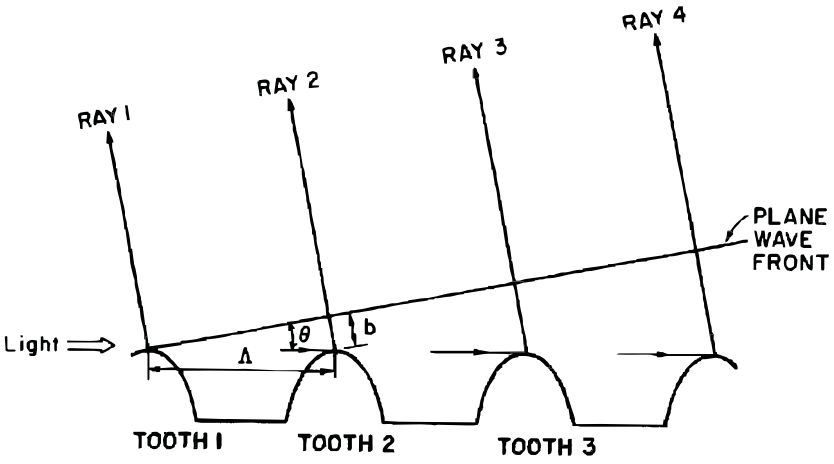

Fig. 2.5: Out-of-plane scattering. A waveguide mode is traveling towards the right and is scattered off the teeth of the high order corrugation grating. Reproduced from [53].

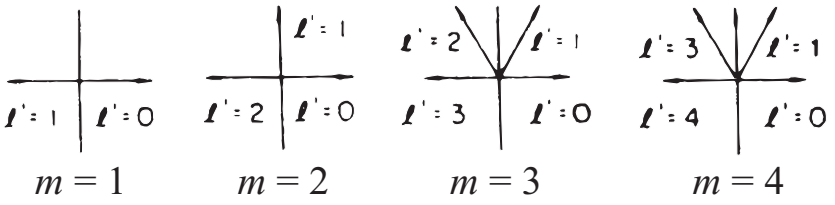

Fig. 2.6: Sketch of directions of out-of-plane scattering for gratings of different order m. Reproduced from [53].

By identifying $\Lambda_{\text{op}} = \tilde{n}\Lambda$ and applying the Bragg condition (2.7), one obtains

$$\sin\theta = \frac{2\ell'}{m} - 1\,, \qquad \ell' = 0, 1, 2, \ldots, m \tag{2.13}$$

which is practical for calculating the out-of-plane scattering angles of gratings of different orders. Table 2.2 and Fig. 2.6 show the different scattering directions for gratings of order $m = 1, 2, 3, 4$.

The strong coupling to out-of-plane scattering for the second order grating is, in general, undesired for DFB lasers designed to emit light in the chip plane. Ideally, a first order grating should be used to achieve the best performance.

However, fabrication tolerances may prevent the use of a first order grating, in which case a third order grating should be used since the coupling to out-of-plane scattering is much weaker than for a second order grating [53]. Based on this analysis, third order DFB lasers was the best choice for the fabricated devices.

m	1	2	3	4
$\ell' = 0$	$-90°$	$-90°$	$-90°$	$-90°$
$\ell' = 1$	$90°$	$0°$	$-19.5°$	$-30°$
$\ell' = 2$		$90°$	$19.5°$	$0°$
$\ell' = 3$			$90°$	$30°$
$\ell' = 4$				$90°$

Tab. 2.2: Directions of out-of-plane scattering for gratings of different order m, calculated using Eq. (2.13). See Fig. 2.5 for a definition of θ.

2.3 Transmission matrix model for design of DFB lasers

For periodic structures such as Bragg gratings, the reflectance and transmittance[2] can be conveniently calculated in the 1D case using transmission matrices. Upon introducing the transmission matrices for two basic optical elements, the basic matrices are combined to represent an entire DFB laser resonator with phase shift in a quasi-1D model.

The advantage of the transmission matrix approach for ray tracing purposes is that when combining several optical elements in a serial chain, the resulting transmission matrix is straightforward to compute. This treatment of transmission matrices is based on Chapter 3 of [54].

Transmission matrices

The transmission matrices are based on normalized field amplitudes and can be converted into scattering matrices. The normalization of the electric field is done such that the power flow of the electric field is the absolute square of the normalized field amplitude A.

To do this, assume that the electric field is a plane monochromatic wave traveling in the y direction which is linearly polarized along the $\mathbf{e}_\mathrm{p}$ vector, that is

$$\mathbf{E}(x,y,z,t) = E_0\,\mathbf{e}_\mathrm{p}\,U(x,z)\,e^{i(\beta y-\omega t)} \tag{2.14}$$

where $U(x,z)$ is the field intensity distribution, normalized by $\iint |U(x,z)|^2\,dxdz = 1$. The power of the electric field is calculated as

$$P = \frac{1}{2}\epsilon_0 nc\,|E_0|^2 \underbrace{\iint |U(x,z)|^2\,dxdz}_{1} = \frac{1}{2}\epsilon_0 nc\,|E_0|^2 \tag{2.15}$$

Let A be defined as

$$A = \sqrt{\frac{1}{2}\epsilon_0 nc}\,E_0\,e^{i\beta y} \tag{2.16}$$

having the same phase as the electric field (2.14). Hence, by this definition $|A|^2$ is equal to the power flow P through Eq. (2.15).

The transmission matrix $\hat{\mathbf{T}}$ relates the forward traveling waves A_j and backward traveling waves B_j $(j = 1, 2)$ of an optical element with two input

[2] Depending on the source, the terms reflectance/transmittance or reflectivity/transmissivity are used for the normalized amount of reflected/transmitted energy of an incoming signal. In this thesis, the terms reflectance and transmittance are used for these quantities, respectively.

Fig. 2.7: Definition of the transmission matrix $\hat{\mathbf{T}}$. The matrix relates the forward (A_j) and backward (B_j) traveling waves.

and output ports, see Fig. 2.7,

$$\begin{bmatrix} A_1 \\ B_1 \end{bmatrix} = \hat{\mathbf{T}} \begin{bmatrix} A_2 \\ B_2 \end{bmatrix} \tag{2.17}$$

A pair of elements with forward and backward traveling waves A_j, B_j and A'_j, B'_j $(j = 1, 2)$, respectively, can be combined so that the output of the first (A_2, B_2) is the input of the second (A'_1, B'_1), i.e. $A_2 = A'_1$, $B_2 = B'_1$. This yields

$$\begin{bmatrix} A_1 \\ B_1 \end{bmatrix} = \hat{\mathbf{T}} \begin{bmatrix} A_2 \\ B_2 \end{bmatrix} = \hat{\mathbf{T}} \begin{bmatrix} A'_1 \\ B'_1 \end{bmatrix} = \hat{\mathbf{T}}\,\hat{\mathbf{T}}' \begin{bmatrix} A'_2 \\ B'_2 \end{bmatrix} \tag{2.18}$$

The resulting transmission matrix for the joined system is the matrix product of the two transmission matrices. This simple relation is the essence of the powerful calculation method of transmission matrices for complicated systems with many elements.

In order to determine the elements of a transmission matrix, the elements are related to the reflection and transmission coefficients of the optical element

$$r_{12} = \left.\frac{B_1}{A_1}\right|_{B_2=0}; \quad t_{12} = \left.\frac{A_2}{A_1}\right|_{B_2=0}; \quad r_{21} = \left.\frac{A_2}{B_2}\right|_{A_1=0}; \quad t_{21} = \left.\frac{B_1}{B_2}\right|_{A_1=0} \tag{2.19}$$

where the subscripts refer to the left (1) and right (2) sides of the optical element, cf. Eq. (2.17), see Fig. 2.7.

The matrix elements can be expressed by the reflection and transmission coefficients by combining Eqs. (2.17) and (2.19) [54]

$$\hat{\mathbf{T}} = \frac{1}{t_{12}} \begin{bmatrix} 1 & -r_{21} \\ r_{12} & t_{12}t_{21} - r_{12}r_{21} \end{bmatrix} \tag{2.20}$$

Vice versa, the reflection and transmission coefficients can be expressed through the elements of the transmission matrix as [54]

$$r_{12} = \frac{T_{21}}{T_{11}}; \quad t_{12} = \frac{1}{T_{11}}; \quad r_{21} = -\frac{T_{12}}{T_{11}}; \quad t_{21} = \frac{\det \hat{\mathbf{T}}}{T_{11}} \tag{2.21}$$

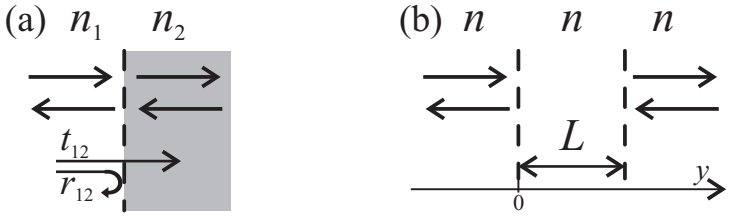

Fig. 2.8: Sketches of the basic optical elements of a Bragg grating. **(a)** Dielectric interface (normal incidence). **(b)** Propagation in a homogeneous medium.

Basic elements

For a dielectric interface, see Fig. 2.8(a), the transmission matrix is derived using the reflection and transmission coefficients from the Fresnel equations at normal incidence

$$r_{12} = \frac{n_1 - n_2}{n_1 + n_2}\,; \qquad t_{12} = \sqrt{1 - r_{12}^2} = \frac{2\sqrt{n_1 n_2}}{n_1 + n_2} \tag{2.22}$$

Also, $r_{21} = -r_{12}$ and $t_{12} = t_{21}$, and Eq. (2.20) yields

$$\hat{\mathbf{T}}_{12} = \frac{1}{t_{12}} \begin{bmatrix} 1 & r_{12} \\ r_{12} & 1 \end{bmatrix} \tag{2.23}$$

For light propagating through a homogeneous medium of length L, see Fig. 2.8(b), there is no coupling between forward and backward traveling waves. There are no reflections, i.e. $r_{12} = r_{21} = 0$, and only the phase of the transmitted signals is changed. Expressed in terms of normalized field amplitudes, the relations are

$$A_2 = A_1\, e^{i\beta L}\,; \qquad B_2 = B_1\, e^{-i\beta L}\,; \qquad \beta = \frac{2\pi}{\lambda} n \tag{2.24}$$

and employing Eqs. (2.19) and (2.20) yields the transmission matrix

$$\hat{\mathbf{T}}_L = \frac{1}{e^{i\beta L}} \begin{bmatrix} 1 & 0 \\ 0 & e^{2i\beta L} \end{bmatrix} = \begin{bmatrix} e^{-i\beta L} & 0 \\ 0 & e^{i\beta L} \end{bmatrix} \tag{2.25}$$

Transmission matrix model of DFB laser cavities

One period of a Bragg grating consists of two segments of length L_j $(j = 1, 2)$ with homogeneous propagation and two segments with dielectric interfaces between media 1 and 2. Hence, by matrix multiplication, the transmission matrix for a grating period $\hat{\mathbf{T}}_\Lambda$ becomes

$$\hat{\mathbf{T}}_\Lambda = \hat{\mathbf{T}}_{L_1} \hat{\mathbf{T}}_{12} \hat{\mathbf{T}}_{L_2} \hat{\mathbf{T}}_{21} \tag{2.26}$$

The resulting transmission matrix for a grating structure with M periods becomes

$$\hat{\mathbf{T}}_M = \left(\hat{\mathbf{T}}_\Lambda\right)^M \tag{2.27}$$

From $\hat{\mathbf{T}}_M$, the energy transmittance T and the phase ϕ_T of the transmitted light of the whole grating structure can be calculated using Eq. (2.21)

$$T = |t_{12}|^2 = \left|\frac{1}{T_{11}}\right|^2 \; ; \qquad \phi_T = \arg\left(t_{12}\right) \tag{2.28}$$

The reflectance can be extracted from the corresponding expression of Eq. (2.21). Alternatively, due to energy conservation, the energy reflectance R can be calculated as $R = 1 - T$ (disregarding losses).

In order to use the model as a design tool for DFB laser cavities such as the one sketched in Fig. 2.3(b), the refractive indices of the different layers are approximated. In the fabricated devices, the materials used for the waveguide core are SU-8 polymer ($n_1 = 1.59$) and dye-dissolved liquids ($n_2 = 1.36 - 1.485$), see Chapter 5. The cladding materials have the refractive indices $n_{\text{top}} = 1.49$ and $n_{\text{bot}} = 1.46$.

In the following examples, a waveguide structure of core height $h_{\text{core}} = 300$ nm is considered. A third order grating ($m = 3$) is designed with a central wavelength of $\lambda = 570$ nm. The SU-8 segments are $L_1 = 280$ nm wide, and the channels are $L_2 = 312$ nm wide, i.e. the grating period is $\Lambda = 592$ nm. These dimensions are similar to the ones for the fabricated optofluidic DFB dye lasers in Chapter 5. In the calculations, $M = 50$ grating periods are used, instead of the $M \sim 845$ periods of the fabricated 500 µm long gratings, in order to limit the computing time.

For the SU-8 segments, the refractive index can be approximated using the mode refractive index of Eq. (2.6) for the corresponding waveguide structure, see Fig. 2.2 (page 21), i.e.

$$\tilde{n}_1 = \frac{\beta_1}{k} = 1.525 \tag{2.29}$$

Due to the low refractive indices of the liquids, $n_2 < n_{\text{top}}$, no confined TE-TM waveguide mode exists and light is not guided in the fluidic resonator segments. However, since the resonator segments are of sub-wavelength dimensions, $L_1, L_2 \lesssim \lambda$, a significant amount of light can still propagate across the channel and enter the adjacent SU-8 waveguide segment. To account for the reduced refractive index in the fluidic resonator segment, $\tilde{n}_2$ is taken as

$$\tilde{n}_2 \sim \frac{\tilde{n}_1}{n_1}\, n_2 \tag{2.30}$$

This is a rough estimate where all coupling losses are disregarded. The coupling loss is estimated using a beam propagation method in Chapter 5.5. For $n_2 = 1.43$ (ethylene glycol solution), Eq. (2.30) yields $\tilde{n}_2 \sim 1.3716$ and the optical path of a grating period becomes $\Lambda_{\text{op}} = 855$ nm. The transmission matrix model in [55] uses a similar approach.

Fig. 2.9 shows the calculated transmittance T for the grating structure described above. The values for T are converted to dB using the relation $T_{\log} = 10 \log_{10} T$, as the input is normalized to unity. Light incident at the Bragg wavelength is reflected, due to constructive interference of the light reflected at the dielectric interfaces of the grating. Correspondingly, light at the Bragg wavelength transmitted through the grating experiences destructive interference, see Fig. 2.9. The interval centered around the Bragg wavelength where almost all light is reflected is referred to as the stop band. The width of the stop band is determined by the index contrast $\tilde{n}_1 - \tilde{n}_2$. As the grating has a finite number of periods, the value for T does not become identically 0 at the Bragg wavelength.

DFB lasers based on a Bragg grating without a central phase shift are known as band edge lasers, as the lasers oscillate at the wavelengths of the edges of the stop band. The group velocity of the light goes to zero at

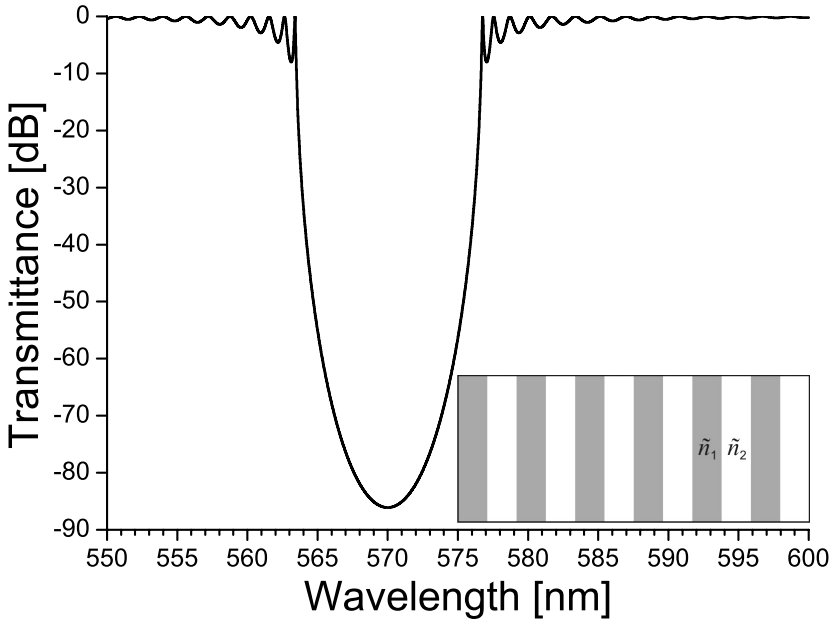

Fig. 2.9: Transmittance of grating structure without phase shift. A clear stop band around the Bragg wavelength is seen.

the band-edges which leads to lasing by means of standing waves in the grating [56].

The role of the central phase shift

In order for a laser to oscillate, the electric field must exactly replicate itself after each round trip. For a Fabry–Perot laser resonator consisting of two flat mirrors of reflection coefficients r_1 and r_2, respectively, positioned a distance L apart, see Fig. 2.10(a), this oscillation condition becomes [54]

$$\mathbf{E} = r_1 e^{i\beta L} r_2 e^{i\beta L} \mathbf{E} \quad \text{i.e.} \tag{2.31}$$

$$1 = r_1 r_2 e^{2i\beta L} \tag{2.32}$$

where $\mathbf{E}$ is the initial electric field of the form (2.14). The term $e^{2i\beta L}$ corresponds to the propagation length $2L$ of a resonator round trip.

The losses of the resonator must be balanced by the gain of the active material to obtain lasing. Gain and loss may be added to the condition as an imaginary part of the propagation constant β. In the fabricated optofluidic DFB lasers, the losses originate mainly from material absorption and light lost to the cladding layers in the fluidic resonator segments, whereas the necessary gain is supplied by the dye molecules. However, practical values for the R6G gain are not available and depend on e.g. dye concentration and optical pumping conditions. Thus, the loss-less passive resonator structure is considered here.

Consider a DFB grating without phase shift with a 50/50 duty cycle, i.e. $L_j = \lambda_m/(4\tilde{n}_j)$ $(j = 1, 2)$, see Fig. 2.10(b). The central grating segment of width L_2 can be treated as a small cavity between two half-gratings, both with a reflection coefficient r_g close to unity near the Bragg wavelength λ_m. Further, the phase of r_g is close to zero near the Bragg wavelength. The oscillation condition for light near the Bragg wavelength to oscillate in the

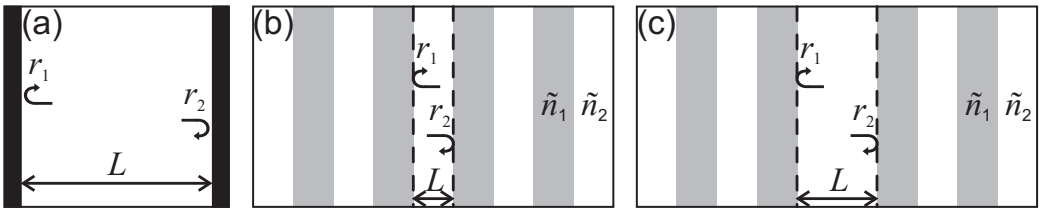

Fig. 2.10: Different laser resonator structures. **(a)** Fabry–Perot resonator. **(b)** DFB resonator without phase shift. **(c)** DFB resonator with central $\pi/2$ phase shift.

resonator between the two grating mirrors is given by (2.32)

$$r_g(\lambda_m)r_g(\lambda_m)e^{2i\beta_m L_2} = e^{i\pi} = -1 \qquad \text{(no phase shift)} \tag{2.33}$$

This oscillation condition has no solution at the Bragg wavelength which agrees well with the fact that all light is reflected by the grating and light cannot propagate through. The transmittance for such a grating structure is shown in Fig. 2.9.

If instead the small cavity has the length $2L_2$, see Fig. 2.10(c), i.e. an extra length L_2 is added corresponding to a phase rotation of $\pi/2$, the oscillation condition (2.32) becomes

$$r_g(\lambda_m)r_g(\lambda_m)e^{4i\beta_m L_2} = e^{i2\pi} = 1 \qquad \text{(with phase shift)} \tag{2.34}$$

which has a solution at the Bragg wavelength. To calculate the transmission matrix for this structure, the transmission matrix of the added phase shift is simply added in the matrix multiplication as

$$\hat{\mathbf{T}}_M = \left(\hat{\mathbf{T}}_\Lambda\right)^{M/2} \hat{\mathbf{T}}_{L_2} \left(\hat{\mathbf{T}}_\Lambda\right)^{M/2} \tag{2.35}$$

Fig. 2.11 shows the transmittance for a grating similar to that of Fig. 2.9 but including a central phase shift, cf. Fig. 2.10(c). In the center of the grating, an extra channel width is added which introduces a phase lag of $\pi/2$ and a single resonance at the Bragg wavelength is obtained. The spectral position of the resonance in the stop band depends e.g. on the width of the phase shift.

Optofluidic refractive index tuning

Although the quasi-1D model is based on the approximation that the refractive index $\tilde{n}_1$ can be calculated from a corresponding infinite planar waveguide structure, Eq. (2.6), and the refractive index $\tilde{n}_2$ in the fluidic resonator segments is basically 'guessed', the model can be used to roughly estimate the laser wavelength and the optofluidic tunability of the fabricated lasers. In this way, the model functions well as a design tool for optofluidic DFB dye lasers.

The optofluidic refractive index tuning range for a fixed resonator geometry with a central $\pi/2$ phase shift can be calculated from the Bragg condition (2.7) as

$$\Delta\lambda_m = \frac{2L_2}{m}\Delta\tilde{n}_2 \sim \frac{2\tilde{n}_1 L_2}{n_1 m}\Delta n_2 \tag{2.36}$$

where Δn_2 is the change in fluid refractive index.

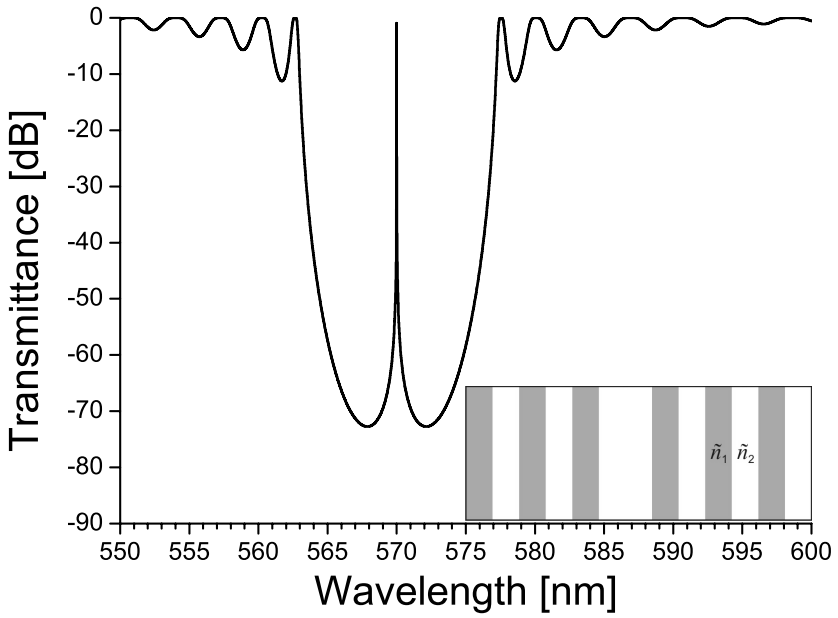

Fig. 2.11: Transmittance of grating structure with central $\pi/2$ phase shift. A single resonance is situated in the middle of the stop band at the Bragg wavelength.

Using the laser geometry of Fig. 2.11 and changing fluid refractive index n_2 from 1.43 to 1.485, i.e. $\Delta n_2 = 0.055$, yields $\Delta\lambda = 11.0$ nm. In the experiments described in Chapter 5 with grating period $\Lambda = 599$ nm, results using this value of Δn_2 are shown, yielding $\Delta\lambda = 7.69$ nm, see Tab. 5.3 (page 82). This is within 30 % of the calculated value.

2.4 Finite element simulation of the cavity modes of an optofluidic dye ring laser

This section presents the efficient use of FEM to simulate the cavity modes of an optofluidic dye ring laser. I have carried out the simulations using the commercial software Comsol FEMLAB 3.1 [57] and explained the function of the optofluidic dye ring laser by finding the optical modes of the passive cavity.

For a recently reported microfluidic dye ring laser [41], the full wave nature of TE modes in the cavity is studied by means of finite element simulations. The resonance wave-patterns of the cavity modes support a ray-tracing view and the the spectrum is explained in terms of standing waves with a

mode spacing $\delta k = 2\pi/L_{\text{eff}}$ where L_{eff} is the effective optical path length in the cavity.

Typically, cavity designs of optofluidic dye lasers rely on classical ray-tracing arguments rather than full wave simulations. In this section, a geometry resembling that of Refs. [40–42] is considered, and a full wave study of the TE modes in the cavity is offered. The resonance wave-patterns of the cavity modes support the ray-tracing view and the mode spacing of the spectrum is explained in terms of standing waves.

Geometry

Consider the 2D laser resonator illustrated in Fig. 2.12 which corresponds to the planar cavities studied experimentally in Refs. [40–42]. The cavity resembles a classical Fabry–Perot resonator and consists of two dielectric isosceles triangles with baseline ℓ_{pol} and refractive index n_{pol} separated by a microfluidic channel of width ℓ_{ch} containing a fluid with refractive index n_{ch}. Light is confined to the cavity by total-internal reflections at the polymer-air interfaces at an angle of incidence of $\pi/4$. Out coupling of power occurs through an evanescent-field coupling to an adjacent polymer region.

In the experiments in Refs. [41, 42] the microfluidic channel is filled by

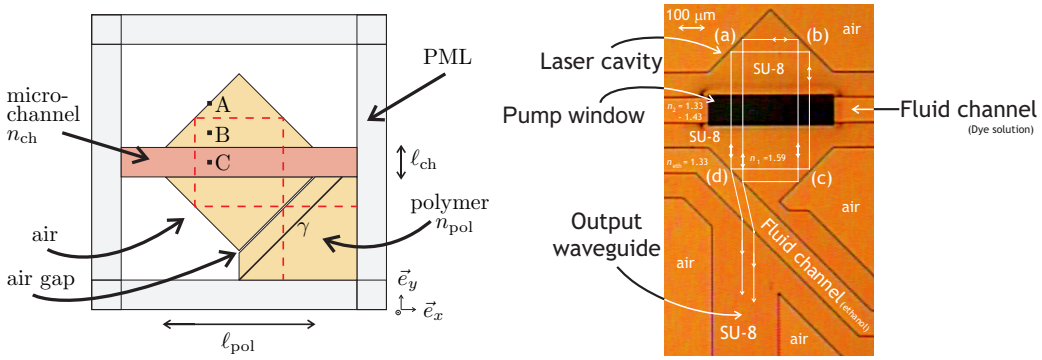

Fig. 2.12: Geometry consisting of a polymer-defined micro-cavity with an embedded microfluidic channel containing a dissolved laser dye. **Left**: Geometry for the FEM simulations. Out coupling of power from the cavity occurs through an evanescent-field coupling through an air gap to an adjacent polymer region where the output power is evaluated by an integral along the solid line γ. The dashed line indicates a typical optical path in the cavity. Simulations are carried out for a point-source excitation at positions A, B, and C, respectively. **Right**: Microscope image of the fabricated device [41].

a dye doped liquid acting as gain medium. In Ref. [41] $\ell_{\mathrm{pol}} \sim 700\,\mu\mathrm{m}$, the cavity is pumped at the wavelength $\lambda = 532\,\mathrm{nm}$ by a pulsed frequency doubled Nd:YAG laser, and lasing occurs in the visible around $\lambda \sim 570\,\mathrm{nm}$. See Ref. [41] for details on the pump power and lasing threshold.

Throughout the rest of this section, a typical structure with $\ell_{\mathrm{ch}}/\ell_{\mathrm{pol}} = 0.2$ is considered, and for the evanescent-field coupling $w/\ell_{\mathrm{pol}} \simeq 0.028$ is chosen for the width w of the air gap. For the refractive indices, $n_{\mathrm{pol}} = 1.6$ and $n_{\mathrm{ch}} = 1.43$ are used. These numbers give an index step which is typical for a liquid and a polymer. Note, however, that the particular choice of numbers does not affect the overall findings and conclusions.

Quasi one-dimensional approach to mode spacing

First, the mode spacing is estimated by considering a plane wave traveling around in the cavity, see Fig. 2.12. In this ray-tracing like approach, reflections at the polymer-fluid interfaces are neglected. This is justified by the very small Fresnel reflectance

$$R = \left(\frac{n_{\mathrm{pol}} - n_{\mathrm{ch}}}{n_{\mathrm{pol}} + n_{\mathrm{ch}}}\right)^2 \simeq 0.31\,\% \tag{2.37}$$

The modes are imagined to be somewhat similar to whispering-gallery modes (WGMs) in resonators of circular shape. However, in this case the modes are subject to four total-internal reflections at an incidence angle of $\pi/4$ irrespectively of the mode index and all modes have the same effective optical path length. Thus, contrary to WGMs these modes have no cut-off for decreasing mode index caused by decreasing incidence angle. The accumulated phase during one round-trip of a plane-wave in the ring cavity is

$$\delta\phi = kL_{\mathrm{eff}} + \varphi \tag{2.38}$$

where $k = 2\pi/\lambda = \omega/c$ is the free-space wave number,

$$L_{\mathrm{eff}} = 2n_{\mathrm{pol}}\ell_{\mathrm{pol}} + 2n_{\mathrm{ch}}\ell_{\mathrm{ch}} \tag{2.39}$$

is the effective optical path length in the cavity, and

$$\varphi = 4 \times \arg\left(\frac{\cos(\frac{\pi}{4}) - \sqrt{n_{\mathrm{pol}}^{-2} - \sin^2(\frac{\pi}{4})}}{\cos(\frac{\pi}{4}) + \sqrt{n_{\mathrm{pol}}^{-2} - \sin^2(\frac{\pi}{4})}}\right) \tag{2.40}$$

is the phase picked up during the four total-internal reflections at the polymer-air interfaces at incidence angle of $\pi/4$. The resonance condition is $\delta\phi = 2\pi m$

with the mode index m being an integer. The corresponding modes

$$k_m = \frac{2\pi m - \varphi}{L_{\text{eff}}} \tag{2.41}$$

are equally spaced with the mode spacing

$$\delta k = \frac{2\pi}{L_{\text{eff}}}. \tag{2.42}$$

Two-dimensional wave equation approach

The full wave nature is governed by the wave equation [58]

$$\nabla \times \nabla \times \mathbf{E}(\mathbf{r}) = \epsilon(\mathbf{r}) k^2 \mathbf{E}(\mathbf{r}) \tag{2.43}$$

where $\mathbf{E}$ is the electrical field and $\epsilon(\mathbf{r}) = n^2(\mathbf{r})$ is the dielectric function. We solve the wave equation in a planar geometry for TE modes, i.e. $\mathbf{E}(\mathbf{r}) = E_z(\mathbf{r})\mathbf{e}_z$ and $\mathbf{r} = x\mathbf{e}_x + y\mathbf{e}_y$. For the simulations, a FEM [57] with 'open' boundary conditions is employed. The boundaries are taken into account by perfectly matching layers (PMLs) at the edges of the simulation domain [59], see Fig. 2.12. This allows outgoing waves with negligible back reflection.

Equation (2.43) is solved subject to a point-source excitation and modes are monitored by calculating the output power $P_{\text{out}}(k)$ by integration along γ in the polymer region adjacent to the cavity, see Fig. 2.12, for different values of k. The point-source has the appealing feature that it radiates isotropically in a homogeneous space and thus it will in general excite the full spectrum of cavity eigenmodes (except of course from the statistically few having a true node at the exact position of the point-source).

In order to compare to the predicted mode spectrum, the k values are transformed into a mode index

$$m(k) = (kL_{\text{eff}} + \varphi)/2\pi \tag{2.44}$$

and according to Eq. (2.41), $P_{\text{out}}(m)$ is expected to have resonances centered at integer values of m. Fig. 2.13 illustrates this in the case of a point-source excitation at point A, see Fig. 2.12.

The over-all agreement between the full wave simulation and the quasi-1D model is excellent, but from Fig. 2.13 it is also clear that the different peaks are slightly blue-shifted from integer values. The top panels illustrate this for two of the peaks indicated by green and red in the lower panel. This small shift may originate in a slightly modified phase shift at the edge with evanescent field coupling compared to the three other edges of the cavity. The

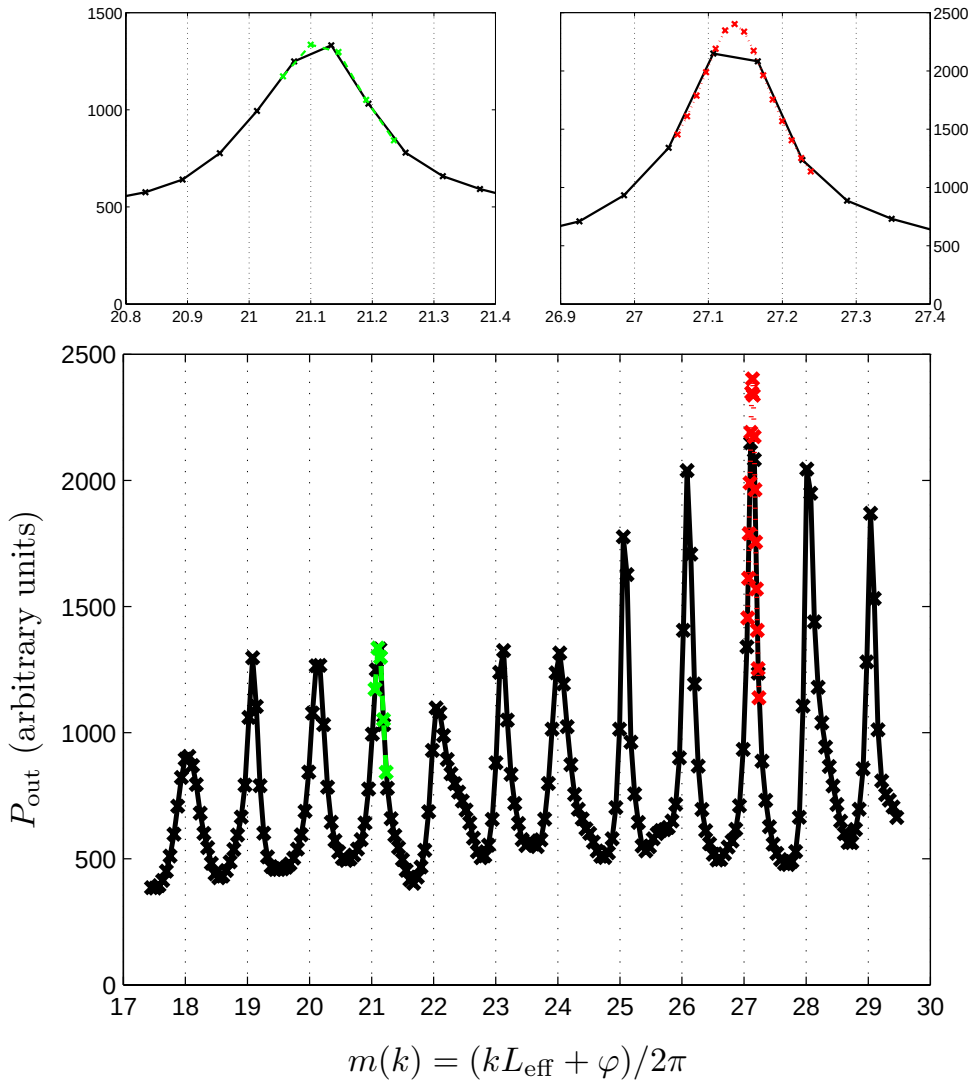

Fig. 2.13: Mode spectrum for a point-source excitation at position A, see Fig. 2.12. The top panels show close-ups with a higher resolution of the respective peaks at $m \sim 21$ and $m \sim 27$ indicated in the lower panel.

small Fresnel reflection may also slightly modify the spectrum compared to the results derived from the quasi-1D model.

Figure 2.13 shows results in the range from $m \sim 18$ up to $m \sim 29$. When further increasing m the pattern of peaks persist with a small tendency that the peaks sharpen. This trend has been investigated up $m \sim 100$ where simulations turn highly computationally demanding (results not shown). How-

ever, since the quasi-1D interpretation does not support a cut-off for increasing m, a spectrum of equally spaced modes is expected to persist for increasing m.

For decreasing m WGMs will typically experience a cut-off because the angles of incidence at some point do not support total-internal reflection. However, as discussed for the quasi-1D model the particular class of modes in the present cavity do not share this property. In fact, in the simulations we have observed the modes down to $m \sim 10$ below which pronounced deviations from the quasi-1D predictions start to emerge. Deviations most likely appear because the polymer-air interface has spatial variations on a length scale comparable to the wavelength of the light. In other words, the ray-tracing picture fails and concepts like total-internal reflection derived from Snell's law do not accurately capture the true wave physics.

In order to verify that the peaks in Fig. 2.13 really do correspond to cavity modes, the corresponding electrical fields at resonance have been studied, see Fig. 2.14. These fields resemble pure eigenfunctions of the resonator while off-resonance fields correspond to linear combinations of a larger number of eigenfunctions. Starting from e.g. the source point, the number of oscillations along one round trip equals m in full agreement with the quasi-1D arguments.

When the cavity is excited at different positions the overall output spectrum is the same such that peaks remain unshifted while changes are observed in the intensity distribution only. The reason is that different positions of the source will excite different linear combinations of eigenmodes (being corre-

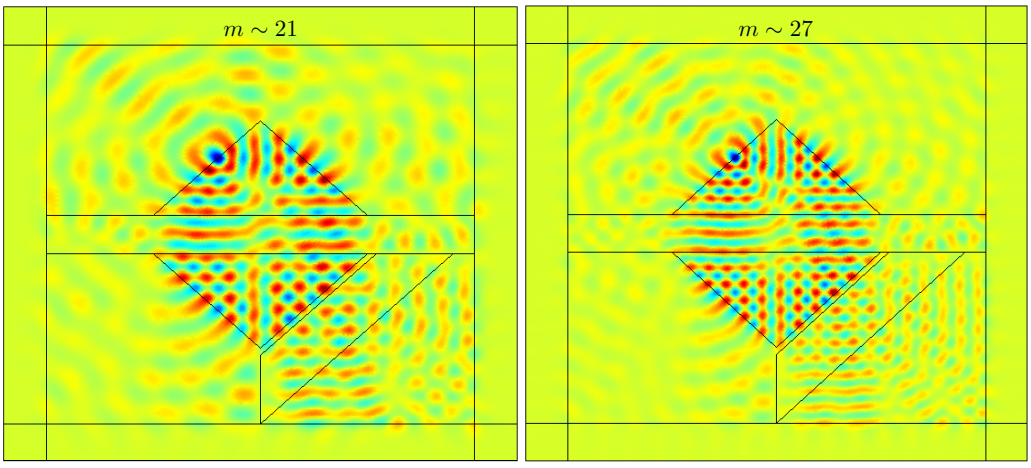

Fig. 2.14: Electrical fields at $m(k) = 21.1000$ and $m(k) = 27.1355$ for a point-source excitation at position A, see Fig. 2.12.

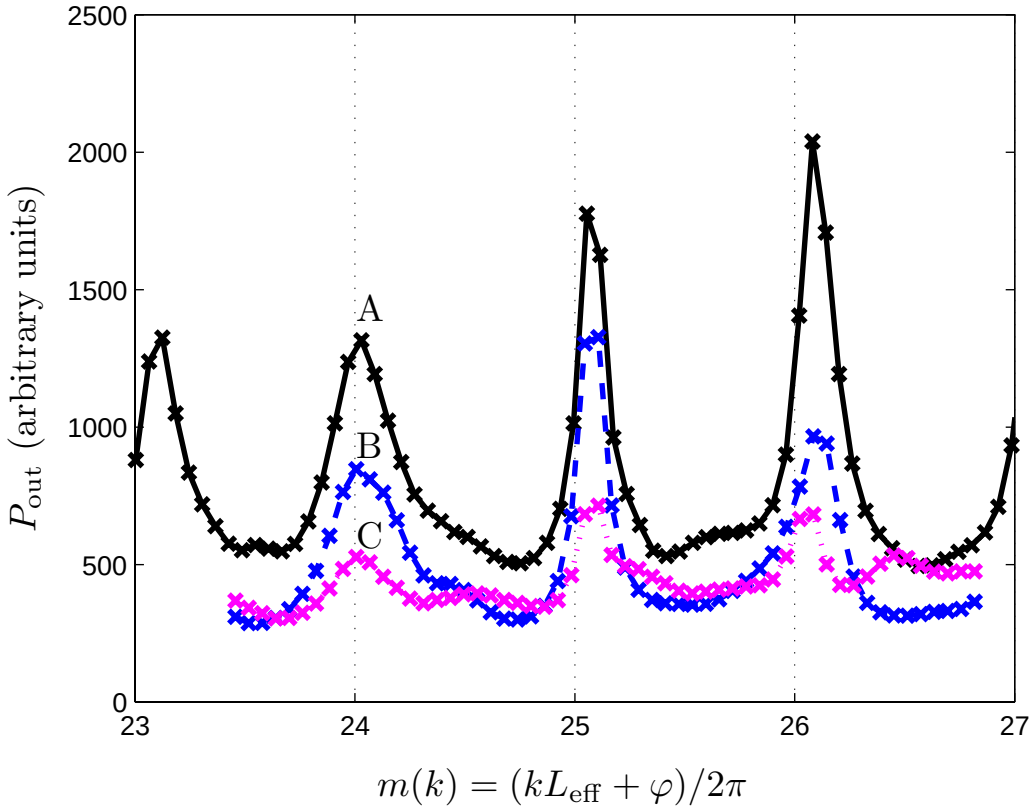

Fig. 2.15: Mode spectra for point-source excitation at positions A, B, and C, see Fig. 2.12.

lated with the intensity level) while the eigenspectrum itself (being correlated with the resonance positions) remains unchanged. Fig. 2.15 illustrates this for different positions of the point source. The spectrum also reveals structure, though very broad with low intensity, in between integer values of $m(k)$. This structure also corresponds to quasi eigenmodes which however are much more poorly confined to the cavity compared to the well-confined modes with integer values of $m(k)$.

Discussion

In this section, finite element simulations are used to study the cavity mode spectrum of a optofluidic dye ring laser with a planar geometry resembling the one studied experimentally in Refs. [40,41]. A full wave study of the TE modes in the cavity has been performed and very good agreement with a quasi-1D plane wave description with resonances corresponding to standing

waves was found.

In principle the simulations allow for an estimate of the quality factor of the modes, but realistic simulations for the experimental device require more details to be taken into account. For instance one would need to include the three-dimensional nature of the device to describe the radiation field accurately and the details of the evanescent field coupling would also influence the quality factor. Such issues add to the difficulty in addressing the dynamics of lasing so in this section, only the passive device has been addressed.

In the simulations, mode indices $m(k)$ up to around 100 are considered while in the experiments the corresponding typical mode index is estimated to be around two orders of magnitude larger. Nevertheless, we are confident that the standing-wave interpretation may be safely extrapolated to the experimental regime [40–42] due to the scale invariance of the wave equation [58] and the fact that this class of modes has no cut-off with respect to increasing mode index.

2.5 Summary

This Chapter introduces the theoretical concepts necessary to understand the design and operation of the optofluidic dye laser devices treated in this thesis. Further, the numerical models developed during this thesis work are described.

Planar dielectric waveguiding which constitutes the cornerstone of integrated optics is introduced, followed by a section concerning DFB lasers with focus on the Bragg condition, FSR, and out-of-plane scattering. The FSR is an important parameter in order to determine the maximum achievable tunability of a DFB laser without mode-hopping. The out-of-plane scattering is a significant loss mechanism for higher order Bragg grating DFB lasers.

A quasi-1D transmission matrix model is developed to aid the design of optofluidic DFB lasers. The model renders a 2D resonator geometry into a quasi-1D model by estimating the refractive indices of the resonator segments as the mode refractive indices. In the SU-8 segments, the mode refractive index of a corresponding infinite planar waveguide is used. For the fluidic resonator segments, the mode refractive index is roughly estimated, since no confined TE-TM mode exists. The model does not account for gain or loss in the laser resonator, as this would require knowledge of the imaginary part of the refractive indices of the materials, which for R6G is strongly dependent on concentration and optical pumping conditions.

Using the quasi-1D model, the laser oscillation condition, the importance of the central $\pi/2$ phase shift, and the optofluidic refractive index tunability

of the lasers are discussed.

The final part of this Chapter concerns FEM simulations of the cavity modes of an optofluidic dye ring laser [48]. A quasi-1D ray tracing model to predict the spectral position of the cavity modes is compared to 2D full wave simulations. The cavity modes are shown to correspond to standing waves in the resonator and the 2D full wave simulations support a ray-tracing view. In order to efficiently calculate the quality factor of the resonator, the three-dimensional nature of the device should be taken into account.

3. MATERIALS

This Chapter introduces the most important materials and material parameters relevant to the work presented in this thesis. The focus is on the chosen laser dye, rhodamine 6G (R6G), the polymer SU-8 which was used as main building blocks in the fabricated optofluidic dye lasers, and the thermoplast polymethylmethacrylate (PMMA) which was used as adhesive layer in polymer wafer bonding.

3.1 Laser dye: Rhodamine 6G

In this work, the organic dye Rhodamine 6G (R6G) has been used as active medium in optofluidic dye lasers. R6G belongs to the class of xanthene dyes, also including rhodamine B and fluorescein, which are very efficient and constitute the most popular type of dyes used in applications today, covering the wavelength region 500 – 700 nm (see [24], Chapter 4).

The molecular structure of R6G is seen in Fig. 3.1. R6G is purchased as a powder, and is dissolved in a liquid prior to use in optofluidic devices. R6G is also known as Rhodamine 590, Basic Rhodamine Yellow, and C.I. 45160, depending on supplier and application. R6G is a widely used laser dye, since it is relatively cheap, easy to use, and not-so-toxic. In this work,

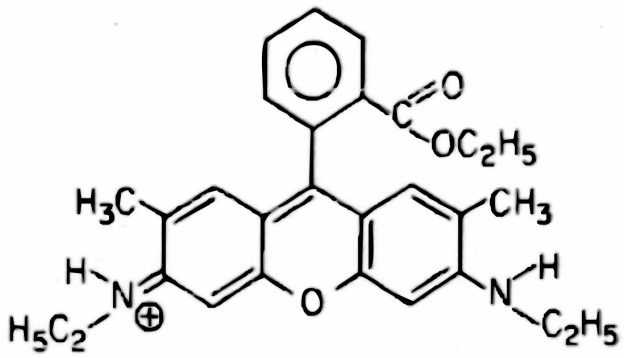

Fig. 3.1: The molecular structure of R6G. From [24].

R6G functions as a model system, demonstrating the functionalities of the optofluidic devices, i.e. other dyes covering a different spectral region can easily be applied.

Energy levels

The molecular structure of R6G, see Fig. 3.1, includes many conjugated double bonds, i.e. alternating single and double bonds and aromatic hydrocarbons. The conjugated double bonds have the effect of lowering the energy gap between the highest occupied molecular orbital and the lowest unoccupied molecular orbital (HOMO/LUMO gap). This enables the absorption of R6G at visible wavelengths through delocalized molecular π orbitals.

The energy level diagram of a typical dye molecule such as R6G is shown in Fig. 3.2. The diagram resembles that of a two-electron atom where the electronic energy levels are divided into singlet and triplet states due to angular momentum coupling. The molecular electronic ground state is denoted S_0, the excited singlet states $S_1, S_2, \ldots$, and the triplet states $T_1, T_2, \ldots$. Intersystem crossing between singlet and triplet states via a spin-flip event is 'forbidden' in the electric dipole approximation according to the $\Delta S = 0$ selection rule.

The molecular energy levels are broadened by vibrational and rotational states of the molecule. Further broadening is caused by interactions with the environment through collisions with solvent molecules. The broad molecular energy levels enable continuous wavelength tuning of dye lasers in the visible region. For a detailed account on the molecular energy states of dye molecules, see [24] Chapter 1.

Laser emission from organic laser dyes is achieved through a four level process. As indicated in Fig. 3.2, stimulated emission occurs on the molecular transition from the lowest vibrational and rotational state of the first excited singlet state S_1 to a higher vibrational and rotational state of the ground state S_0.

In step 1 of the lasing cycle, molecules in the ground state S_0 are optically pumped to a vibrational and rotational energy state above the upper laser level by an external optical pump source, for R6G typically a frequency doubled Nd:YAG laser operating at 532 nm. Step 2 is a fast transition on the timescale of picoseconds to the upper laser level which is the lowest vibrational and rotational energy state of the first excited singlet state S_1. The transition is usually radiationless, and the excess energy is delivered to the surroundings through collision energy transfer.

The upper laser level S_1 has a long lifetime of a few nanoseconds, consequently the molecules 'pile up' and the level functions as a bottleneck. In

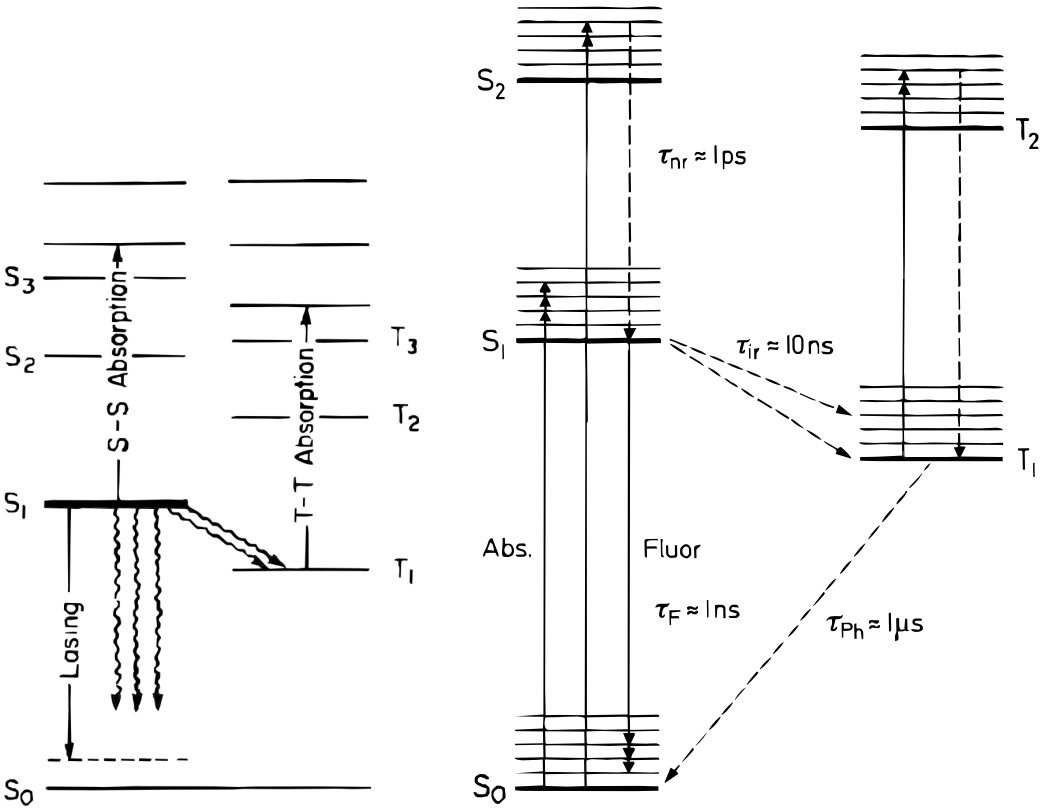

Fig. 3.2: Energy level diagrams for a typical dye molecule. **Left:** Overview showing the division in singlet and triplet states. **Right:** Scheme for 4-level lasing using laser dyes. From [24].

step 3, the molecules decay from the upper laser level to the lower laser level which is a higher vibrational and rotational energy state of the ground state. In step 4, the state is quickly depleted on the timescale of picoseconds and the molecules complete the lasing cycle through radiationless relaxation to the ground state S_0.

This lasing scheme enables the build-up of a large population inversion between the laser levels which is necessary for optical amplification (stimulated emission). When a positive population inversion has been realized and a resonant photon interacts with one of the molecules in the upper laser level, stimulated emission can occur. The photon is emitted as an exact copy of the incident photon, amplifying the radiation field, and the molecule is left in the lower laser level.

Since the lower laser level is not the ground state S_0, it is not necessary to excite the majority of the molecules, but only to achieve a population inversion between the upper and lower laser levels which is considerably easier.

As the energy gap between the two laser levels is smaller than the energy gap of the pumping transition, see Fig. 3.2, the emission spectrum of the dye is red-shifted in wavelength relative to the absorption spectrum. This shift in wavelength is called the Stokes shift.

As sketched in Fig. 3.2, excited molecules can undergo a spin-flip event and decay via forbidden transitions from excited singlet states to triplet states. As the first excited triplet state T_1 has a long lifetime compared to the singlet states on the timescale of microseconds, these decay channels result in loss of molecules when aiming for a positive population inversion between the laser levels, and further triplet-triplet transitions increase absorption of pump light. By continuous pumping, the T_1 state would deplete the upper laser level S_1 and hinder laser action. To avoid this, a pulsed optical pump source is used, allowing all the molecules to relax to the ground state S_0 between the pump pulses.

Fluorescence quantum yield

The fluorescence quantum yield ϕ, or quantum efficiency, of the dye molecules is defined as the fraction of the number of emitted photons to the number of absorbed photons. The quantum yield of the dye strongly depends on the dye molecule environment through the dye concentration and dye-solvent interactions.

The dissolved dye molecules are very sensitive to their environment through dye-solvent interactions, hence the choice of solvent strongly influences the dye laser characteristics. Most dye molecules are polar and since their dipole moment increases upon excitation to the first excited singlet state, polar solvents are well-suited to dissolve them [60].

In general, an increase in solvent polarity introduces an increase of the Stokes shift and a shift of the dye gain spectrum towards longer wavelengths. Consequently, the gain bandwidth and output lasing energy increase. Polar solvents such as ethanol, methanol, and water may appear optimal for many dyes in the visible range [60]. In addition, other solvent properties such as, refractive index, viscosity, and acidity (pH) are important for the environment of the dye molecules.

The quantum yield of R6G dissolved in ethanol has been measured by Bojarski *et al.* [61] and López Arbeloa *et al.* [62] and their results are shown in Fig. 3.3. The Figure shows a large quantum yield close to unity of R6G molecules in dilute solutions. At concentrations c around 10^{-2} mol/L, fluorescence quenching, i.e. a rapid drop of the quantum yield, is observed. The drop is attributed to the formation of non-luminescent dimers and trimers [61, 62]. The absorption spectrum of the combined dimer molecules

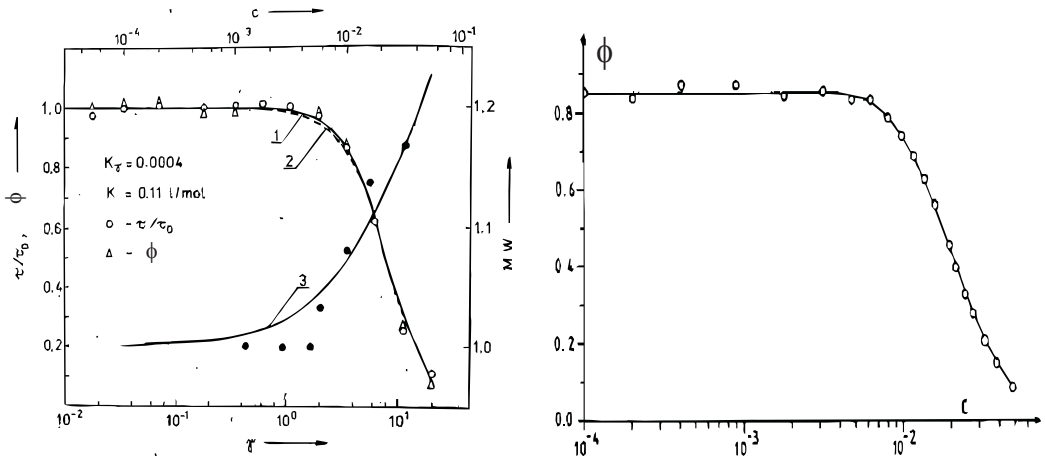

Fig. 3.3: The quantum yield ϕ of R6G dissolved in ethanol as a function of concentration. At $c \sim 10^{-2}$ mol/L a rapid drop of ϕ is observed. **Left**: The measurements of ϕ are denoted by $\triangle$ and are mapped on the left axis as a function of concentration (top axis, mol/L). Reproduced from [61]. **Right**: Measurements performed at 20°C at high concentrations c [mol/L]. Reproduced from [62].

is changed, and the probability to excite the dimer-molecule to the first excited state (usable for lasing) is reduced in favor of the second excited state (see [24], Chapter 1).

Dye-solvent interactions strongly influence the optical gain and quantum yield of R6G. The gain is mainly affected through non-specific interactions due to dispersion and hydrogen bonding, as studied by Govindanunny and Sivaram [63]. The emitted laser light is strongly dependent on solvent, through differences in quantum yield and triplet state absorption which is influenced by the presence of molecular oxygen, as investigated by Korol'kova *et al.* [64].

Lopez Arbeloa and Rohatgi-Mukherjee [65] thoroughly investigated the influence of solvents on the emission from rhodamine B which is similar to R6G in molecular structure. They studied emission from the different pH-dependent ionic forms of the molecules. The Kosower polarity parameter Z is a measure of how polar a solvent is, see [66] for a rigorous definition.

The results in [65] show that the quantum yield of rhodamine B is higher in solutions of ethanol $\phi = 0.65$ than ethylene glycol (ethane-1,2-diol) $\phi = 0.51$ and water $\phi = 0.28$. Ethanol has a polarity of $Z = 333$ kJ/mol, low viscocity at 25°C $\eta = 1.04$ mPa s, and a high dissociation constant $\mathrm{pK_a} = 18.9$ (weak acid). Ethylene glycol has a slightly higher polarity $Z = 356$ kJ/mol, high viscosity $\eta = 15.66$ mPa s, and a dissociation constant of $\mathrm{pK_a} = 15.8$.

Water is highly polar $Z = 395$ kJ/mol, has a low viscosity $\eta = 0.83$ mPa s, and lower dissociation constant $\mathrm{pK_a} = 14.0$.

In aqueous solution, R6G molecules form dimers which absorb light at the laser wavelength [67, 68], rendering water unsuitable as solvent. For acetone which is a non-polar solvent $Z = 275$ kJ/mol [66], with high dissociation constant $\mathrm{pK_a} = 16.5$ [69] and low viscosity $\eta = 0.3$ mPa s [69], the quantum yield is high ($\phi \sim 1$ for R6G) but the emitted lasing energy is minute due to photolysis of acetone which can lead to quenching of fluorescence or short-lived particles that absorb the emitted radiation [64].

The above illustrates some of the many solvent properties that influence dye-solvent interactions and the success for a dye solvent.

Absorption and emission characteristics

The interaction between light and dye molecules is characterized by absorption, spontaneous emission, and stimulated emission (lasing). The molecular singlet and triplet states all contribute significantly to the spectral absorption and emission characteristics. Further, the interaction between dye molecules (quenching) and the surroundings (dye-solvent interactions) play an important role.

An absorption process can be characterized by the molecular absorption cross section $\sigma(\lambda)$ defined by (see [24], Chapter 2)

$$I(\lambda) = I_0(\lambda)\ \exp[-N\,\sigma(\lambda)\,\ell] \tag{3.1}$$

where $I_0(\lambda)$ and $I(\lambda)$ are the intensities of the light before and after passing through an absorbing sample of length ℓ, respectively. N is the number density of molecules, i.e. the number of molecules per volume, given by $N = N_A\,c$ where N_A is the Avogadro constant and c is the concentration. If c and ℓ are measured in mol/cm^3 and cm, respectively, σ has the dimension of cm^2 and effectively measures the area of an absorbing molecule. The Beer-Lambert-Bouguer law [69] relates σ to the molar extinction coefficient α_m as

$$\alpha_\mathrm{m}(\lambda) = N_A\,\sigma(\lambda) \tag{3.2}$$

Note, that α_m is typically given in L mol^{-1} cm^{-1}.

Fig. 3.4 shows the cross sections for various processes in R6G [24]. The cross section for the molecular transition $S_0 \rightarrow S_1$ is denoted σ_S. The long wavelength tail of σ_S is shown in an enlarged view around $\lambda = 600$ nm. The fluorescence signal $E(\lambda)$ for the transition $S_0 \leftarrow S_1$ is normalized through $\int E(\lambda)d\lambda = \phi$ with $\phi = 0.92$. The data for $\sigma_S(\lambda)$ and $E(\lambda)$ have been obtained from R6G in an aqueous solution of concentration $c = 10^{-4}$ mol/L

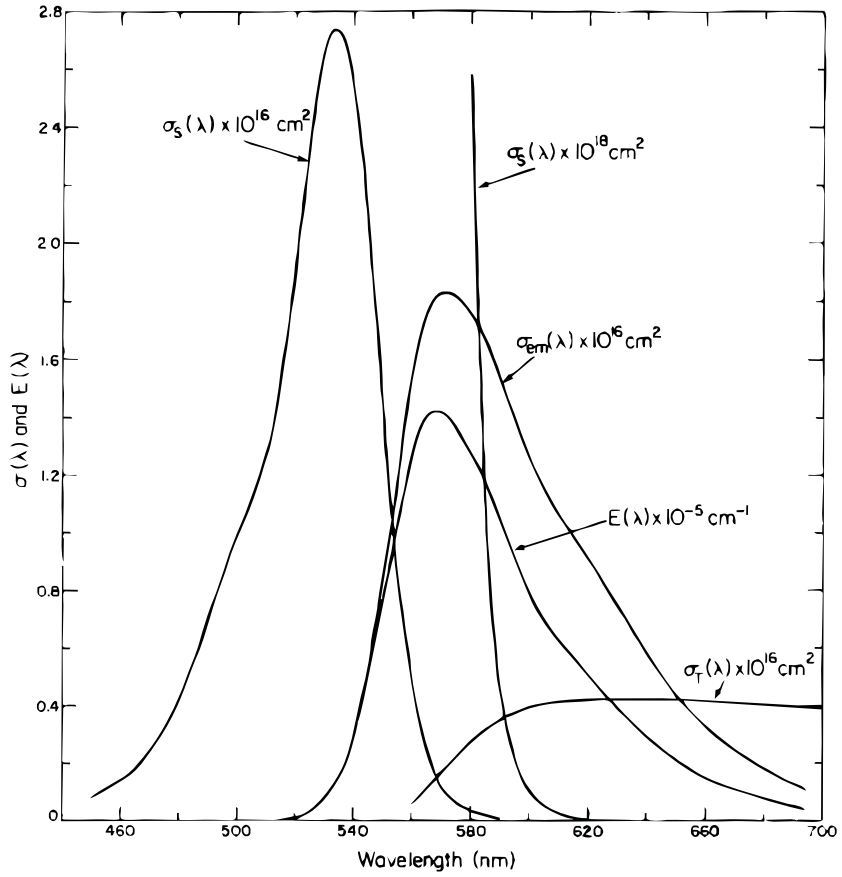

Fig. 3.4: Absorption and emission cross-sections for R6G solutions of concentration $c = 10^{-4}$ mol/L. Singlet absorption cross section $\sigma_S(\lambda)$, spontaneous emission spectrum $E(\lambda)$, and calculated stimulated emission cross section $\sigma_{\mathrm{em}}(\lambda)$ obtained for R6G in an aqueous solution with an added surfactant. Triplet absorption cross section $\sigma_T(\lambda)$ for an ethanolic solution. From [24].

with an added surfactant. From $\sigma_S(\lambda)$ and $E(\lambda)$, the stimulated emission cross section $\sigma_{\mathrm{em}}(\lambda)$ has been calculated.

For increasing intensities of the optical pumping of the dye molecules at a wavelength close to the absorption maximum, the absorption curve (labeled σ_S) decreases and the emission curve (labeled σ_{em}) grows due to increased population inversion, thus the gain grows. Due to the Stokes shift, the gain maximum increases and moves towards shorter wavelengths. For a laser with modes of equal cavity losses, the laser will oscillate in the mode which is located closest to the gain maximum.

The absorption spectrum $\sigma_T(\lambda)$ due to triplet state transitions $T_1 \rightarrow T_n$ for an ethanolic solution of R6G is also shown in Fig. 3.4. Although the absorption and emission spectra for R6G are solvent dependent, the overall shape is not expected to differ greatly. In a continuous wave pumping configuration of R6G, some dye molecules will decay into the triplet states which disable lasing, since the emission in the spectral region of $\sigma_{\mathrm{em}}(\lambda)$ is readily absorbed by the molecules in the triplet states.

The penetration depth or skin depth is the characteristic length a plane wave penetrates into a material before it is absorbed, more precisely the distance it takes to reduce the amplitude of the electric field by a factor of $1/e$, see Chapter 9.4 in [71], or [69]. The penetration depth δ is defined from the molar extinction coefficient as

$$\delta(\lambda) = \frac{1}{\alpha_{\mathrm{m}}(\lambda)\, c} = \frac{1}{N_A\, \sigma(\lambda)\, c} \tag{3.3}$$

Table 3.1 shows estimated values for the penetration depth δ for R6G solutions of different concentration. Values for the molar extinction coefficient and absorption cross section at the absorption maximum ($\lambda \sim 530$ nm) are obtained from different sources for different solvents, typically in dilute solutions, in order to estimate the range of δ.

Generally, the penetration depth is in the micron-scale range for concentrations in the range 10^{-2} mol/L $-$ 10^{-4} mol/L, however, δ varies significantly due to the inverse proportionality of δ and $\sigma\, c$, see Eq. (3.3), and is also dependent on the solvent.

For the concentration 2×10^{-2} mol/L used in the devices of Chapter 5, δ is

Solvent	$\alpha_{\mathrm{m}}^{\mathrm{max}}$ [L mol^{-1} cm^{-1}]	σ_S^{max} [cm^2]	c [mol/L]	δ [µm]
Water ([24], p. 89)	1.63×10^5	$\mathbf{2.7 \times 10^{-16}}$	10^{-2}	6
			10^{-3}	62
			10^{-4}	615
Ethanol [70]	$\mathbf{6.4 \times 10^4}$	1.1×10^{-16}	10^{-2}	16
			10^{-3}	156
			10^{-4}	1563
Ethanol [60]	$\mathbf{1.16 \times 10^5}$	2.0×10^{-16}	10^{-2}	8
			10^{-3}	83
			10^{-4}	833

Tab. 3.1: Penetration depth δ for different concentrations c of R6G in different solvents, evaluated through Eq. (3.3). Values for the molar extinction coefficient α_{m} and absorption cross section σ_S at the absorption maximum are obtained from different sources (cited values in boldface).

much larger than the height of the structures. In Chapter 6, a concentration of 2×10^{-4} mol/L is used which yields a penetration depth comparable to the device dimensions. In both cases, the optical pumping intensity throughout the device can be assumed to be uniform.

3.2 Polymer: SU-8

The main material used as building blocks in the fabricated optofluidic dye lasers is the polymer SU-8. In lithographic processes, SU-8 can be structured by UV light, electrons, and x-rays. SU-8 is a negative-tone resist, i.e. the exposed pattern remains after the cross-linking reaction and subsequent development. For UV lithography, the i-line of the Hg spectrum (365 nm) is usually used for the exposure.

SU-8 was developed and patented by IBM in the 1980'ies, the first results on SU-8 as a high aspect ratio thick film resist were published in 1995 by LaBianca and Gelorme [72]. In 1997, further results focusing on MEMS applications were published at the IEEE MEMS conference [73] and in the first journal article on SU-8 [74]. Today, SU-8 is commercially manufactured by MicroChem (`www.microchem.com`).

The molecular structure of the SU-8 monomer is shown in Fig. 3.5. The '8' in the name refers to the, on average, eight epoxy groups ($-CH_2-CHOCH_2$) in the SU-8 monomer. The cross-linking reaction is a two step process: The polymerization is initiated by the exposure during which a strong acid is generated from an added photo acid generator. The acid acts as a catalyst

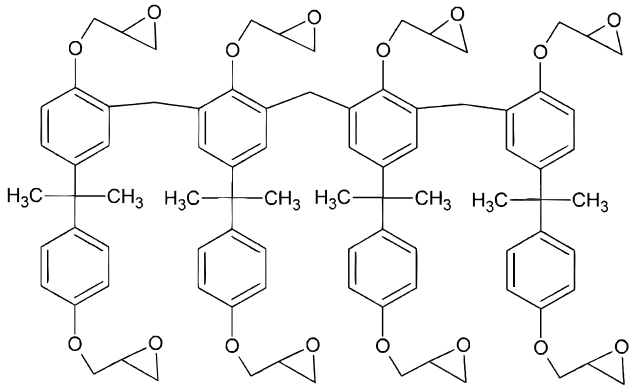

Fig. 3.5: The molecular structure of SU-8. Exposure initiates thermally driven catalytic epoxy cross-linking of neighboring molecules. Sketch generated using ACD/ChemSketch, formula according to [72].

for the thermally driven epoxy cross-linking [75, 76]. A normal SU-8 process consists of: Spin-coating, soft bake, exposure, post-exposure bake, and finally development.

SU-8 has a variety of interesting properties which makes it an attractive material for a wide range of applications: It is chemically and mechanically stable, transparent for visible wavelengths, and has shown heat resistance to temperatures above 200°C.

For the SU-8 2000 series, cyclopentanone is used as solvent. Depending on SU-8 solid content and spin-coating parameters, film thicknesses in the interval from approximately 100 nm to more than 200 µm is obtained. The developer for SU-8 is propylene glycol monomethyl ether acetate (PGMEA). The possibility to spin-coat and structure SU-8 films of thicknesses ranging from the nanometer scale to the millimeter scale enables the use of SU-8 for a wide range of applications. The relatively low cost of SU-8 based devices is attractive for creating disposable, single use devices.

Fig. 3.6 shows transmission and absorption spectra of SU-8 2000 films. The left part shows the transmission at different stages of the fabrication process (film thickness not available, soft bake 5 minutes at 95°C, hard-bake 30 minutes at 300°C) [75]. The transmission characteristics below approximately 450 nm change during the fabrication process. The right part shows the absorption spectrum of SU-8 2000 measured with a spectrophotometer from a sample contained in a 1 cm wide quartz vial (baking procedure not available). Note, that the wavelength scale continues into the infrared. The results show low absorption for wavelengths from approximately 450 nm − 1100 nm. The absorption below 450 nm is due to the photochemical

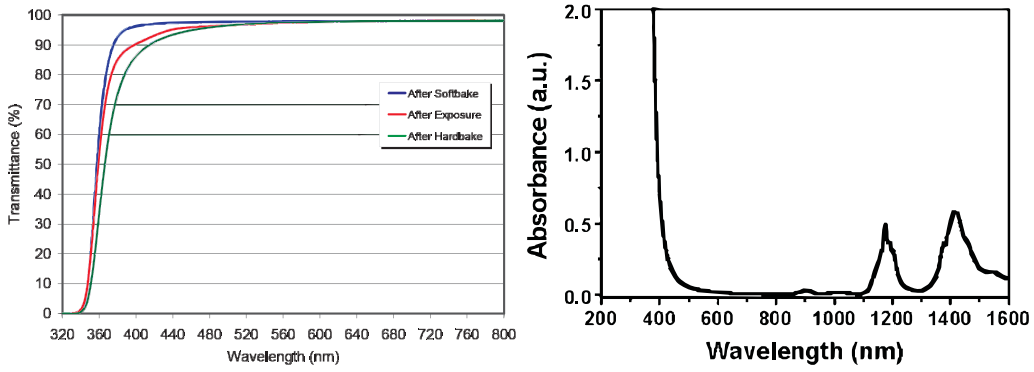

Fig. 3.6: Transmission and absorption spectra of SU-8. **Left**: Transmittance at different steps in the fabrication. From [75]. **Right**: Absorption of SU-8, low absorption is observed in the visible part of the spectrum. From [77].

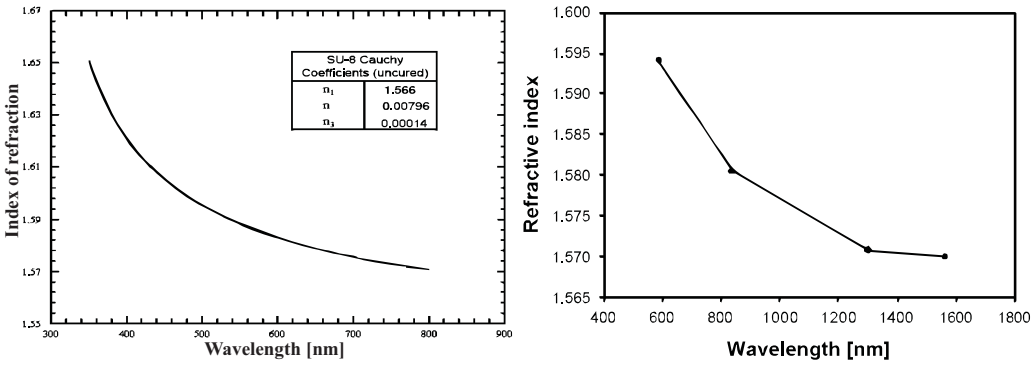

Fig. 3.7: Dispersion of SU-8. **Left**: Uncured SU-8. Reproduced from [75]. **Right**: 40 μm thick film after hardbake treatment. From [78].

cross-linking reaction and the absorption in the region 1100 nm – 1300 nm is due to vibrational overtones of the C – H bonds [77].

Fig. 3.7 shows measurements of the refractive index of SU-8 as a function of wavelength. A clear dispersion is observed. The left part shows the data from the supplier [75] for uncured SU-8 2000 (film thickness not available). The right part shows a measurement of the refractive index of a 40 μm thick film of SU-8 grade 25 [78]. The film was softbaked and post-exposure baked at 95°C and subjected to a hardbake heating treatment at 150°C for 4 hours subsequent to development.

Fig. 3.8 shows how the refractive index depends on the hardbake temperature (film thickness ~ 6 μm). The refractive index is seen to decrease with

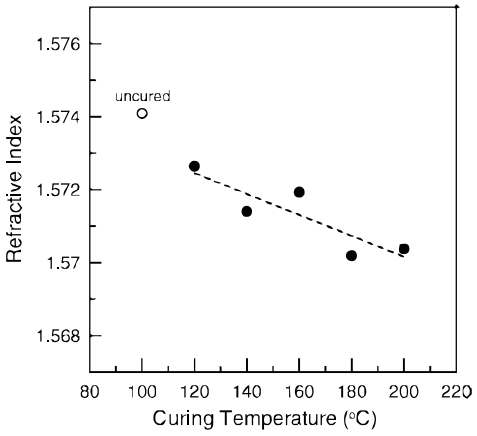

Fig. 3.8: SU-8 refractive index as a function of hardbake temperature. From [79].

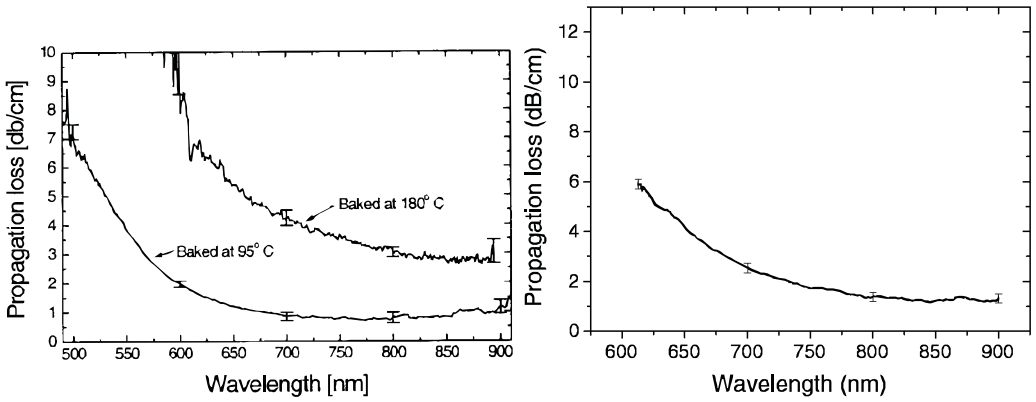

Fig. 3.9: Propagation loss of SU-8 waveguides. The propagation loss is less than 2 dB/cm for wavelengths above 600 − 700 nm. **Left**: 100 µm thick waveguides. From [34]. **Right**: 10 µm thick waveguides with PMMA cladding. Reproduced from [80].

hardbake temperature, possibly due to an increase in molecular weight [79].

Fig. 3.9 shows the propagation loss of different SU-8 waveguides. The left part shows results for 100 µm thick waveguides with a SU-8 refractive index of 1.59 (measured at 633 nm). The baking temperature refers to an increase in propagation loss due to thermal degradation over time. Propagation losses below 2 dB/cm are measured for wavelengths above 600 nm [34]. The right part shows propagation loss measurements of 10 µm thick straight waveguides of SU-8 with PMMA cladding. The results show a propagation loss below approximately 2 dB/cm for wavelengths above 700 nm [80]. The increase in propagation loss for shorter wavelengths may be due to absorption in the SU-8, cf. Fig. 3.6. The authors do not comment on the loss distribution between imperfections and surface roughness.

As the results of Figs. 3.6–3.9 show, the optical properties of SU-8 strongly depend on the processing parameters, especially on exposure dose and baking parameters.

3.3 Polymer: PMMA

In this thesis work polymethylmethacrylate (PMMA) was used as adhesive layer in polymer wafer bonding. The chemical structure and dispersion is shown in Fig. 3.10. The refractive index of PMMA of molecular mass 950 kDa is approximately 1.49 for wavelengths above 500 nm. PMMA can be dissolved in anisole and is a popular resist for electron beam lithography (EBL) and

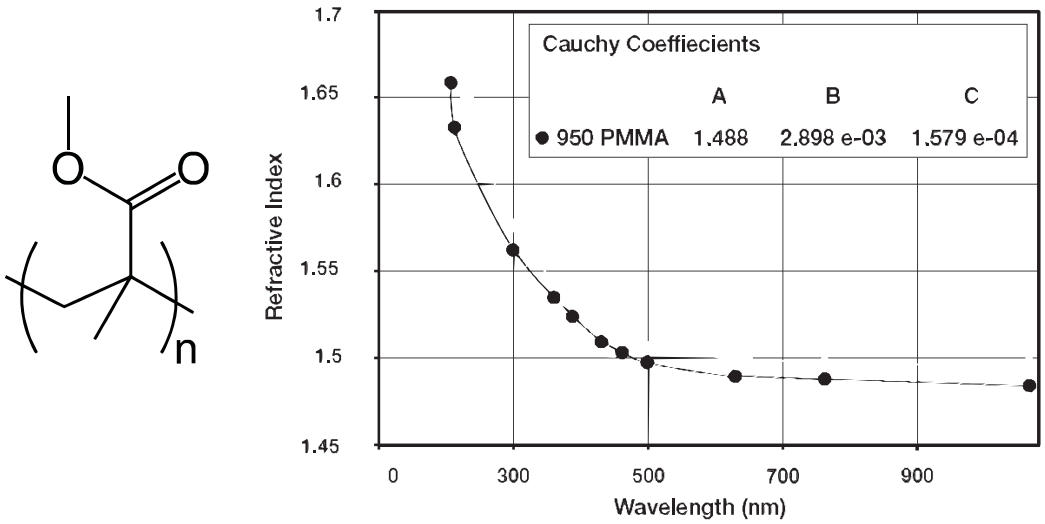

Fig. 3.10: PMMA. **Left**: Molecular structure. From [69]. **Right**: Dispersion of PMMA of molecular mass 950 kDa. The refractive index is approximately 1.49 for visible wavelengths. Reproduced from [82].

NIL.

Upon exposure with electrons, the polymer chains of PMMA are broken, and the exposed PMMA is dissolved during development, hence PMMA is a positive-tone EBL resist. Nanostructures of sub-10 nm dimensions have been demonstrated using 30 kV acceleration voltage EBL and cold development [81].

In addition, the thermoplastic nature of PMMA enables the use as a NIL resist. PMMA has a glass transition temperature of approximately 105°C, and imprints are typically performed at 175°C with an imprint pressure of a few MPa. Imprinted structures of sub-10 nm dimensions in PMMA have been demonstrated with a period of 40 nm [83].

PMMA has found widespread use in numerous applications. In a microfabrication context it is mainly used as high resolution resist for EBL and NIL. PMMA is also known as e.g. 'acrylic glass' or 'plexiglass' and everyday examples of PMMA include aquariums, lenses for headlights in automobiles, spectator protection in ice hockey stadiums, aircraft windows, human implants, and 1960–1970s space-age furniture [69].

In the fabricated optofluidic dye laser devices, PMMA was used to seal the fluidic channels and simultaneously functioned as the cladding of a polymer waveguide structure with a core of SU-8 on a SiO_2 substrate. The thermoplastic nature of PMMA facilitated adhesive wafer bonding of SU-

8 and PMMA by heating the two substrates to 140°C which rendered the PMMA highly viscous and applying pressure, as described in [80]. PMMA of molecular mass 950 kDa was supplied by MicroChem (`www.microchem.com`).

3.4 Summary

This Chapter introduces the main materials used in the work presented in this thesis: R6G, SU-8, and PMMA. Emphasis is on the optical properties, as the materials are used in optofluidic dye lasers based on planar waveguiding structures.

For R6G, the 4-level lasing scheme and energy level structure is described, as well as the concentration-dependent fluorescence quantum yield and the complicated yet strong influence of dye-solvent interactions. Absorption and emission characteristics are discussed and the penetration depth of pump light in a R6G solution is estimated. In this thesis work, R6G functions as a model system to demonstrate the functionalities of the optofluidic devices and can easily be exchanged with another laser dye in order to suit a specific application.

The basic structure and processing of SU-8 is described. Results from the literature on the wavelength-dependent absorption, refractive index, and waveguide propagation losses are presented. The optical properties of SU-8 are strongly dependent on the process parameters, especially exposure dose and baking parameters. SU-8 was chosen as the main building blocks for the fabricated optofluidic dye lasers, as it has optical properties suitable for planar polymer waveguides. Further, SU-8 is chemically and mechanically stable and is easily structured by electrons and UV light.

PMMA is a popular resist for EBL and NIL. In this thesis work, PMMA is used for adhesive wafer bonding of the polymer fluidic channels. Further, the PMMA layer also serves as top cladding of the polymer waveguide structures with SU-8 core. The molecular structure, wavelength-dependent refractive index of PMMA, and the SU-8/PMMA polymer bonding procedure are described.

4. FABRICATION

This Chapter describes the main nanofabrication methods used in this thesis work: Electron beam lithography (EBL), combined electron beam and UV lithography (CEUL), and thermal nanoimprint lithography (NIL). During this thesis work, CEUL in SU-8 has been developed and applied in the fabrication of optofluidic dye laser devices as well as stamps for NIL. The main results on CEUL and NIL presented in this Chapter, behind which I have been the driving force, have been published in *Microelectronic Engineering*, volume **84**, pages 1058–1061 (2007) [49].

4.1 Electron beam lithography

Electron beam lithography (EBL) is a top-down lithographic technique where electrons are used to expose a polymer resist material. A schematic drawing of an EBL tool is shown in Fig. 4.1. Electrons are extracted from a filament and are focused on a substrate which is positioned on a mechanical stage. Since electrons are charged particles, a series of electromagnets are used as lenses to focus and position the electron beam. Apertures are used for shaping the beam and the whole column is kept under vacuum conditions to prevent scattering [84].

In photolithography, the resolution is limited by diffraction of light which is proportional to the wavelength of the light. For electrons, the (non-relativistic) de Broglie wavelength λ_e depends on the acceleration voltage $\mathcal{U}$ as

$$\lambda_e = \frac{h}{p} = \frac{h}{\sqrt{2m_0 e\,\mathcal{U}}} \tag{4.1}$$

where h is Planck's constant, p is the electron momentum, m_0 is the electron mass, and e is the electron charge. A high acceleration voltage yields a small de Broglie wavelength ($\lambda_e \ll 1$ Å) and leads to a small beam size, thus the resolution is not limited by the wavelength. Beam-sizes down to 1 nm can be achieved, limited by the electromagnetic lenses. The electron beam is computer controlled, rendering EBL a high-resolution, flexible, and reliable nanofabrication method [84].

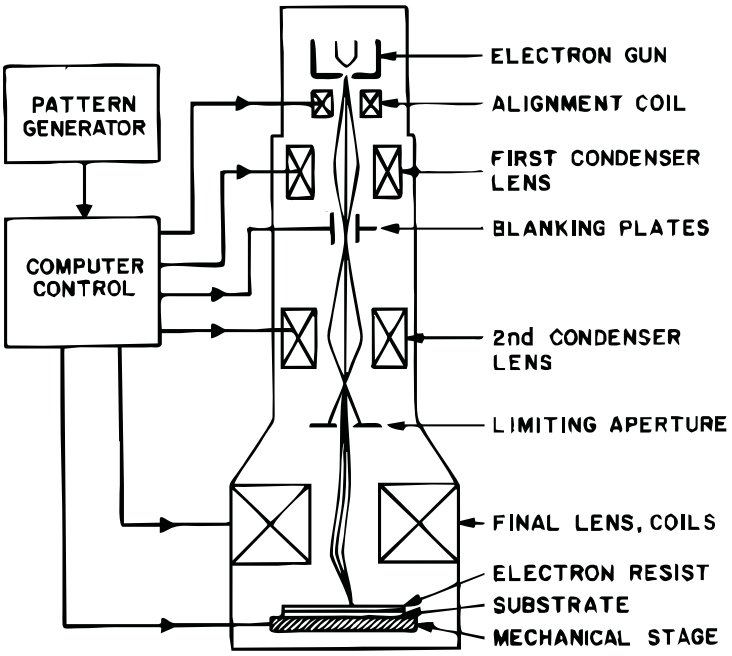

Fig. 4.1: Sketch of EBL system. The electron beam is shaped and focused using electromagnets and apertures. The position of the electron beam is scanned across the substrate. From [84].

The costs of EBL are high due to the need for high vacuum and precision electron focusing, further, the throughput is low since only one pixel can be exposed at a time in a serial fashion. Due to these disadvantages, the use of EBL in commercial applications is, in general, not viable.

A resolution of a few nanometers can be obtained, limited by electron-electron collisions (scattering), but also influenced by resist properties and processing. The electrons are subjected to forward and backward scattering and a large fraction of the incident high-energy electrons penetrate through the resist and into the substrate.

Fig. 4.2 shows how electrons incident on a resist-substrate system are scattered in both forward and backward directions. The left part shows the simulated trajectories of 100 electrons ($\mathcal{U} = 20$ kV) incident on a 400 nm thick PMMA film on a Si substrate (projected onto the xz-plane) [84]. The right part shows the normalized distributions of the forward and backscattered electrons at the resist-substrate interface. Due to electron backscattering, the resist is effectively exposed several micrometers away from the center of the beam. This is denoted the proximity effect and means that electron exposure at one position will influence the exposure at neighboring positions.

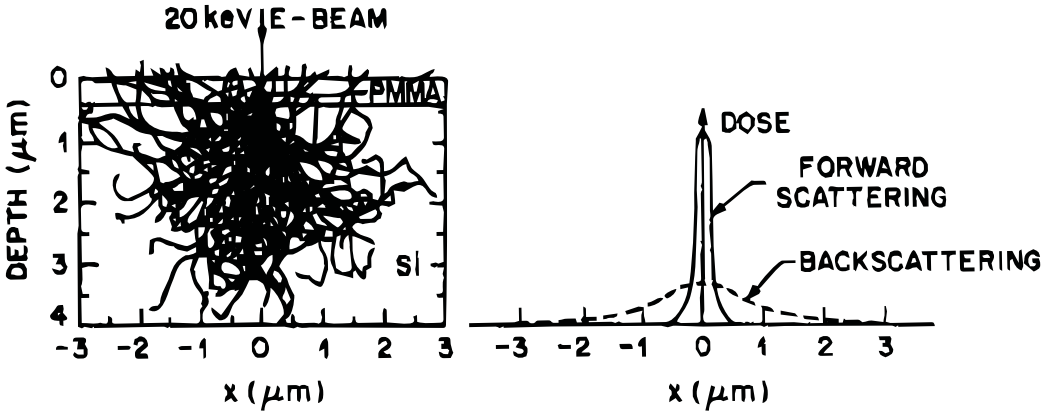

Fig. 4.2: Electron scattering giving rise to the proximity effect. **Left**: Computed trajectories of 100 electrons incident on a 400 nm thick PMMA film on a Si substrate. **Right**: Dose distribution of the forward and backward scattering electrons at the resist-substrate interface. Reproduced from [84].

The proximity effect determines a limit for the minimum spacing between pattern features.

The resist sensitivity is characterized by the exposure dose $\mathcal{D}$ which measures the number of received electrons per unit area, typical doses are in the range $\mu C/cm^2 - mC/cm^2$. The dose is calculated as

$$\mathcal{D} = \frac{I\,\Delta t}{A} \tag{4.2}$$

where I is the beam current, Δt is the dwell time of the electron beam determined by the deflection rate of the EBL system, and A is the exposed area for a single beam step, e.g. 20×20 nm^2. Note, that A is typically significantly larger than the area of the focused electron beam spot due to the proximity effect. There is a trade-off between beam current and step size in order to obtain high resolution and short exposure time. A higher current decreases the exposure time, however, at the cost of a larger beam step size (keeping $\mathcal{D}$ constant), i.e. lower resolution [85].

For the $\mathcal{U} = 100$ kV EBL system at DTU (JEOL-JBX9300FS), the smallest achievable spotsize of the focused electron beam is 4 nm and the maximum deflection rate is 25 MHz, i.e. the minimum dwell time is $\Delta t_{\min} = 1/\,(25\text{ MHz}) = 40$ ns. For a given resist, the beam current I is held fixed, the dwell time is minimized $\Delta t = \Delta t_{\min}$, and the dose is varied by changing the spot size, since this requires less calibration of the EBL system than changing the beam current.

Both positive tone and negative tone resist materials for EBL are available. In positive tone resists such as PMMA and ZEP, the bonds of the polymers are broken during exposure and the exposed areas are dissolved during development. In negative tone resists such as SU-8 and calixarene-based resists, e.g. TEBN-1, new bonds in the exposed areas are formed, and the written pattern remains after development.

The proximity effect is especially pronounced for sensitive resists such as SU-8. The proximity effect can be reduced by calculating the total dose received for each area of a design and accordingly adjusting the dose as a function of position in the design. Proximity correction was not used in the work presented in this thesis, since the computer software is expensive and calculations time consuming.

As EBL resist, SU-8 is a negative tone resist which is typically exposed using a beam current of $I = 0.2$ nA and a 60 μm beam shaping aperture. The critical dose of SU-8 is very low due to the chemical amplification process during cross-linking, typically only a few $\mu C/cm^2$, which is two orders of magnitude lower than that of PMMA. The low doses needed to expose the SU-8 enables low writing times in the EBL system and reduces cost for electron beam writing.

In recent years, the use of SU-8 as an EBL resist has been investigated by several authors [86–91]. Using $\mathcal{U} = 100$ kV EBL, 24 nm wide lines with a 300 nm period have been demonstrated on a 99 nm thick SU-8 film on a Si substrate using an exposure dose of 20 $\mu C/cm^2$ [90, 91]. For comparison, 10 nm wide lines with a period of 60 nm have been demonstrated on a 31 nm thick film of TEBN-1 resist on a Si substrate with an exposure dose of 4.1 mC/cm^2 [91]. The higher resolution of TEBN-1 comes at the price of a 205 times higher dose which dramatically increases the electron beam writing time compared to SU-8. Further, also the purchasing costs of TEBN-1 are orders of magnitude larger than that of SU-8.

4.2 Combined electron beam and UV lithography in SU-8

Many microdevices and systems require fabrication of microstructures over large areas in combination with smaller nanostructured regions. One example could be photonic crystal devices [92, 93] where the central photonic crystal structure requires nanometer scale definition while planar waveguides of μm to mm dimensions are necessary to facilitate coupling of light in and out of the components. Large area features of μm to mm scale dimensions are most efficiently defined by high-throughput parallel methods such as UV lithography (UVL) whereas dedicated serial nanofabrication methods such

as EBL are required for the sub-micrometer scale features.

This section presents combined electron beam and UV lithography (CEUL) in SU-8 as a fast and flexible lithographic technique for prototyping of functional polymer devices and pattern transfer applications. CEUL takes advantage of the property that SU-8 can be patterned by both EBL and UVL. Thus, CEUL is a lithographic technique suitable for defining both micrometer and nanometer scale features in a single polymer film on the wafer scale. The height of the micrometer and nanometer scale features can, in general, be matched within 30 nm.

Experimental scheme

The general scheme of CEUL is shown in Fig. 4.3 and is as follows: A thin film of negative-tone SU-8 2000 resist [94] is spin-coated on a 10 cm substrate of silicon with a layer of thermal oxide and alignment marks defined by reactive ion etch (RIE) or metal lift-off. The resist is pre-exposure baked at 90°C for 1 min. $\mathcal{U} = 100$ kV electron beam exposure of the nanometer scale features is performed; the exposure time is short due to the high electron sensitivity of SU-8. The micrometer scale features are defined by UV exposure of the same polymer film, followed by post-exposure bake (90°C, 1 min.), development in PGMEA, and iso-propyl alcohol (IPA) rinse. Subsequent to the lithography steps, the wafer is subjected to a soft O_2 plasma treatment in order to remove any SU-8 residuals in unexposed areas, adapted from Ref. [90]. After

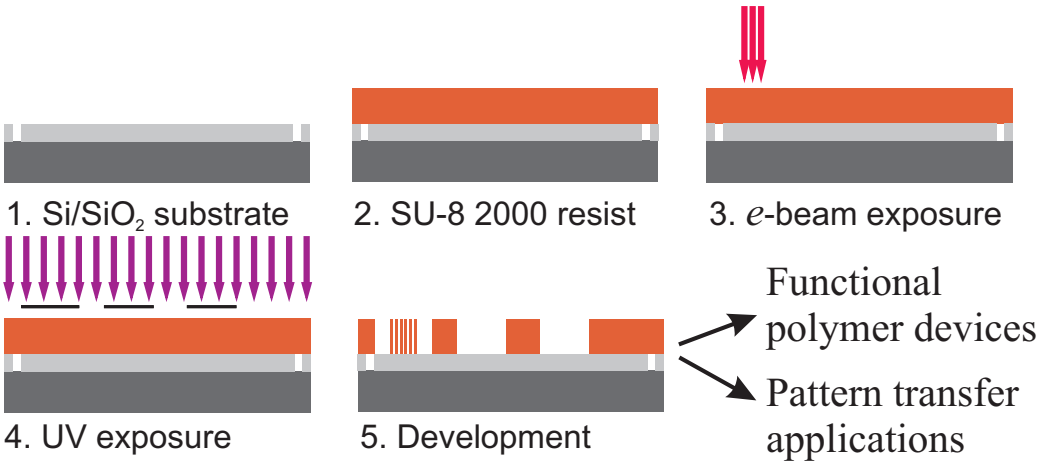

Fig. 4.3: Experimental scheme of CEUL in SU-8. The high electron sensitivity of SU-8 renders CEUL a fast and flexible lithography technique for defining both micrometer scale and nanometer scale features on the wafer scale.

CEUL, the fabricated structures can be used for functional polymer devices (see Chapter 5) and pattern transfer applications.

Electron beam dose

The optimum electron beam dose for the nanometer scale features depends on the pattern shape and spacing due to the proximity effect. To find the optimum electron beam dose for a given pattern design, a number of nanostructures are fabricated with different electron beam doses and inspected using scanning electron microscopy.

Figures 4.4 and 4.5 show structures fabricated by EBL in order to determine the optimum exposure dose. Layers of SiO_2 of different thicknesses are thermally grown on the Si substrates prior to SU-8 spin-coating. For too low doses, the structures are not well defined, whereas too high doses result in overexposed structures which are not fully developed and are connected by a 'sponge-like' network due to the proximity effect.

Figure 4.4 shows arrays of lines of design width $\ell = 280$ nm and period $\Lambda = 590$ nm which have been fabricated by EBL in a SU-8 film with an initial thickness of 449 nm on a Si substrate with a 2.5 µm thick thermally grown layer of SiO_2 (not subjected to O_2 plasma treatment). Electron beam doses from 2 µC/cm^2 to 9 µC/cm^2 have been investigated for these structures in steps of 1 µC/cm^2. For exposure doses less than 3 µC/cm^2, the structures are not well defined, whereas exposure doses above 3 µC/cm^2 result in overexposed structures.

Figure 4.5 shows a 2D array of lines of design width $\ell = 100$ nm and period $\Lambda = 380$ nm for different EBL doses on a Si substrate with a 310 nm thick layer of thermally grown SiO_2 (initial SU-8 film thickness 300 nm).

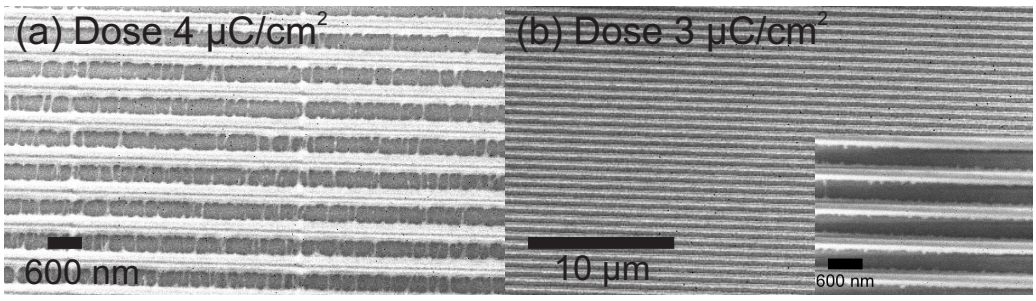

Fig. 4.4: Array of lines of design width $\ell = 280$ nm and period $\Lambda = 590$ nm defined by EBL. **(a)** Dose 4 µC/cm^2. Pronounced proximity effect. **(b)** Dose 3 µC/cm^2. Well defined array.

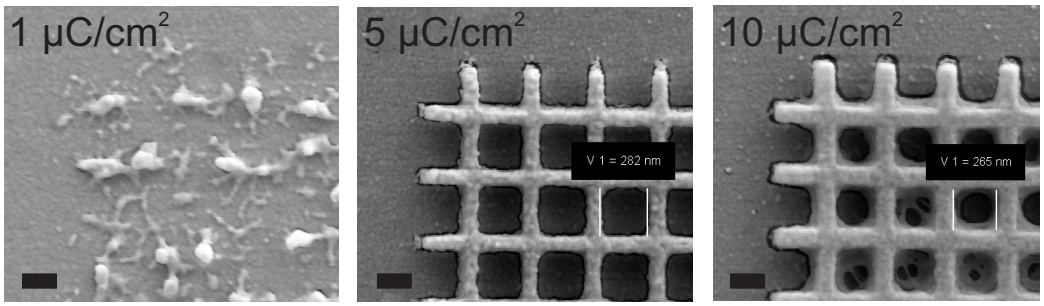

Fig. 4.5: 2D array of lines of design width $\ell = 100$ nm and period $\Lambda = 380$ nm for different doses defined by EBL. Optimum dose: 5 µC/cm^2. Scale bars: 200 nm. Samples covered with 20 nm Au for SEM contrast.

Doses in the range 1 µC/cm^2 – 20 µC/cm^2 have been investigated. The optimum exposure dose is determined to be 5 µC/cm^2. For 1 µC/cm^2, the structures are not well defined, and for 10 µC/cm^2, the 'sponge-like' network due to the proximity effect is clearly seen.

Figures 4.4 and 4.5 illustrate the narrow process window when performing EBL of closely spaced structures in SU-8 due to the strong influence of the proximity effect.

Matching the height

The height of the developed structures depends on the exposure dose; both for EBL and UVL. In CEUL, the heights of electron beam and UV exposed areas have to be matched in order to enable the use of the structures for e.g. nanofluidic devices or pattern transfer applications.

Figure 4.6(a) shows a dose curve for an array of lines, see Fig. 4.4, defined by EBL. The height of the developed structures is measured by a stylus profilometer and increases with the exposure dose. In order to achieve well defined structures for this pattern and initial film thickness (449 nm), we are working on the slope of the dose curve due to the influence of the proximity effect. The optimum electron beam dose is marked with a circle. The small inclination of the dose curve illustrates the low contrast of SU-8.

Fig. 4.6(b) shows a dose curve for micrometer scale features defined by UVL in a film of the same initial thickness. To match the height of the final structures, fabricated by CEUL, the UV exposure energy is chosen such that the developed height of the micrometer scale features matches the height of the optimized nanometer scale features (solid line of Fig. 4.6(b)).

Figure 4.7 shows an atomic force micrograph of the final structures fabri-

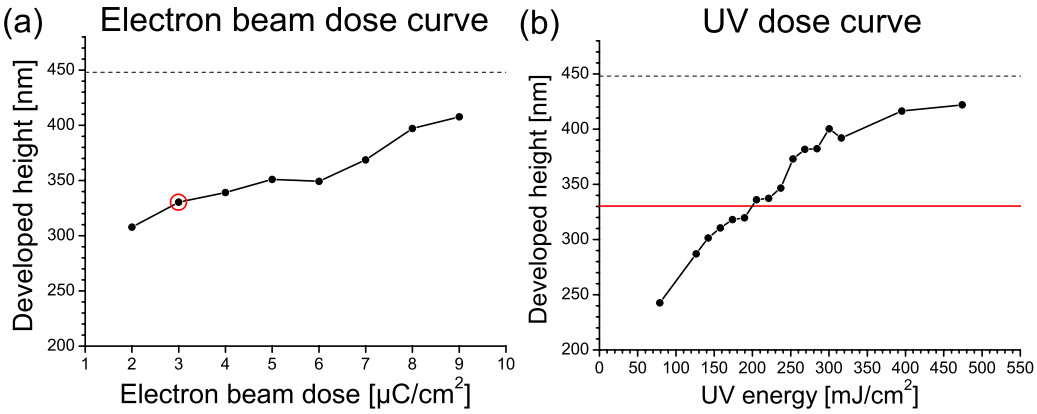

Fig. 4.6: **(a)** EBL dose curve. The circle indicates the optimum dose for the structures of Fig. 4.4. **(b)** UVL dose curve. The red solid line indicates the height of the optimized structures defined by EBL. The dashed line indicates the initial film thickness of 449 nm.

cated by CEUL (after O_2 plasma treatment). The image shows the boundary region between electron beam and UV exposed areas. The transition between the areas is very smooth, the height of the structures is 300 nm and the height of the electron beam and UV exposed areas is matched within 30 nm. The inclined flank in the UV exposed area is also observed for structures which have not been subjected to electron beam exposure and can thus be attributed to the UV exposure.

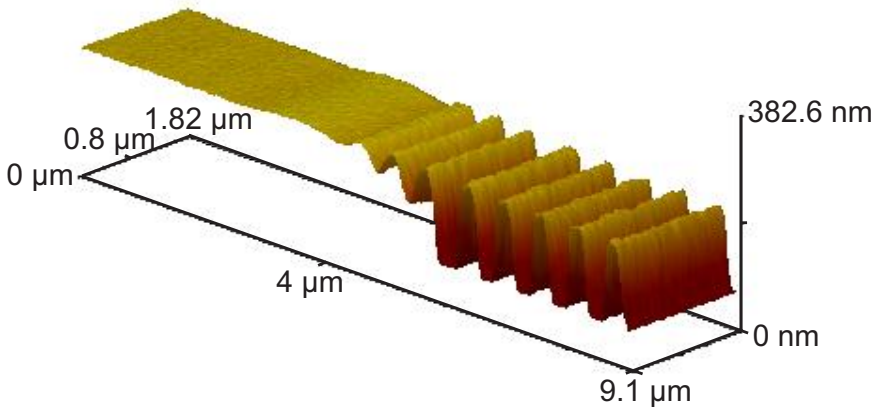

Fig. 4.7: Atomic force micrograph of structures defined by CEUL. The image shows the boundary region between electron beam and UV exposed areas, the height is matched within 30 nm.

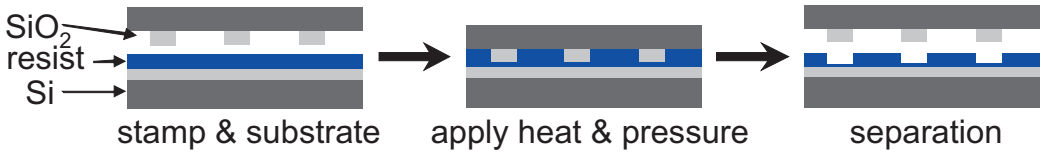

Fig. 4.8: The NIL process. Stamp and substrate is assembled and the structures from the stamp are transferred to the resist by applying heat and pressure.

4.3 Nanoimprint lithography

As a pattern transfer application of CEUL, stamp fabrication and thermal nanoimprint lithography (NIL) is presented. In NIL, a thermoplastic resist is structured through mechanical deformation by assembling the stamp and substrate and applying heat and pressure. A schematic of the NIL process is seen in Fig. 4.8. Since all structures on the stamp are imprinted simultaneously, NIL is a parallel technique which can potentially enable cheap nanofabrication since the stamps can be reused. The resolution of NIL is limited by the resolution on the stamp, i.e. the stamp fabrication. See Guo [95] for a review on NIL and related parallel imprint techniques.

On the stamps, a 2D array of lines of design width $\ell = 100$ nm and period $\Lambda = 380$ nm is defined in connection with micrometer scale features (UVL mask) by CEUL, see Fig. 4.9. The fabrication of the stamps was carried out by L. H. Thamdrup and A. Mironov who also performed the imprints.

The structures are defined by CEUL in SU-8 on a Si substrate with a 310 nm thick layer of thermally grown SiO_2. The spin-coated SU-8 film thickness is 300 nm and the optimum electron beam dose for the 2D array of lines is 5 $\mu C/cm^2$, see Figures 4.5 and 4.9(a).

After CEUL, the SU-8 structures are transferred into the SiO_2 layer by an anisotropic RIE process, using the SU-8 as etch mask and the Si substrate surface as etch stop layer, see Fig. 4.9(b),(c). The RIE process (STS C010

Gas	CF_4/CHF_3
Gas flow rate	16/24 sccm
RF Power	60 W
Pressure	100 mTorr
DC bias voltage	300 V
Time	10 min

Tab. 4.1: Reactive ion etch process used to transfer the pattern of SU-8 into SiO_2. Etch rate SiO_2: ∼33 nm/min. Selectivity: ∼1.6.

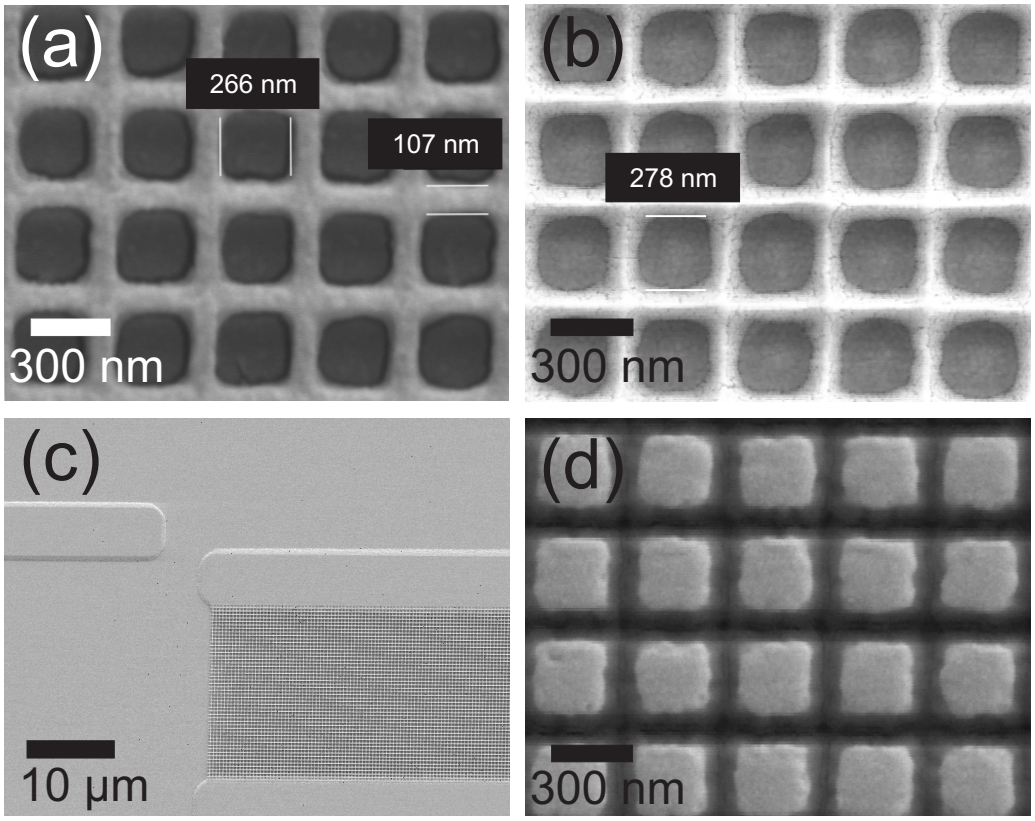

Fig. 4.9: Stamp fabrication by CEUL and pattern transfer, and replication of the structures by NIL. The samples have been covered with 20 nm Au for SEM contrast. **(a)** SU-8 structures of design width $\ell = 100$ nm and period $\Lambda = 380$ nm. Dose 5 µC/cm^2. **(b)** Nanometer scale features after pattern transfer into SiO_2. **(c)** Overview of stamp after pattern transfer. **(d)** Replicated structures by NIL in 310 nm thick mr-I T85 resist.

Multiplex Cluster System), see Table 4.1, has a SiO_2 etch rate of approximately 33 nm/min and a selectivity of SiO_2 to SU-8 of approximately 1.6. The sidewalls have a finite slope due to resist edge corrosion during RIE, see Fig. 4.9(b), which may be reduced by further optimization of the RIE process.

The electron beam and UV defined structures are aligned laterally within 2 µm, limited by the optical alignment of the UV exposed structures, and their heights are matched within 30 nm. Figure 4.10 shows a stylus profilometer scan across a device on the stamp, showing the variation of the top height of the structures along a vertical line in Fig. 4.9(c). Only the

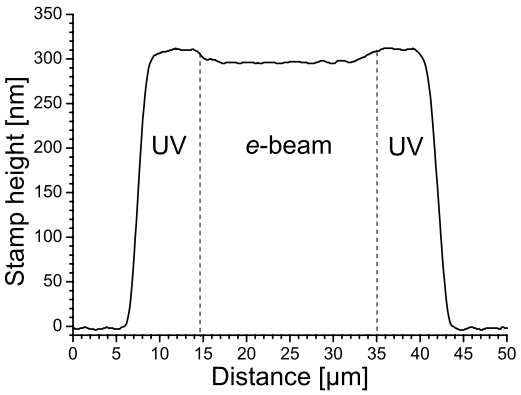

Fig. 4.10: Stylus profilometer scan of the fabricated stamp of SiO_2 along a vertical line of Fig. 4.9(c). The top height of the nanometer and micrometer scale features is, in general, matched within 30 nm (in this case 17 nm).

top height and not the individual features of the nanometer scale structures is resolved. For this device, the height of the structures is matched within 17 nm.

After stripping the remaining SU-8 in an O_2 plasma adapted from Ref. [90] and vapor deposition of an anti-sticking layer similar to that used in Ref. [96], the structures of the stamp are replicated in a 310 nm thick film of mr-I T85 NIL resist [97] on a SiO_2 substrate, see Fig. 4.9(d). For the imprint, a temperature of 200°C and an imprint pressure of 1.3 MPa for 60 min. was used for this first demonstration.

4.4 Summary

In this Chapter, the nanofabrication methods used in this thesis work are presented.

EBL is introduced as a high-resolution and flexible yet serial and expensive nanofabrication technique. Basic properties such as dose and proximity effect are discussed and SU-8 is presented as a highly sensitive negative tone EBL resist.

CEUL is presented as a fast and flexible nanofabrication technique suitable for wafer scale fabrication of both micrometer and nanometer scale features, taking advantage of the high sensitivity of SU-8 to both electron and UV radiation. Upon electron beam exposure of the nanometer scale features, micrometer scale features are added by UV exposure of the same polymer film, followed by simultaneous development. The height of the microme-

ter scale features is matched to the height of the optimized nanostructures within 30 nm by adjusting the UV exposure dose. CEUL in SU-8 is ideal for prototyping of functional polymer devices and pattern transfer applications.

NIL is introduced as a nanofabrication technique based on mechanical deformation of a thermoplastic resist. Stamps for NIL are fabricated to demonstrate a pattern transfer application of CEUL. On the stamps, a 2D array of 100 nm wide lines with a period of 380 nm are defined in connection with micrometer scale features by CEUL in SU-8 and pattern transfer into SiO_2 by RIE. The structures on the stamp are replicated by NIL in mr-I T85 resist.

5. TUNABLE OPTOFLUIDIC DFB DYE LASERS

This Chapter presents the design and operation of narrow linewidth, low threshold, and widely tunable optofluidic DFB dye lasers. The devices rely on light-confinement in a nanostructured polymer film embedded between two substrates. An array of nanofluidic channels forms a Bragg grating DFB laser resonator with a central $\pi/2$ phase shift relying on the third order Bragg reflection. The lasers are fabricated by CEUL in a thin film of SU-8 resist and polymer-mediated wafer bonding. The third order Bragg grating of the DFB laser resonator yields:

(i) Low out-of-plane scattering losses

(ii) Low coupling losses for the light when traversing the dye-filled nanofluidic channels due to the sub-wavelength dimensions of the resonator segments

(iii) A large free spectral range (FSR).

Points (i)+(ii) enable a low threshold for lasing, point (iii) facilitates wavelength tuning over the full gain spectrum of the chosen laser dye without mode-hopping. Optofluidic tuning is demonstrated by combining different grating periods and dye solution refractive indices.

Capillary action drives the liquid dye infiltration of the optofluidic DFB lasers and accounts for dye replenishment, thereby completely removing the need for external fluidic handling apparatus.

I have been the driving force behind the work described in this Chapter, the main results have been published in *Applied Physics Letters*, volume **89**, 103518 (2006) [50] and *Optics Express*, volume **15**, pages 137–142 (2007) [51].

5.1 Device design

The laser resonator structure, see Fig. 5.1, is based on a planar polymer waveguide structure supporting a single propagating TE-TM mode. The basic waveguide structure consists of a SiO_2 buffer substrate ($n = 1.46$), a 300 nm thick core of SU-8 polymer ($n = 1.59$), and a top cladding of PMMA ($n = 1.49$). An array of nanofluidic channels, defined lithographically in the SU-8 film, constitutes a third order Bragg grating DFB laser resonator. The resonator has a phase shift of $\pi/2$ in the middle, see Fig. 5.1(b), to obtain a single resonance at the Bragg wavelength for each Bragg reflection, cf. Chapter 2.3. The laser emits light laterally in the chip plane. The light is coupled directly into the SU-8 layer which guides the light to the edge of the chip for measurement.

In order to achieve a low threshold for lasing, the optical losses should be minimized. Two main challenges to be addressed in this context are liquid-core waveguiding and out-of-plane scattering from high order Bragg reflections. Since the liquids used have a refractive index lower than that of the cladding layer, see Fig. 5.1(c), a well-confined TE-TM-like mode does not exist in the fluidic resonator segments and light is not guided. However, the requirement of a low refractive index polymer and a high refractive index liquid may be relaxed by reducing the dimensions of the resonator segments as the subwavelength regime is entered [39].

Despite the lack of waveguiding in the dye-filled nanofluidic channels, the sub-wavelength dimensions of the third order DFB grating yield a low coupling loss for the light when traversing the dye-filled nanofluidic channels. Combined with the low out-of-plane scattering losses and large FSR of the third order Bragg grating, see Chapter 2.2, this has resulted in an efficient laser device.

The laser resonator is embedded in a 300 nm high, 500 μm wide fluidic channel which is followed by a 100 μm wide, 16 cm long meandering channel. The hydrophilicity of the SiO_2 [98] at the bottom of the nanochannels facilitates filling of the nanochannels of the resonator with a dye solution by capillary action, thus simplifying operation of the device as opposed to conventional setups with external syringe pumps. Replenishing of the dye in the cavity region is achieved for hours through capillary filling of the meandering channel.

In order to estimate the spectral positions of the resonances and the FSR of the passive DFB laser resonator, we consider the periodic arrangement of polymer and fluidic resonator segments in the layered structure shown in Fig. 5.1(c). The lack of waveguiding in the fluidic segments gives rise to losses and complicates the modelling of light propagation in the structure. In

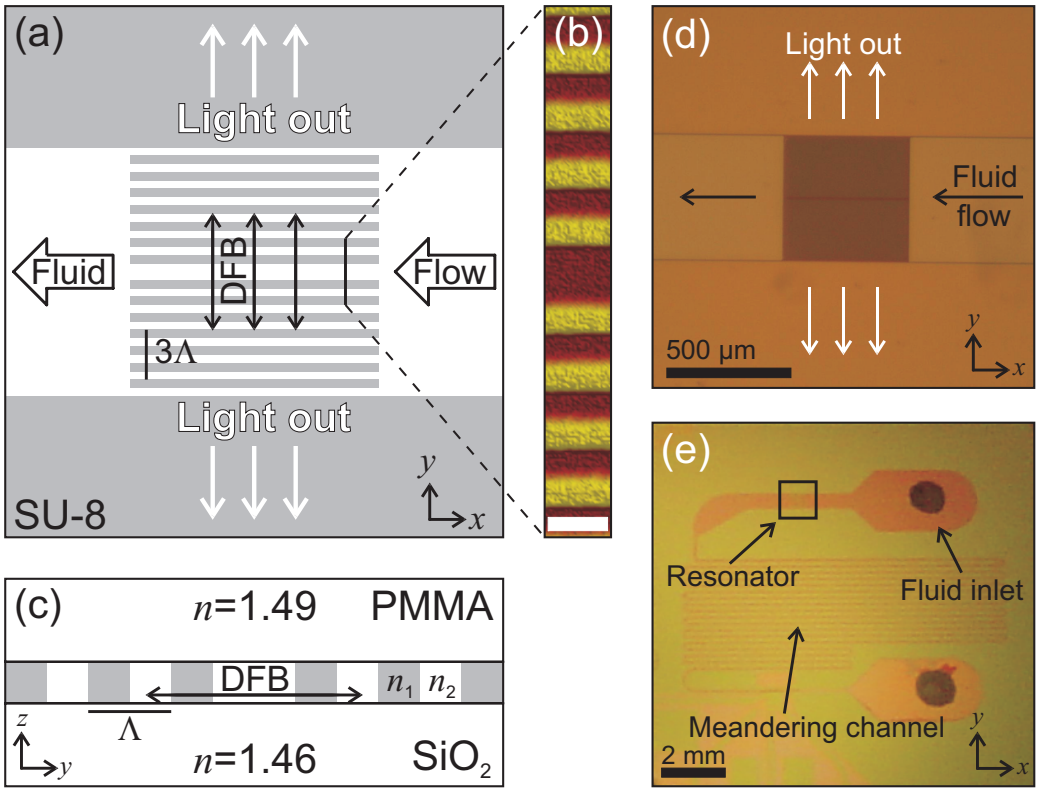

Fig. 5.1: Overview of the capillary driven tunable optofluidic third order DFB dye laser. **(a)** Top-view schematic. **(b)** Atomic force micrograph of the central region of the third order DFB laser resonator including the central $\pi/2$ phase shift. The white scale bar is 600 nm. **(c)** Side-view schematic showing the refractive index distribution of the structure. **(d)** Optical micrograph of the 500×500 µm^2 DFB laser resonator embedded in the shallow meandering channel. **(e)** Top-view picture of the over-all layout of the fabricated laser chip.

general, a full solution to Maxwell's equations in the geometry is required [39].

The resonances of the grating satisfy the Bragg condition

$$m\lambda_m = 2\Lambda_{\text{op}} \tag{5.1}$$

where $m = 1, 2, 3, \ldots$ is the reflection order, λ_m is the free space wavelength of the m'th reflection order, and Λ_{op} is the optical path length of one grating period, see Chapter 2.2. The spatial dimensions of the resonator segments are carefully chosen so that the DFB laser oscillates at the third order Bragg reflection wavelength using the model developed in Chapter 2.3. From the experimental data, summarized in Table 5.3, Λ_{op} can be estimated. Given

Λ_{op}, the FSR is calculated as

$$FSR = \frac{\lambda_m}{m-1} \tag{5.2}$$

as derived in Chapter 2.2.

As an example, a grating of period $\Lambda = 599$ nm filled with an ethylene glycol solution ($n = 1.43$) is considered. From Eq. (5.1) using $m = 3$ and $\lambda_3 = 580.60$ nm, we obtain $\Lambda_{op} = 871$ nm and a FSR of 290 nm at the third order Bragg reflection wavelength. This very large FSR ensures that only the third order resonance falls inside the wide dye gain spectrum and facilitates tuning of the laser over the full gain spectrum of the chosen laser dye (for visible wavelengths).

The laser structure provides tuning of the wavelength by changing the grating period and through optofluidic functionality by changing the refractive index of the dye solution.

5.2 Fabrication

The devices are fabricated by CEUL to enable fast and flexible prototyping of device designs, see Chapter 4.2, followed by polymer-mediated wafer bonding. The key fabrication parameters are stated here.

A 430 nm thick film of SU-8 2000 resist [94] is spin-coated onto a Si substrate with a 2.5 µm thick thermally grown oxide layer. The wafer is baked at 90°C for 1 min. The device structure is defined by CEUL in the SU-8 film. The nano-structures of the third order DFB grating are defined by $\mathcal{U} = 100$ kV electron beam exposure (JEOL-JBX9300FS, dose 3 µC/cm^2). The total writing time for all 32 devices on a 10 cm wafer is 15 min.

After electron beam exposure, the micron-sized structures (meandering channel and reservoirs) are defined in the same polymer film by UV exposure, the wafer is post-exposure baked at 90°C for 1 min., and the micro and nano-structures are developed simultaneously in PGMEA for 30 s, followed by an IPA rinse. The wafer is subsequently subjected to a 20 s soft oxygen plasma to remove any residues of SU-8 at the SiO_2 surface in the nano-channels of the DFB resonator. After the plasma treatment, the structures are 300 nm high, and the heights of the EBL and UVL defined structures are matched within 30 nm.

Fluidic access holes are formed by micro powder blasting [99] and the channels are sealed by a glass lid, using adhesive bonding by means of a 5 µm thick PMMA film (2200 N, 140°C, 10 min.) [80].

5.3 Capillary action

The ability of a fluid to wet a surface is characterized by the contact angle θ. The contact angle is measured by putting a small droplet of fluid, typically water, on a horizontal surface and measuring the angle between the surface and the droplet where the fluid/air interface meets the surface, see Fig. 5.2. The contact angle is specific for the fluid/surface system and is determined by the interactions across the fluid, solid, and air interfaces.

For $\theta < 90°$, the surface is called hydrophilic and is easily wetted by water, whereas for $\theta > 90°$, the surface is hydrophobic and water droplets almost do not spread out on the surface. Water contact angles for typical lab-on-a-chip materials are listed in Tab. 5.1.

Of the materials used to fabricate the fluidic network of the optofluidic dye lasers, SU-8 and PMMA both have contact angles close to 90° and can be considered hydrophobic. SiO_2 is highly hydrophilic and facilitates the filling of the fluidic network by capillary action. Note, the high water contact angles of single crystal Si and PDMS dramatically limit the number of fluids available for use in capillary driven fluidic networks using these materials.

To operate the optofluidic dye lasers, the device is loaded by adding a droplet of dye solution to the fluid inlet, thus filling the DFB resonator structure by capillary action. The use of this simple fluidic handling scheme omits the need for external fluidic handling apparatus, such as syringe pumps. The devices are suitable for single-use, as they are not easily emptied and recycled once they have been filled.

Capillary action is driven by the capillary pressure which in micro and nanochannels can be up to several bars. By balancing the expressions for the hydraulic resistance and the capillary pressure for a horizontal channel

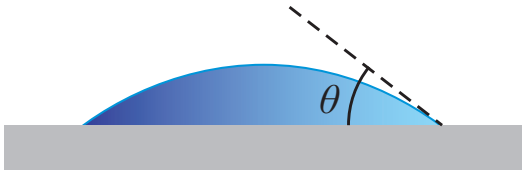

Fig. 5.2: Definition of the contact angle θ.

	Si	Glass	SiO_2	SU-8†	PMMA	PDMS
θ	110°	20° – 35°	∼ 30°	∼ 90°	60° – 75°	∼ 110°

Tab. 5.1: Water contact angles θ for different materials. Numbers from [98] († from [100]).

configuration (no contribution by gravity), the position of the advancing fluid front x in a straight channel can be determined as a function of time t as [101, 102]

$$x(t) = a\sqrt{t} \tag{5.3}$$

where a is a constant dependent on the surface tension of the fluid in air, the contact angle(s) of the fluid to the channel walls, the channel dimensions and geometry, and the viscosity of the fluid. See the textbook [103] for an overview.

By differentiation, the fluid velocity v can be obtained as

$$v = \frac{dx}{dt} = \frac{a}{2\sqrt{t}} \tag{5.4}$$

i.e. the speed of the advancing fluid front in the meandering channel decreases with time.

Figure 5.3 shows a microscope image of a laser device during filling. The horizontal structures seen along the grating appeared during bonding for this particular device and did not affect the optical properties of the laser. The fluid front advances towards the left, thereby filling the resonator with dye solution. Upon filling of the resonator, the fluid front continues into the 100 µm wide, 16 cm long meandering channel which facilitates dye replenishment during laser operation.

The speed of the fluid front is approximately $v \sim 11.7$ µm/s, corresponding to a flow rate of 350 µm^3/s, estimated from the fluid front positions 5 min. and 10 min. after loading of the device with ethylene glycol solution. When assuming a 50 % volume fraction of SU-8 in the 500×500 µm^2 resonator area, this corresponds to a replacement of the dye solution in the resonator in 107 s.

During the first 30 min. of experiments, the dye solution in the cavity region is replaced in 30 s − 5 min. using an ethylene glycol solution. The flow rate in the resonator region can be increased, e.g. by increasing the width of the meandering channel.

Due to the highly hydrophilic nature of SiO_2, the device can be loaded with a wide variety of fluids such as water, ethanol, ethylene glycol, and refractive index matching fluids (`www.cargille.com`), enabling a wide range of applications for micro and nanofluidic channels employing our fabrication scheme. For optofluidic dye lasers, an additional requirement is that the dye must be dissolvable in the solvent or solvent mixture used.

In the experiments, the fabricated optofluidic dye lasers were operated with four different R6G dye solutions, all with a concentration of 2×10^{-2} mol/L

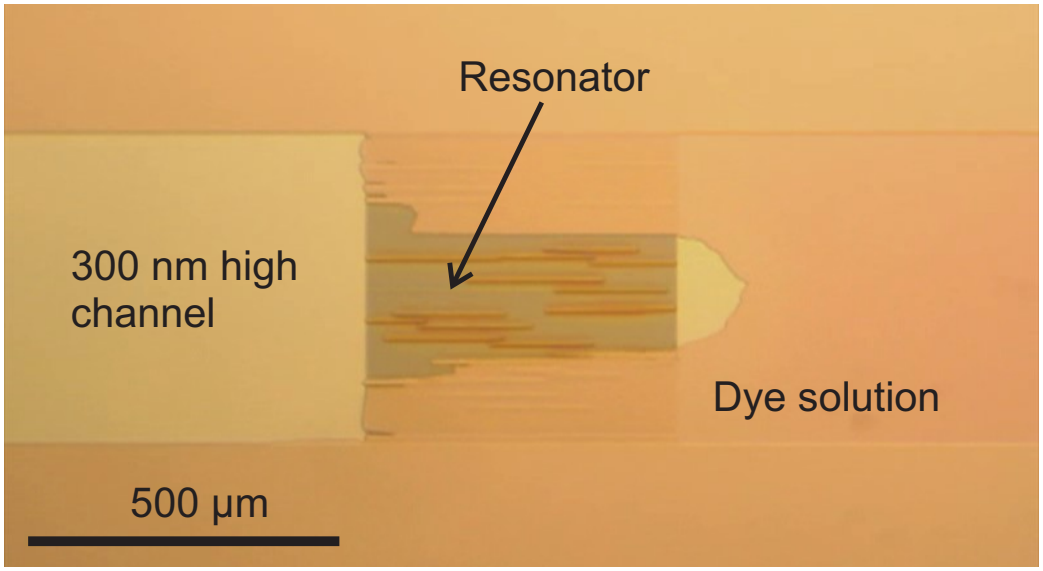

Fig. 5.3: Optical microscope image of a laser device during filling (ethylene glycol solution). The laser resonator is partially filled with dye solution and the fluid front advances towards the left.

and a refractive index below that of PMMA: ethanol ($n = 1.36$), ethylene glycol ($n = 1.43$), a 2:1 mixture of ethylene glycol and benzyl alcohol ($n = 1.467$), and a 1:1 mixture of ethylene glycol and benzyl alcohol ($n = 1.485$). The refractive indices of the mixtures are determined by linear extrapolation of the refractive indices of the pure solvents, a method that has been experimentally confirmed by Søren Balslev.

The laser is optically pumped at 532 nm perpendicularly to the chip plane through the glass lid by a frequency doubled Nd:YAG laser (5 ns pulse duration, 10 Hz repetition rate) and the output dye laser light is collected by an optical fiber at the edge of the chip and analyzed using a fixed grating spectrometer (resolution 0.15 nm).

Figure 5.4 shows the output laser power from an optofluidic dye laser device filled with ethylene glycol solution as a function of the time after loading of the chip. For this particular device, the resonator region is optically pumped through a 100 µm wide slit in order not to bleach the dye molecules in the other parts of the fluidic network.

The laser output rapidly decreases during the optical pumping which is only performed in certain intervals. Between the periods of optical pumping, the dye solution in the resonator is exchanged and when the optical pumping commences, the laser output is back to the initial level. During the 33 min.

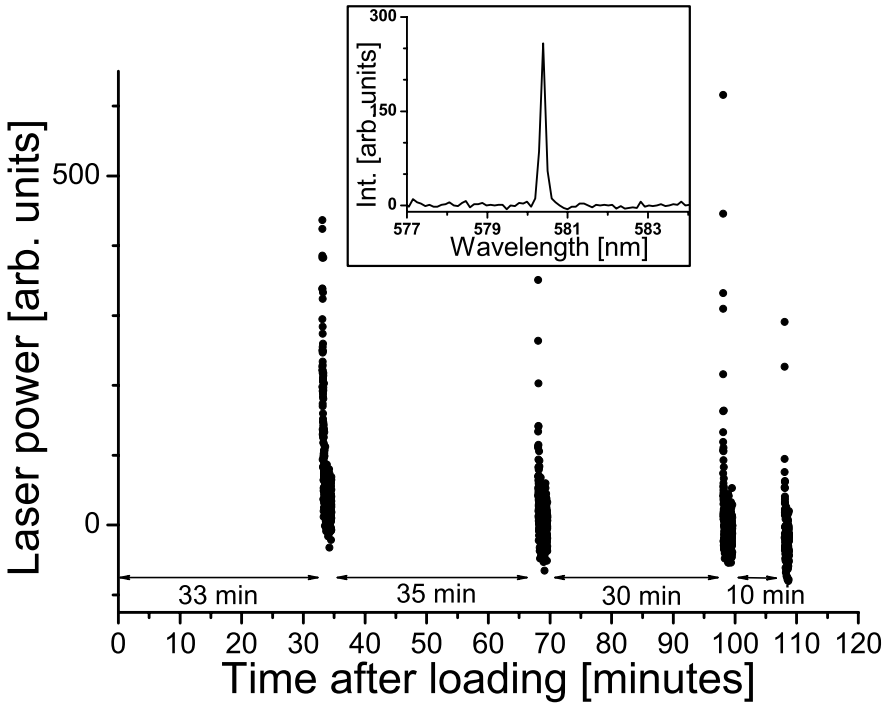

Fig. 5.4: Laser output power as a function of time after loading of the device with ethylene glycol solution. The dye solution in the cavity is replenished by the capillary driven flow. The inset shows a typical emission spectrum from the dye laser device.

long pause before the start of the experiment, the slit was aligned to the resonator structure, the detection fiber was aligned to the chip, and a suitable optical pumping level of $2-3$ times the laser threshold was determined. The inset shows a typical narrow linewidth spectrum from the laser device. The spectral characteristics did not change during the experiment. The results demonstrate that the dye solution in the resonator is replenished by the capillary driven flow.

5.4 Wafer-scale reproducibility

In order to investigate the wafer-scale reproducibility of the devices, chips of identical design dimensions have been filled with the same dye solution. Fig. 5.5 shows laser spectra from four nominally identical chips (grating period $\Lambda = 601$ nm) filled with R6G in ethylene glycol. The results demonstrate wafer-scale spectral reproducibility of the laser, exhibiting narrow linewidth

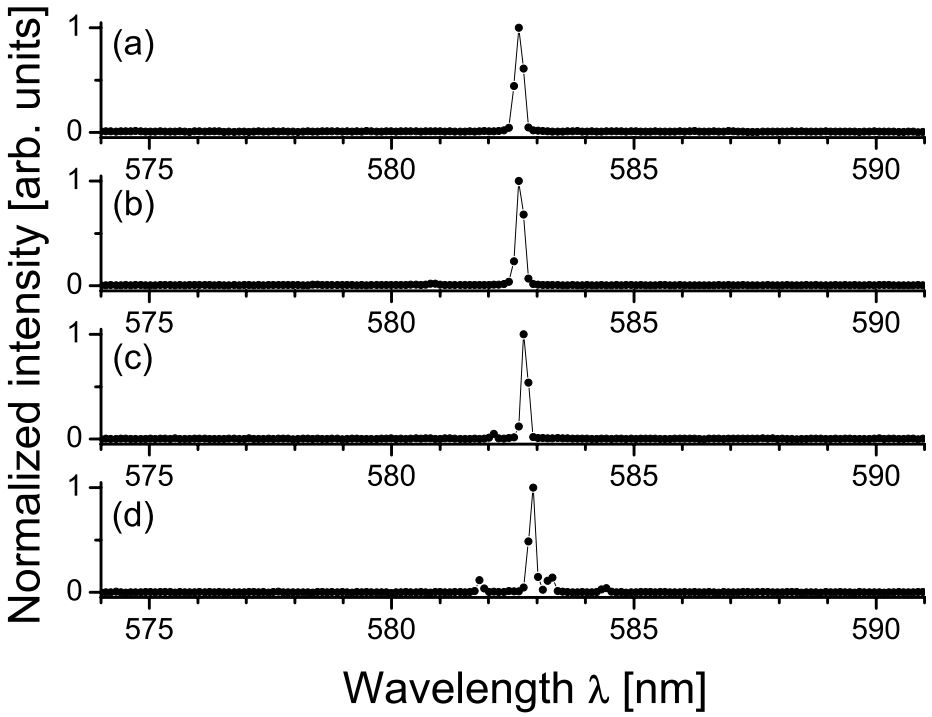

Fig. 5.5: Normalized laser spectra from four nominally identical chips (Λ = 601 nm) demonstrating wafer-scale spectral reproducibility of the laser. On each chip, the DFB laser resonator is filled by capillary action with R6G dissolved in ethylene glycol. The average laser wavelength of the chips is 582.72 nm with a standard deviation of 0.14 nm.

emission, polarized perpendicularly to the chip plane (TM). The average laser wavelength is 582.72 nm with a standard deviation of 0.14 nm, at the resolution limit of our spectrometer (0.15 nm).

The deviation and the minor peaks in Fig. 5.5(c),(d) may arise from grating imperfections due to fabrication defects. Due to limited spectrometer resolution, our equipment does not allow us to determine whether the laser is truly operating in a single mode, and the spectral shape and linewidth of the laser remain undetermined. Although the devices are not emptied after use, the excellent wafer-scale spectral reproducibility allows for a quantitative comparison between devices of different design dimensions filled with different dye solutions.

Figure 5.6 shows the output laser power as a function of the average pump pulse fluence for a device. The laser spectrum of the device is shown in Fig. 5.9(e). The output power is found by integrating the measured laser

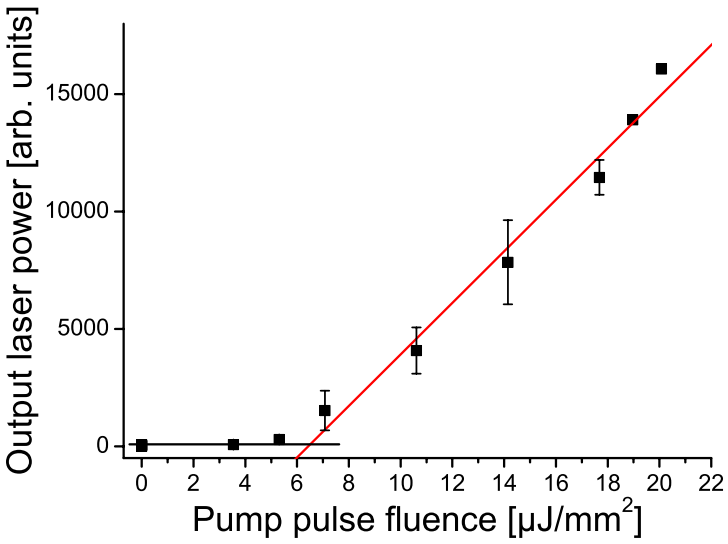

Fig. 5.6: Typical pump pulse fluence/output laser power graph for the laser device with spectrum shown in Fig. 5.9(e). The graph follows the standard pump/output relation of two linear segments around a laser threshold of ~ 7 μJ/mm^2.

spectrum for each value of the average pump pulse fluence. The graph follows the standard pump/output relation of two linear segments around a threshold fluence Q_{th} of approximately $Q_{\text{th}} = 7$ μJ/mm^2 and is typical for the fabricated lasers.

The error bars of the output laser power are calculated as the standard deviation of a number of output laser power measurements using the same average pump pulse energy fluence and reflect the pump pulse energy fluctuations from our Nd:YAG system.

5.5 Optofluidic tuning

This section presents results on optofluidic tunability, achieved by employing two tuning concepts:

(i) Refractive index tuning by altering the dye solution refractive index

(ii) Tuning by changing the grating period.

By combining the two concepts, an optofluidic tunability of 45 nm is achieved. Further, the laser threshold fluence decreases with increasing dye solution refractive index.

Refractive index tuning and threshold analysis

Fig. 5.7 shows laser spectra from chips of grating period $\Lambda = 601$ nm with R6G dissolved in different solvents, thus demonstrating 6.45 nm optofluidic tuning of the laser from 581.41 nm to 587.86 nm. In Fig. 5.7(c), the minor side-mode shifted 1.8 nm from the main peak may be attributed to an additional phase shift introduced in the DFB grating by a stitching error during electron beam exposure. For increasing fluid refractive indices, the emission wavelengths increase and the laser thresholds decrease, see Table 5.2.

In order to account for this decrease in laser threshold with increasing fluid refractive index, the loss of light due to the lack of waveguiding in the fluidic resonator segments is investigated. To simplify the computational problem, the coupling loss γ for light traversing one dye-filled nanofluidic channel is calculated. γ can be calculated using a finite difference beam propagation method (FD-BPM).

Beam propagation methods (BPMs) are powerful tools for understanding

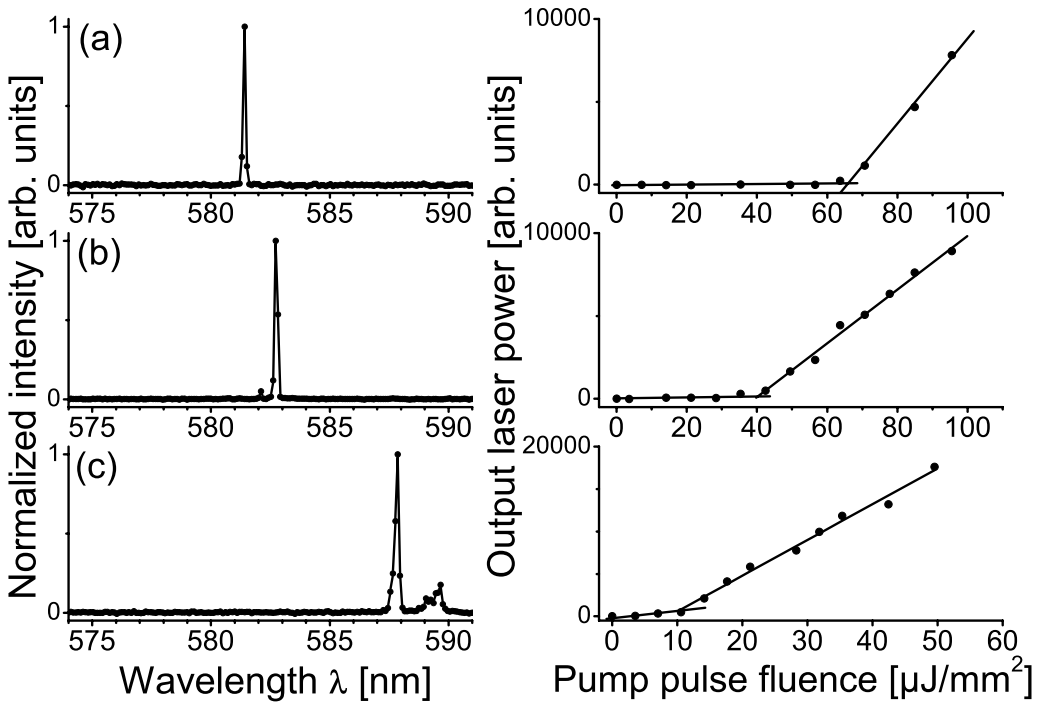

Fig. 5.7: Normalized laser spectra and corresponding laser output power curves as a function of pump pulse fluence for R6G in three different solutions ($\Lambda = 601$ nm): **(a)** R6G in ethanol. **(b)** R6G in ethylene glycol. **(c)** R6G in a 1:1 mixture of ethylene glycol and benzyl alcohol.

Solvent	n	λ [nm]	Q_{th} [$\frac{\mu J}{mm^2}$]	γ
ethanol	1.36	581.41	65	.159
ethylene glycol	1.43	582.72	40	.089
ethylene glycol/ benzyl alcohol 1:1	1.485	587.86	10	.043

Tab. 5.2: Summary of threshold analysis. For R6G solutions of larger refractive indices n, the laser wavelength λ increases, and the threshold pump fluence Q_{th} and coupling loss γ decrease. Fixed grating period $\Lambda = 601$ nm.

the propagation of light through structures with an arbitrary refractive index distribution. BPM typically require less computational power than FEM and can handle larger structures (relative to the wavelength). The propagation is done by following the phase front along a fixed axis. The FD-BPM implementation used in this work allows for propagation of light through a 2D structure, see Fig. 5.8, as 3D structures are computationally demanding. The implementation was programmed by Søren Balslev in Mathematica and is described in detail in [55].

FD-BPM propagates light in a structure with average refractive index n_0 by means of the paraxial Helmholtz equation in the slowly varying envelope approximation. The 'paraxial' refers to the propagation direction (the direction of the $\mathbf{k}$ vector) which is mainly along the positive y-axis, i.e. from left to right in Fig. 5.8(a). An $\exp(i\omega t)$ time dependence is assumed. In the TM-case, the paraxial Helmholtz equation becomes [104]

$$2ik_0n_0\frac{\partial\psi}{\partial y} = \left\{\frac{\partial^2}{\partial z^2} + k_0^2\left[n^2(y,z) - n_0^2\right]\right\}\psi - \frac{\partial \ln(n^2)}{\partial z}\frac{\partial\psi}{\partial z} \tag{5.5}$$

where $n(y,z)$ is the refractive index distribution, $H_x = \psi\exp(-ik_0n_0y)$ is the magnetic field component in the x-direction, and ψ is slowly varying in the y-direction, i.e. $\frac{\partial^2\psi}{\partial y^2} \simeq 0$. For regions with refractive index n_0, the phase does not evolve with distance during calculation.

By calculating $\frac{\partial^2\psi}{\partial z^2}$ from the second order difference coefficient and integrating Eq. (5.5) from y to $y + \Delta y$, a system of linear equations can be obtained to be solved for $\psi_{j+1}(y+\Delta y)$, where j is the step (slice) number [55]. In this fashion, ψ can be propagated through any given refractive index distribution by applying FD-BPM. Note, that FD-BPM does not account for back-reflections from the dielectric interfaces as the light propagates through the structure.

The upper and lower boundaries in Fig. 5.8 are made absorbing by adding an imaginary part to the refractive index near the boundary in order to avoid reflections. The coupling loss for light traversing a dye-filled nanofluidic

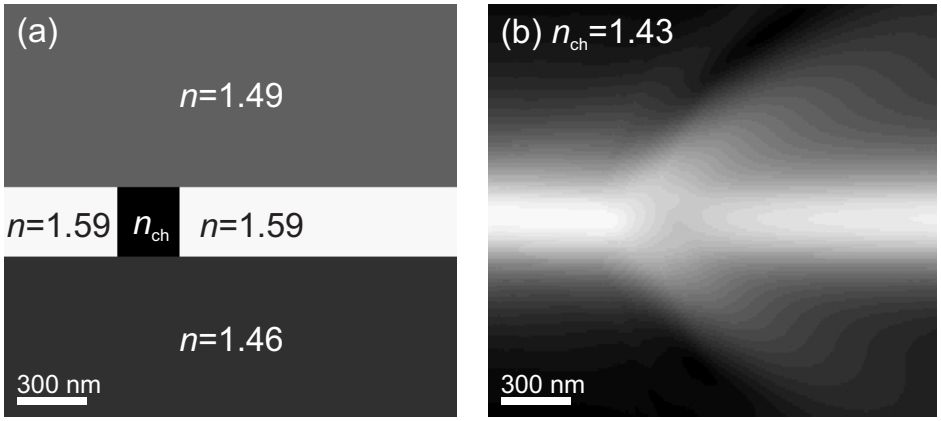

Fig. 5.8: FD-BPM simulations of the coupling loss γ for a period of the DFB grating. **(a)** Sketch of the refractive index distribution. The width of the channel is 273 nm. **(b)** Energy distribution for $n_{\mathrm{ch}} = 1.43$ (ethylene glycol) is shown as an example.

channel is modeled by propagating the TM mode of the single mode waveguide structure of SU-8 core height $h_{\mathrm{core}} = 300$ nm through the structure of Fig. 5.8(a).

As light of the observed wavelength traverses a 273 nm wide nanofluidic channel filled with liquid of refractive index n_{ch}, corresponding to the value of the used solvent, part of the light is lost into the top and bottom cladding layers. The coupling loss γ is calculated from the maximum field energies in the waveguide core at the input ($y = 0$) and output ($y = L$) of the waveguide. Let $H_x(0, z)$ and $H_x(L, z)$ denote the magnetic fields at the input and output, respectively. γ is calculated as

$$\gamma = 1 - \frac{\max\left\{|H_x(L,z)|^2\right\}}{\max\left\{|H_x(0,z)|^2\right\}} \tag{5.6}$$

The calculations yield the energy propagation loss corresponding to the coupling loss for a period of the DFB grating. As an example, the energy distribution with the channel filled with ethylene glycol ($n_{\mathrm{ch}} = 1.43$) is shown in Fig. 5.8(b). The loss decreases for increasing n_{ch}, see Table 5.2. For increasing refractive index in the channel, the fluidic segment increasingly resembles a waveguide, thus yielding a lower coupling loss.

To obtain lasing in the resonator, the amplification of the R6G must equal the loss. As expected, the experiments show that the threshold fluence for lasing decreases as the refractive index of the R6G solution increases, see Table 5.2.

The wavelength dependence of the R6G gain, see Figs. 2.4 (page 24) and 3.4 (page 49), cannot account for this behavior. The gain maximum for R6G is situated at $\lambda \sim 565$ nm, and for longer wavelengths R6G is less efficient. If this effect was dominant, devices with a longer emission wavelength should have a higher threshold fluence, which is not the case.

According to the estimations of the penetration depth of the pump light in Tab. 3.1 (page 50), the penetration depth δ of the pump light for the chosen dye concentration is estimated to be a few µm. As the channel height in the optofluidic dye lasers is only 300 nm, i.e. less than 10 % of δ, most of the pump light is not absorbed by the dye molecules. Thus, by employing a more efficient optical pumping scheme, a considerably lower threshold fluence may be obtained.

Wavelength tunability

In order to investigate the tuning range of the laser without mode-hopping, devices with different grating periods $\Lambda = 579,\ 599,\ 620$ nm were fabricated by varying the width of the nanochannels and keeping the width of the SU-8 bars fixed. The periods were derived from atomic force micrographs of the SU-8 structures prior to bonding, cf. Fig. 5.1(b).

Figure 5.9 shows laser spectra for laser devices with different grating periods using different R6G solutions. The lasers exhibit narrow linewidth emission (except the laser of Fig. 5.9(b)) and are polarized perpendicular to the chip plane (TM). The minor side-modes in the spectrum in Fig. 5.9(b) may be due to grating defects due to fabrication errors. The spectral shape and linewidth of the lasers remain undetermined due to limited spectrometer resolution.

The data are summarized in Tab. 5.3 and demonstrate wavelength tunability of 45 nm by changing the grating period (coarse-tuning) and dye

Label	Λ [nm]	n	λ [nm]	$\Delta\lambda$ [nm]
(a)	579	1.43	561.52	7.69
(b)	579	1.485	569.21	
(c)	599	1.43	580.60	6.75
(d)	599	1.467	585.04	
(e)	599	1.485	587.35	
(f)	620	1.485	606.28	

Tab. 5.3: Summary of the data presented in Fig. 5.9. The laser wavelength λ is tuned by changing the grating period Λ and the refractive index n of the R6G solution. $\Delta\lambda$ denotes the refractive index tuning range for fixed Λ.

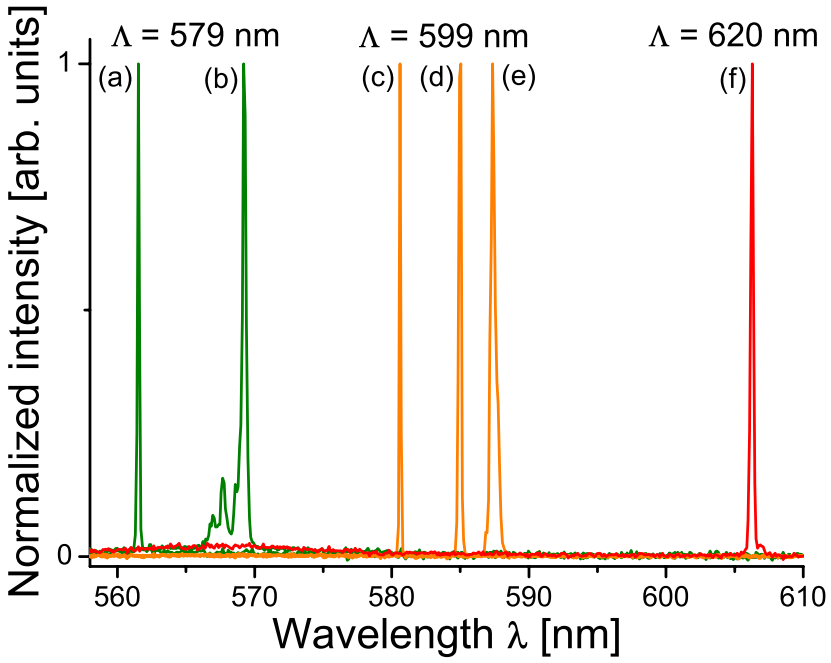

Fig. 5.9: Laser spectra from different laser devices showing a tunability of the lasers of 45 nm by changing the grating period and the refractive index of the R6G solution. Lasers with different periods Λ were fabricated.

solution refractive index (fine-tuning).

The achievable refractive index tuning range depends on the wavelength selection (Bragg) condition for the cavity as well as the confinement of the optical mode to the liquid. The results for $\Lambda = 579$ nm demonstrate a large refractive index tuning range of $\Delta\lambda = 7.69$ nm for $\Delta n = 0.055$, see Table 5.3, due to the low reflection order of the employed third order Bragg grating. Li and Psaltis [105] have reported a 2.2 nm refractive index tuning range using a fifth order Bragg grating for $\Delta n = 0.069$.

Figure 5.10 shows the laser wavelength plotted as a function of grating period for the devices using ethylene glycol and 1:1 ethylene glycol/benzyl alcohol solutions. For these solutions, three or more points exist, see Tabs. 5.2 and 5.3, and linear fits have been added to the graphs. In Figure 5.11, the laser wavelength is plotted as a function of dye solution refractive index for the devices with $\Lambda = 599$ nm, see Tab. 5.3. A linear fit is provided. The devices are tuned through optofluidic functionality by changing the dye solution refractive index.

Figures 5.10 and 5.11 provide linear tuning curves and indicate a linear dependence of the wavelength on grating period and dye solution refractive

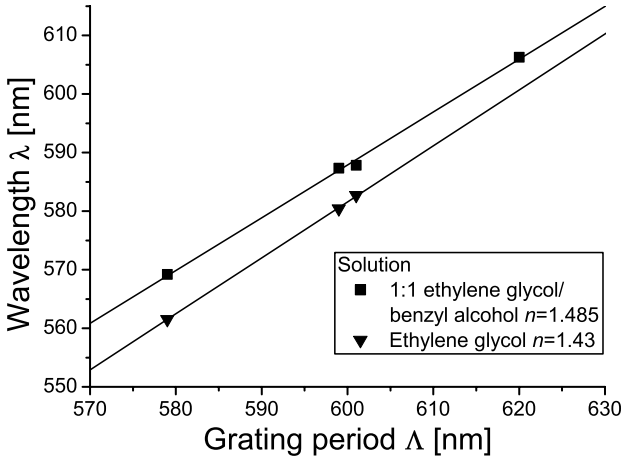

Fig. 5.10: Laser wavelength as a function of grating period for different R6G solutions. The fits indicate a linear dependence for each solution.

index. This may be interpreted as a linear regime where the Bragg condition of Eq. (5.1) applies although the resonator structure of Fig. 5.1 is not a simple layered dielectric stack but rather a 2D structure of sub-wavelength dimensions. To draw further conclusions from the graphs, more data points are needed.

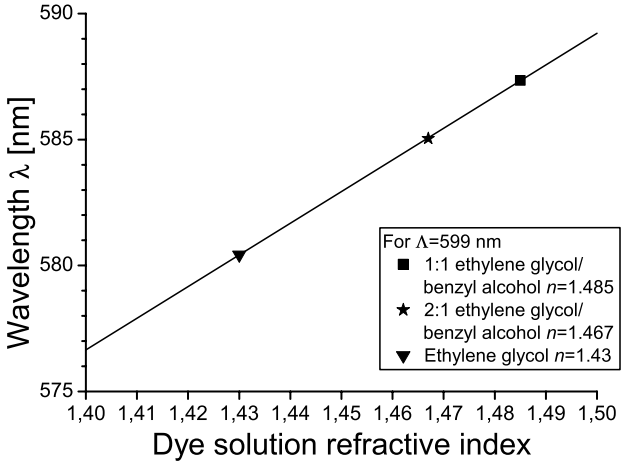

Fig. 5.11: Laser wavelength as a function of dye solution refractive index for different R6G solutions with fixed grating period $\Lambda = 599$ nm. The fit indicates a linear dependence.

5.6 Summary

This Chapter describes the fabricated tunable third order optofluidic DFB dye lasers. The lasers rely on light-confinement in a nanostructured polymer film and a third order Bragg grating DFB laser resonator with a central $\pi/2$ phase shift. In the devices, the dye replenishing flow to account for dye bleaching is achieved through capillary filling of a long meandering channel following the laser resonator. This significantly simplifies the operation of the devices as external fluid handling is omitted.

The lasers are fabricated by CEUL in SU-8 and polymer-mediated wafer bonding, ideal for fast and flexible prototyping of device designs. Due to the large FSR of the third order Bragg grating, the laser resonator provides a wide tuning range of 45 nm using a single laser dye by changing the grating period and dye solution refractive index. A refractive index tunability of 7.69 nm is obtained.

Despite the lack of waveguiding in the dye-filled nanofluidic resonator segments of the laser resonator, the lasers exhibit low threshold fluences down to $Q_{\mathrm{th}} \sim 7$ μJ/mm^2 due to the sub-wavelength dimensions of the resonator segments and low out-of-plane scattering.

To provide real-time wavelength tunability, the laser could be combined with a microfluidic mixer [6]. The laser is suitable for integration on lab-on-a-chip microsystems [14], e.g. for novel sensor concepts, where coherent, tunable light in the visible range is desired.

6. DIFFUSIVE DYE REPLENISHMENT IN OPTOFLUIDIC LIGHT SOURCES

This Chapter presents an investigation of the bleaching dynamics that occur in optofluidic dye lasers where the liquid-dissolved laser dye in a microfluidic channel is locally bleached due to optical pumping. The results show that for microfluidic devices, dye bleaching may be compensated through diffusion of dye molecules *alone*, suggesting a diffusive dye replenishment mechanism for optofluidic light sources.

By relying on diffusion rather than convection to generate the necessary dye replenishment, the observations potentially allow for a significant simplification of optofluidic dye laser device layouts, omitting the need for cumbersome and costly external fluidic handling or on-chip microfluidic pumping devices.

My role in this work has mainly been to experimentally verify the theoretical predictions. I have built the experimental measurement setup, performed the measurements and data analysis, as well as contributed to the formulation of the manuscript which contains the main results of this Chapter and has been published in *Applied Physics Letters*, volume **90**, 143501 (2007) [52].

6.1 Concept

Dye bleaching, i.e. dye degradation due to optical pumping, resulting in limited device lifetimes is in general considered a major disadvantage of organic dyes as active laser medium. Typically, the problem of dye bleaching is addressed by employing a continuous convective flow of liquid-dissolved dye molecules, compensating the bleaching dynamics caused by the external optical pump.

In optofluidic dye lasers and light sources, the required convective dye-replenishing flow has been achieved by external fluid handling apparatus (syringe pumps) [6,31–33,36–38,40,41,43,44], on-chip microfluidic pumps [42, 105], or by means of capillary effect [Chapter 5], [45,46]. In order to facilitate compact optofluidic dye laser systems suitable for commercial applications, simplification of fluidic handling is necessary, omitting the need for fluidic handling apparatus such as syringe pumps, hoses, fittings, valves, etc.

In this Chapter a novel dye replenishment mechanism based on diffusion is proposed. The concept may potentially allow the operation of optofluidic dye lasers for days without the need for a convective flow. The key concept in this is very similar to the entire paradigm behind miniaturized chemical-analysis systems where scaling arguments are used to show the attractiveness of micron-scale analytical devices compared to their macroscopic counterparts [1, 2].

The local dye bleaching dynamics which is characteristic in optofluidic dye lasers is investigated. Based on the findings, a dye replenishment mechanism is proposed which takes advantage of the classical diffusion present when dye molecules are dissolved in a liquid and placed in a microfluidic device. The bleaching of dye molecules by the optical pump will introduce gradients in the concentration of non-bleached dye molecules $c(\mathbf{r}, t)$, thus activating the diffusion mechanism associated with the thermally driven Brownian motion of the dye molecules. The bleaching-diffusion dynamics is modeled by a classical diffusion-convection equation with an additional drain (sink) term

$$D\nabla^2 c(\mathbf{r}, t) = \frac{\partial}{\partial t}\, c(\mathbf{r}, t) + \mathbf{v} \cdot \nabla c(\mathbf{r}, t) + \Gamma(\mathbf{r})\, c(\mathbf{r}, t) \tag{6.1}$$

where Γ is the bleaching rate, D is the diffusion constant, and $\mathbf{v}$ is the velocity field of a possible flow. For R6G dye molecules dissolved in ethylene glycol, D is estimated to $D \sim 1.5 \times 10^{-11}\,\mathrm{m}^2/\mathrm{s}$ by taking an experimental value for R6G molecules in water [106] and scaling with the viscosity at 25°C, using the Stokes–Einstein relation. On average, the random walk transports a dye molecule approximately $\ell = 0.1$ mm in $t = \ell^2/D \sim 10$ min. For typical optical pumping levels and repetition rates this is estimated to be sufficient

to replenish bleached dye in a miniaturized dye laser. This statement is supported by both Eq. (6.1) as well as our experimental studies of a particular optofluidic device.

To analyze the bleaching-diffusion dynamics, a simple, idealized 1D model system is used, resembling the experimental setup outlined in Fig. 6.1. Consider the situation where the liquid-dissolved dye molecules of initial concentration c_0 are optically pumped through a narrow slit of width w covering a closed microfluidic channel of length L. With x being along the direction of the quasi-1D channel we can thus make the approximation

$$\Gamma(x) \simeq \Gamma_0 \, \Theta\left(w/2 - |x|\right) = \begin{cases} \Gamma_0 & , \quad -\frac{w}{2} < x < \frac{w}{2}, \\ 0 & , \quad \text{otherwise.} \end{cases} \tag{6.2}$$

where $\Theta(x)$ is the Heaviside step function with $\Theta(x) = 0$ for $x < 0$ and $\Theta(x) = 1$ for $x > 0$.

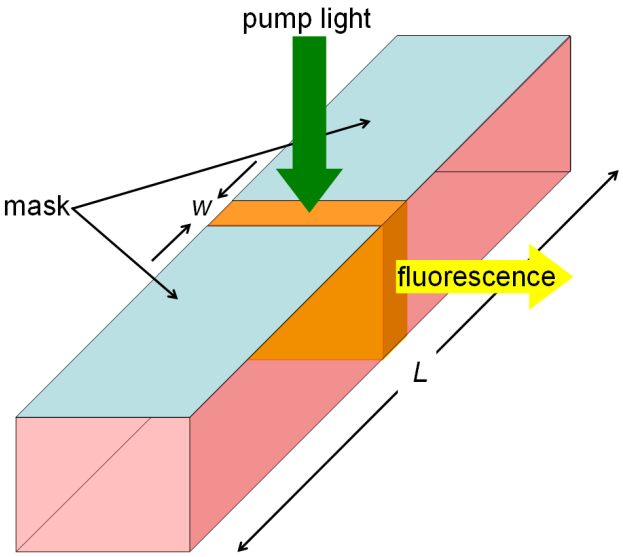

Fig. 6.1: Experimental setup. Closed channel containing a liquid solution of dye molecules. The dye molecules are optically pumped by a pulsed, frequency-doubled Nd:YAG laser through a slit of width w covering the sample.

6.2 Theory

The bleaching-diffusion dynamics may conveniently be understood by dimensional analysis. In the quasi-1D analysis, we use the notation $\nabla = \frac{\partial}{\partial x}$. Since the characteristic timescale is set by the inverse bleaching rate Γ_0^{-1} and the characteristic length scale by the slit width w, normalized variables for the time and position $\tilde{t}$ and $\tilde{x}$, respectively, are introduced as

$$\tilde{t} = \Gamma_0\, t\,; \qquad \tilde{x} = \frac{x}{w} \tag{6.3}$$

Using the chain rule, a change of variables of each of the derivatives of Eq. (6.1) is carried out

$$\nabla c = \frac{1}{w}\tilde{\nabla} c\,; \qquad \nabla^2 c = \frac{1}{w^2}\tilde{\nabla}^2 c\,; \qquad \frac{\partial c}{\partial t} = \Gamma_0 \frac{\partial c}{\partial \tilde{t}} \tag{6.4}$$

where the x, t dependence of c is omitted for clarity and $\tilde{\nabla} = \frac{\partial}{\partial \tilde{x}}$.

Expressing Eq. (6.1) in the normalized variables $\tilde{x}, \tilde{t}$ rather than x, t we arrive at the equation

$$\underbrace{\frac{D}{w^2}}_{\Gamma_D} \tilde{\nabla}^2 c(\tilde{x},\tilde{t}) = \Gamma_0 \frac{\partial}{\partial \tilde{t}}\, c(\tilde{x},\tilde{t}) + \underbrace{\frac{v}{w}}_{\Gamma_v} \tilde{\nabla} c(\tilde{x},\tilde{t}) + \Gamma_0\, \Theta\left(\frac{1}{2} - |\tilde{x}|\right)\, c(\tilde{x},\tilde{t}) \tag{6.5}$$

from which a diffusion rate Γ_D and a convection rate Γ_v can be extracted as

$$\Gamma_D = \frac{D}{w^2}\,; \qquad \Gamma_v = \frac{v}{w} \tag{6.6}$$

which should be compared to the externally controlled bleaching rate Γ_0.

In macroscopic dye lasers one has $\Gamma_v \gg \Gamma_0 \gg \Gamma_D$ so that un-bleached dye molecules are supplied on a faster time scale than the bleaching. This strategy has been central to the so far reported optofluidic dye lasers.

However, the very different scaling of Γ_D and Γ_v with w offers an alternative and attractive replenishment mechanism in microfluidic systems. Usually the convective term $\mathbf{v} \cdot \nabla c$ is driving the replenishment, but if $\Gamma_D \gg \max(\Gamma_v, \Gamma_0)$ we have the freedom to completely turn off convection and entirely rely on diffusion. In this work we will emphasize diffusion and the convective term will be explicitly zero, i.e. $\mathbf{v} = 0$.

The initial dynamics is characterized by the absence of gradients and for $t \ll \Gamma_D^{-1}$ diffusion can be neglected. This yields the solution

$$c(t) \simeq c_0 \exp\left[-\Gamma_0\, t\right]\,; \qquad t \ll \Gamma_D^{-1}\,; \qquad |x| < w/2 \tag{6.7}$$

This exponential dynamics, with a characteristic time scale Γ_0^{-1}, is the major source of concern for the bleaching-defined lifetime of the device outlined in Fig. 6.1. However, the bleaching, expressed as $c \to 0$ for $t \gg \Gamma_0^{-1}$, may be compensated by diffusion which becomes efficient for $t \gtrsim \Gamma_D^{-1}$, i.e. for $t \gtrsim \Gamma_D^{-1}$ the decay will be governed by Γ_D rather than Γ_0. Eq. (6.1) is difficult to solve analytically, but the dynamics may easily be studied numerically in more detail.

Numerical solutions

Considering the symmetric bleaching configuration of Eq. (6.5) and disregarding convection by setting $v = 0$, the concentration will always have a minimum in the center of the slit. The bleaching-diffusion dynamics is governed by the following equation, only depending on the *ratio* of the diffusion and bleaching rates

$$\boxed{\frac{\Gamma_D}{\Gamma_0}\,\tilde{\nabla}^2 c(\tilde{x},\tilde{t}) = \frac{\partial}{\partial \tilde{t}}\,c(\tilde{x},\tilde{t}) + \Theta\left(\frac{1}{2} - |\tilde{x}|\right)\,c(\tilde{x},\tilde{t})} \tag{6.8}$$

The Heaviside step function Θ works as a switch which controls the bleaching in the slit. The insulating boundary condition can be formulated as

$$\left.\frac{\partial c}{\partial x}\right|_{x=\pm L/2} = 0 \qquad \text{(insulation)} \tag{6.9}$$

i.e. zero flux out of the ends of the channel.

Eq. (6.8) is solved by time-dependent finite-element simulations for a channel much longer than the slit width, $L \gg w$, for varying values of Γ_D relative to Γ_0 using Comsol Multiphysics 3.2 [57].

Fig. 6.2 shows the normalized concentration as a function of normalized distance $\tilde{x}$ for different values of the ratio Γ_D/Γ_0 at different times $\tilde{t}$ for a fixed geometry with $w = 0.02\,L$. The dashed lines indicate the initial homogeneous concentration c_0. As expected, the solutions are symmetric around the center of the slit $\tilde{x} = 0$ and the concentration decreases with time (also for $x = \pm L/2$). As Γ_D/Γ_0 is increased, the concentration outside the slit drops faster due to increased diffusion and the concentration within the slit maintains a higher level.

Fig. 6.3 shows the normalized concentration as a function of normalized time $\tilde{t}$ in the center of the slit ($x = \tilde{x} = 0$). As seen, the above analysis accounts well for the qualitative behavior found. Clearly, diffusion changes the dynamics away from the pure exponential bleaching (dashed curve) to a

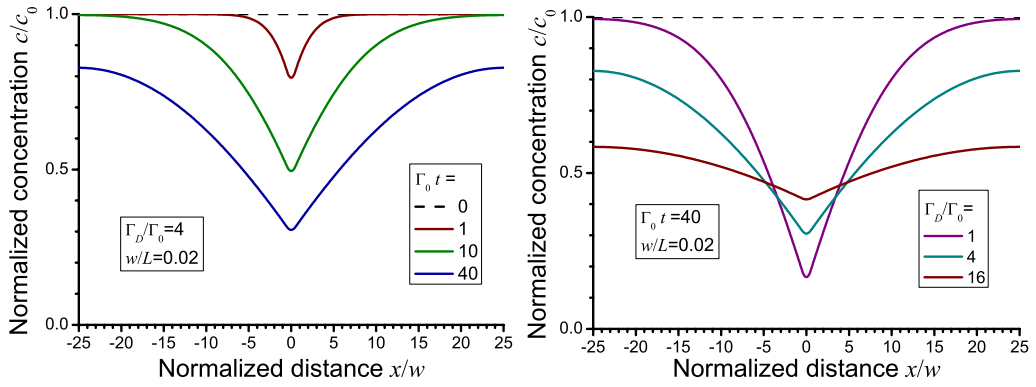

Fig. 6.2: Finite element simulation of bleaching-diffusion dynamics with $w = 0.02\,L$. **Left**: Concentration as a function of distance for different times (fixed $\Gamma_D/\Gamma_0 = 4$). **Right**: Concentration as a function of distance for different ratios Γ_D/Γ_0 (fixed time $\tilde{t} = \Gamma_0\, t = 40$.)

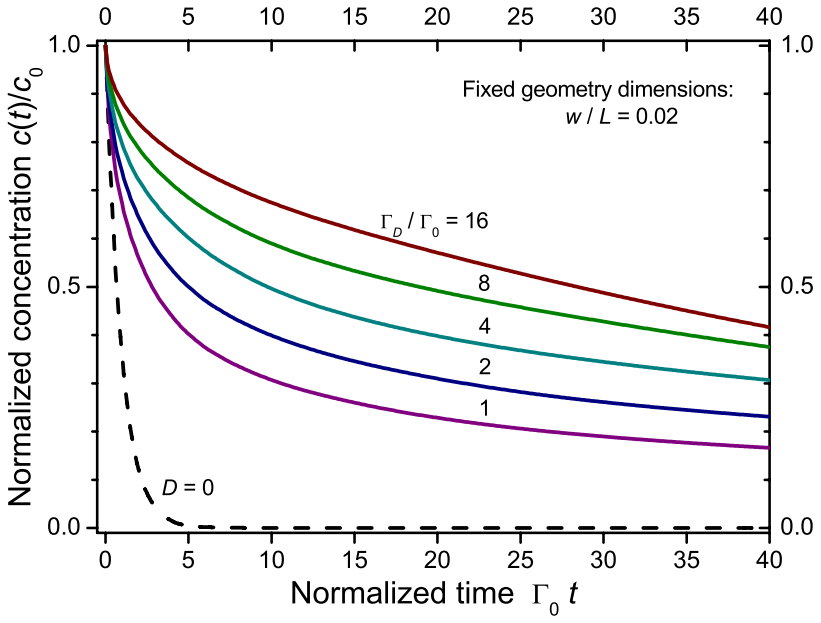

Fig. 6.3: Finite element simulation of bleaching-diffusion dynamics in the center of the slit ($x = \tilde{x} = 0$). The black dashed line shows the bare bleaching exponential decay, Eq. (6.7), in the absence of diffusion ($D = 0$), while the solid lines show the decay for an increasing value of the diffusion rate $\Gamma_D = D/w^2$.

situation with a much slower decay, thus potentially increasing the bleaching-limited lifetime of the device dramatically. As clearly seen, the presence of diffusion may considerably slow down the decay. The halving time $\tau_{1/2}$, i.e. $c(\tau_{1/2}) = c_0/2$, is increased by a factor of 4 for $\Gamma_D/\Gamma_0 = 1$ and a factor of 41 for $\Gamma_D/\Gamma_0 = 16$.

6.3 Dye bleaching experiment

The implicit hypothesis behind the above analysis is that the dye laser output signal somehow correlates with the concentration of un-bleached dye molecules. In order to verify our predictions experimentally we use the intensity of the fluorescence from a dye solution as an indirect measure of the local dye concentration in the optically pumped volume. The R6G dye solution is placed in a closed volume liquid channel and the fluorescence is measured under different optical pumping conditions.

Figure 6.4 shows the experimental setup, where the closed volume liquid channel is placed in a holder on a stage and optically pumped at 532 nm by a pulsed frequency doubled Nd:YAG laser (5 ns pulse duration, 10 Hz repetition rate). The closed volume liquid channel is constructed from a flexible polymer tube with an inner diameter of approximately 800 μm. The tube is filled with a dye solution of R6G dissolved in ethylene glycol with a concentration of $c_0 = 2 \times 10^{-4}$ mol/L and is closed at the ends by physical clamping, yielding a sealed tube length of 8 mm.

For the applied dye concentration level, the quantum efficiency has a weak dependency on the dye concentration, see Fig. 3.3 (page 47). According to the estimations of the penetration depth of the pump light in Tab. 3.1 (page 50) the penetration depth is comparable to the tube diameter. Thus, the dimensions of the closed volume liquid channel combined with the chosen dye concentration allow for measurements under experimental conditions where the pump energy distribution may be taken as constant over the total closed liquid channel volume, i.e. the pump light absorption is approximately constant in the dye solution of the closed volume.

The average optical pump pulse fluence is chosen to be 32 $\mu J/mm^2$ which is typical for optofluidic dye lasers operating well above threshold, see Tab. 1.1 (page 14) and Chapter 5. The fluorescence signal indicated in Fig. 6.1 is collected at an angle normal to the incident pump light by an optical fiber and measured by a fixed grating spectrometer (resolution 0.15 nm), see Fig. 6.4(c),(d).

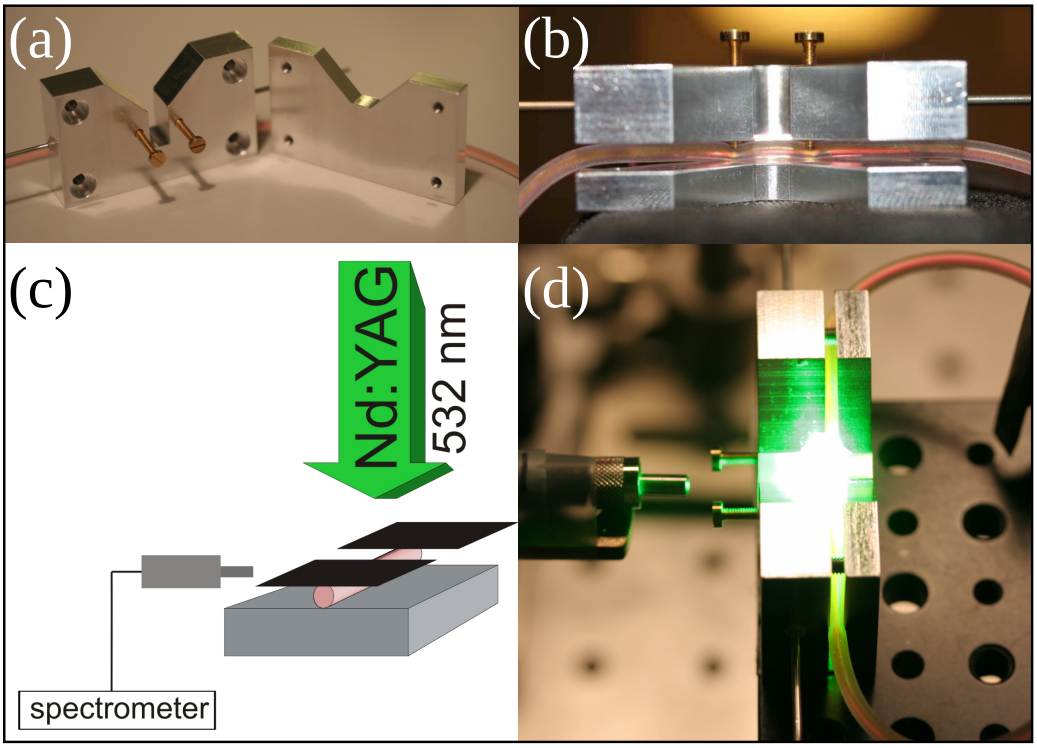

Fig. 6.4: Measurement setup. **(a)** Aluminum holder prior to assembly and flexible polymer tube in the background. **(b)** View of aluminium holder and flexible polymer tube in semi-closed liquid channel configuration. The screws which define the closed volume liquid channel are 10 mm apart. **(c+d)** The sample is placed on a stage and is pumped vertically at 532 nm by a frequency doubled Nd:YAG laser. The fluorescence signal is collected by an optical fiber and is measured by a fixed grating spectrometer.

6.4 Results

In the experiments, the decay of the fluorescence signal from the closed volume liquid channel is studied for two different optical pumping configurations:

(i) Spatially homogeneous pumping of the closed volume liquid channel.

(ii) Spatially inhomogeneous pumping of only the central part of the closed volume liquid channel through a narrow slit.

Figure 6.5 shows the temporal decay of the integrated spectrally broad fluorescence signal for different optical pumping configurations. For spatially

homogeneous optical pumping (no slit, $w/L = 1$), the data show an initial fast decay, followed by a much slower decay with a characteristic decay time of

$$\Gamma_0^{-1} = 5.0 \text{ hours } = 2 \times 10^4 \text{ s} \tag{6.10}$$

obtained from a fit to the data using a double exponential function.

The behavior of an initial fast decay followed by a slow decay does not arise from pump laser fluctuations nor from changes in the spectral output pattern of the device. When pumping through a slit ($w/L < 1$), the fast decay remains and the rate of the slow decay decreases with w. The fast decay may be attributed to initial consumption of oxygen in the fluid which is involved in the bleaching of the dye, as speculated in [89].

In the case of $w/L = 0.04$ ($w \sim 300\,\mu\text{m}$), a quasi stable output level on the timescale of days is observed. The experimentally observed fluorescence

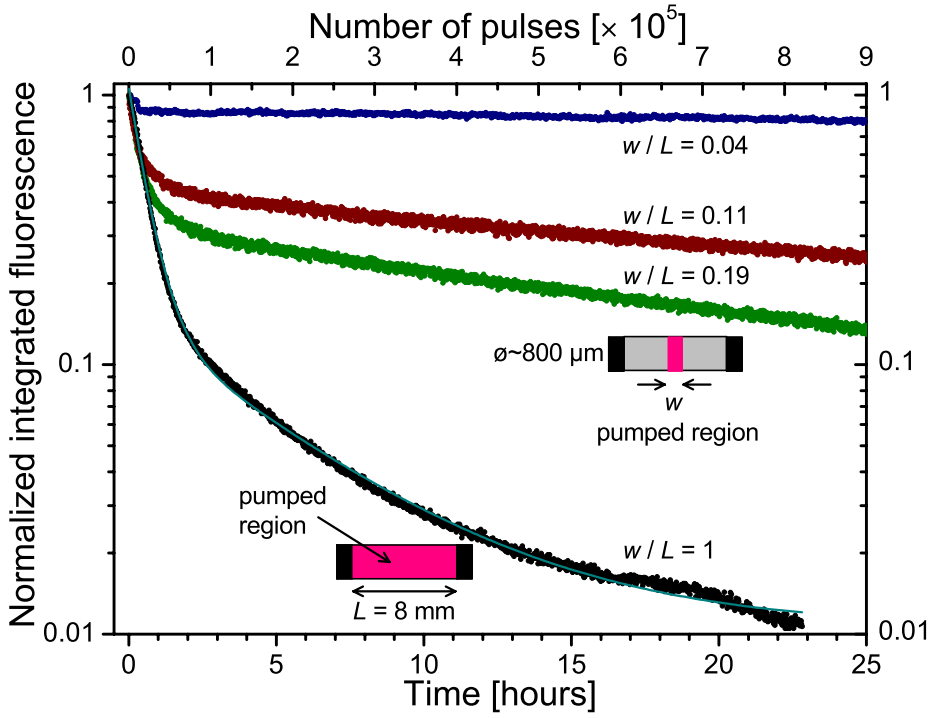

Fig. 6.5: Temporal decay of fluorescence for different optical pumping configurations. The lower curve ($w/L = 1$) is for spatially homogeneous pumping while the upper curves correspond to spatially inhomogeneous pumping through slits of varying width w. In the case of $w/L = 0.04$, the fluorescence signal is nearly constant on the timescale of days after a short initial decay (first 25 hours shown).

w [μm]	Γ_D [s^{-1}]	ν [Hz]
1000	2×10^{-5}	4
100	2×10^{-3}	400
10	0.2	40×10^3

Tab. 6.1: Diffusion rate and maximum repetition rate for different slit widths w, calculated by means of $\Gamma_D = D/w^2$ and $\nu = 2 \times 10^5 \, \Gamma_D$. A characteristic lifetime of 2×10^5 pulses is assumed, based on experiments, see Fig. 6.5.

dynamics is in qualitative agreement with the bleaching-diffusion dynamics found in the quasi-1D model, see Fig. 6.3.

The measurement of the bleaching rate $\Gamma_0 = 0.5 \times 10^{-4} \, s^{-1}$, corresponding to 2×10^5 pulses, allows for a comparison with the diffusion rate Γ_D for different slit widths. The diffusion rate Γ_D would be comparable to Γ_0 for a slit of macroscopic width $w \sim 1\,mm$. For a micron-scale slit of width $w \sim 100\,\mu m$, however, the diffusion rate increases by one order of magnitude to $\Gamma_D \sim 10^{-3} \, s^{-1}$. Table 6.1 shows the calculated diffusion rates for different slit widths w, and the maximum achievable repetition rates ν under the condition $\Gamma_D = \Gamma_0$ through the relation $\nu = 2 \times 10^5 \, \Gamma_D$. Laser devices employing a $\sim$10 μm wide slit can potentially be operated at kHz repetition rates enabling quasi-continuous wave applications, such as flow cytometry [107].

The order-of-magnitude estimates of Γ_D relative to Γ_0 illustrate the importance of the w^{-2}-scaling of Γ_D and support our proposal of miniaturized optofluidic dye lasers with $\Gamma_D \gg \Gamma_0$, thus fully avoiding any need for external fluidic handling systems such as syringe pumps or complicated on-chip pumping schemes. Optofluidic devices such as the one presented here provide a typical level of output power that is more than sufficient for use as an on-chip light source in lab-on-a-chip applications [14].

6.5 Summary

In this Chapter, the bleaching and diffusion dynamics in optofluidic dye lasers caused by local bleaching of the laser dye is investigated. A novel dye replenishment mechanism for optofluidic light sources is proposed based on diffusion of dye molecules alone, omitting the need for external fluid handling apparatus or on-chip microfluidic pumping devices. A simple quasi-1D diffusion model is used to explore the characteristic evolution of the local un-bleached dye concentration in the optically pumped or bleached volume of the device.

In the absence of convective flow, the asymptotic decay of the local dye concentration in the optically pumped volume is governed by the diffusion

rate and the resulting lifetime of the device is mainly limited by the capacity of the fluidic reservoirs. Generic microfluidic platforms typically allow for device layouts with a large volume ratio between the fluidic reservoir and the region being optically pumped.

In order to put our proposal in perspective, a reservoir with a volume of the order 1 cm^3, with an optically pumped volume of 2.5×10^{-7} cm^3 as in [89] and a bleaching rate of $\Gamma_0 \sim 10^{-4}\,s^{-1}$, would in principle allow for continuous operation for more than a thousand years for typical pumping levels and repetition rates. The implicit hypothesis behind the analysis is that the concentration of un-bleached molecules somehow correlates with the intensity of emitted light from the device under investigation. The conclusions drawn from the simple model are supported by basic experiments.

In the dye bleaching experiments, a closed volume liquid channel of length $L = 8$ mm is constructed from a flexible polymer tube and filled with a dye solution. The dye solution is optically pumped and the fluorescence signal is measured for different optical pumping configurations.

For spatially homogeneous pumping of the closed volume liquid channel, an initial fast decay in fluorescence is observed, followed by a much slower decay with characteristic decay time $\Gamma_0^{-1} = 5.0$ hours $= 2 \times 10^4$ s. When pumping only the central part of the closed volume liquid channel through a narrow slit of width w, the characteristic time of the slow decay dramatically increases. In the case of $w/L = 0.04$, the fluorescence signal is approximately constant on the timescale of days, in qualitative agreement with the quasi-1D model.

The investigations reveal the possibility that optofluidic dye laser devices may potentially be operated for days by diffusion without the need for a convective flow. Relying on diffusion rather than convection to generate the necessary dye replenishment significantly simplifies optofluidic dye laser device layouts, omitting the need for cumbersome and costly external fluidic handling or on-chip microfluidic pumping devices.

7. CONCLUSION

This thesis concerns optofluidic dye lasers suitable for integration onto a lab-on-a-chip platform. The work has consisted of design, fabrication, characterization, and modeling of the devices with a focus on:

(i) Reducing the threshold fluence for lasing.

(ii) Increasing the wavelength tunability.

(iii) Simplifying the fluidic handling of the devices.

The basic theory and materials used for optofluidic dye lasers have been presented. A transmission matrix model for design of optofluidic DFB lasers has been developed. The cavity modes of an optofluidic dye ring laser are studied using FEM simulations and compared to a ray-tracing model. The chosen laser dye R6G and polymer materials SU-8 and PMMA are introduced, with emphasis on their optical properties.

The development of CEUL in SU-8 has enabled fast and flexible fabrication of nanostructures and sub-wavelength optical structures in materials suitable for polymer planar waveguides and integrated optics. CEUL is capable of reliably fabricating 100 nm lines with 380 nm period in SU-8 on the wafer-scale. Micrometer scale features are easily added through an UV exposure step with no significant additional cost. The fabrication of NIL stamps by CEUL and pattern transfer into SiO_2 has been demonstrated. Optofluidic DFB dye lasers have been fabricated at DTU using CEUL in SU-8, followed by adhesive polymer-mediated wafer bonding.

Threshold and tunability

For the fabricated optofluidic DFB dye lasers, points (i)+(ii) have been addressed by employing a third order Bragg grating DFB laser resonator with a central $\pi/2$ phase shift and period of approximately $\Lambda \sim 600$ nm. The laser devices have been characterized by infiltrating the resonator with a dye solution by means of capillary action and optical pumping at 532 nm by a pulsed frequency doubled Nd:YAG laser.

The third order Bragg grating DFB laser resonator yields efficient wavelength selection and narrow linewidth emission (< 0.15 nm) has been obtained, with the linewidth measurement limited by the resolution of our spectrometer. The low grating order provides low out-of-plane scattering which enables a low threshold fluence for lasing. Threshold fluences down to ~ 7 μJ/mm^2 have been demonstrated. Due to the small height of the nanofluidic channels, most of the pump light is not absorbed, and the effective threshold fluence may be considerably lower.

Further, a low order Bragg grating has a large FSR, enabling a large wavelength tunability. A wavelength tunability of 45 nm has been demonstrated, limited by the spectral width of the gain of the chosen laser dye. The optofluidic wavelength tuning was achieved through coarse-tuning by varying the grating period and fine-tuning by altering the dye solution refractive index. A refractive index wavelength tunability of 7.69 nm has been demonstrated.

Fluidic handling

Point (iii) has been addressed in two ways. In the fabricated optofluidic DFB dye lasers, the dye replenishing fluid flow is mediated by capillary action, omitting the need for external fluid handling apparatus. A long meandering channel in connection with the laser resonator provides the dye-replenishing flow. The bottom of the channels is of SiO_2 which is highly hydrophilic and facilitates filling of the channels with a wide variety of fluids such as water, ethanol, ethylene glycol, and refractive index matching fluids. Due to the nature of capillary flow, the flow rate decreases with time and the chip is not easily emptied, rendering the devices suitable for single-use applications.

The second approach concerns a novel dye replenishment mechanism based on diffusion of dye molecules alone. Using this concept, no external fluid handling apparatus or on-chip microfluidic pumps are needed. The optofluidic light source is simply loaded with a dye solution which is optically pumped through a narrow slit of width w. As dye molecules in the slit region are bleached, they are replaced by un-bleached molecules through diffusion. As the dye diffusion rate scales as w^{-2}, the dye replenishment rate is dramatically increased relative to the bleaching rate for micrometer scale slits. The lifetime of the devices, which can be on the timescale of days, is mainly limited by the capacity of the fluidic reservoirs. A natural extension of this work would be to develop an optofluidic dye laser employing diffusive dye replenishment.

Outlook: Improvements and applications

In addition to the device characterization performed in this thesis work, the fabricated optofluidic DFB dye lasers could be characterized by accurately measuring the spectral shape and linewidth using a high-resolution spectrometer. This would allow for a determination of the quality factor of the laser resonator.

Other useful characterization data include the slope efficiency which could be determined through calibrated measurements of the laser output power using a highly sensitive power meter. Further, by combining the laser with a couple of waveguides, integrated Mach-Zehnder interferometers could be realized in order to measure the coherence length of the laser light. Further, this type of device could be used as an interference-based sensor [79].

Confinement of light

Although three important themes of optofluidic dye lasers have been addressed in this thesis, there is naturally still room for improvement. From a design point of view, the biggest issue is the lack of waveguiding in the fluidic resonator segments which gives rise to losses, as calculated in Chapter 5.5. The losses could be reduced by employing a scheme to achieve waveguiding in the fluidic resonator segments. Such liquid-core waveguiding would require either a dye-dissolvable liquid of higher refractive index than the top and bottom cladding layers, i.e. $n > 1.49$, or top and bottom cladding layers of lower refractive indices than the liquid.

PDMS has a low refractive index, $n = 1.406$, which is lower than that of e.g. ethylene glycol, and has been used to demonstrate liquid-core optofluidic DFB dye lasers oscillating on the $m = 5, 14, 15$ order Bragg reflection wavelength [37, 38, 105]. However, fabrication of sub-wavelength structures in PDMS, such as the third order Bragg gratings demonstrated in this thesis work, remains a technical challenge due to collapse of the PDMS structures [105]. Further, the hydrophobic nature of PDMS, see Tab. 5.1 (page 73), dramatically limits the number of suitable liquids. In this context, the issue of dye replenishment in PDMS-based nanochannels may be addressed by employing diffusive dye replenishment.

Stronger confinement of light in the fluidic resonator segments may be achieved with the presently used materials by reducing the dimensions of the resonator segments [39]. Since SU-8 can be structured using standard clean room fabrication techniques, this could be achieved by e.g. combined nanoimprint and photolithography (CNP) [95,108]. First order Bragg gratings could be realized using this parallel fabrication technique, thus eliminating out-of-

plane scattering losses, cf. Chapter 2.2.

Photonic crystal structures could provide efficient 2D lateral confinement, as opposed to the present gratings. Optofluidic photonic crystal laser devices could be realized by CNP in SU-8 followed by adhesive polymer-mediated wafer bonding. Recently, optofluidic tuning of both passive photonic crystal structures [9] and polymer photonic crystal band edge lasers [108] have been demonstrated.

In addition to the reduction of losses, stronger confinement of light could lead to a better general theoretical understanding of laser oscillation in the resonator structure.

Applications

The fabricated optofluidic dye lasers are suitable for integration with other polymer or microfluidic components onto lab-on-a-chip systems [14]. The applications of such systems are mainly in optical sensing in chemistry and biochemistry where tunable, coherent light in the visible range is desired [13].

Integrated sensors could rely on absorption, evanescent field, intra-cavity, or interference effects [18, 19]. Even a sensor concept where the emission direction of a laser device is altered, has been proposed [108]. For a biosensor device to be competitive with existing technologies, the challenges of sensitivity and specificity must be addressed. The required specificity may be achieved through surface functionalization by positioning specific receptor molecules on the sensing surface.

Optofluidic dye lasers could be applied in nanofluidics, e.g. for excitation or detection of stained single DNA molecules in nanochannels. In such systems [109], optofluidic dye lasers could easily be integrated with the nanofluidic network on the chip and deliver coherent light locally to regions of interest.

Arrays of optofluidic dye lasers could be used for on-chip multi-wavelength spectroscopy [38, 110]. Such laser arrays operating at high repetition rates could be applied in multi-color flow cytometry [107].

Other applications include adaptive optical devices where the flexible nature of liquids can be used to alter the optical properties of the device. Also, devices for shaping and shortening of light pulses using an absorbing dye as saturable absorber [111, 112] are promising applications of optofluidic dye lasers.

REFERENCES

[1] A. Manz, N. Graber, and H. M. Widmer. Miniaturized total chemical-analysis systems – a novel concept for chemical sensing. *Sens. Actuator B: Chem.*, 1:244–248, 1990.

[2] D. Janasek, J. Franzke, and A. Manz. Scaling and the design of miniaturized chemical-analysis systems. *Nature*, 442(7101):374 – 380, 2006.

[3] Demetri Psaltis, Stephen R. Quake, and Changhuei Yang. Developing optofluidic technology through the fusion of microfluidics and optics. *Nature*, 442:381–386, 2006.

[4] C. Monat, P. Domachuk, and B. J. Eggleton. Integrated optofluidics: A new river of light. *Nat. Photon.*, 1(2):106 – 114, 2007.

[5] Uriel Levy and Romi Shamai. Tunable optofluidic devices. *Microfluid. Nanofluid.*, 4:97–105, 2008.

[6] Brian Bilenberg, Torben Rasmussen, Søren Balslev, and Anders Kristensen. Real-time tunability of chip-based light source enabled by microfluidic mixing. *J. Appl. Phys.*, 99:023102, 2006.

[7] Daniel B. Wolfe, Richard S. Conroy, Piotr Garstecki, Brian T. Mayers, Michael A. Fischbach, Kateri E. Paul, Mara Prentiss, and George M. Whitesides. Dynamic control of liquid-core/liquid-cladding optical waveguides. *Proc. Natl. Acad. Sci. U. S. A.*, 101:12434–12438, 2004.

[8] Sindy K. Y. Tang, Brian T. Mayers, Dmitri V. Vezenov, and George M. Whitesides. Optical waveguiding using thermal gradients across homogeneous liquids in microfluidic channels. *Appl. Phys. Lett.*, 88:061112, 2006.

[9] David Erickson, Troy Rockwood, Teresa Emery, Axel Scherer, and Demetri Psaltis. Nanofluidic tuning of photonic crystal circuits. *Opt. Lett.*, 31:59–61, 2006.

[10] Xin Heng, David Erickson, L. Ryan Baugh, Zahid Yaqoob, Paul W. Sternberg, Demetri Psaltis, and Changhuei Yang. Optofluidic microscopy – a method for implementing a high resolution optical microscope on a chip. *Lab. Chip*, 6:1274–1276, 2006.

[11] P. Domachuk, M. Cronin-Golomb, B. J. Eggleton, S. Mutzenich, G. Rosengarten, and A. Mitchell. Application of optical trapping to beam manipulation in optofluidics. *Opt. Express*, 13:7265–7275, 2005.

[12] Martin Schadt. Liquid crystal materials and liquid crystal displays. *Annu. Rev. Mater. Sci.*, 27:305–379, 1997.

[13] E. Verpoorte. Chip vision – optics for microchips. *Lab. Chip*, 3:42N–52N, 2003.

[14] S. Balslev, A. M. Jorgensen, B. Bilenberg, K. B. Mogensen, D. Snakenborg, O. Geschke, J. P. Kutter, and A. Kristensen. Lab-on-a-chip with integrated optical transducers. *Lab. Chip*, 6:213–217, 2006.

[15] B. Bilenberg, M. Hansen, D. Johansen, V. Ozkapici, C. Jeppesen, P. Szabo, I. M. Obieta, O. Arroyo, J. O. Tegenfeldt, and A. Kristensen. Topas-based lab-on-a-chip microsystems fabricated by thermal nanoimprint lithography. *J. Vac. Sci. Technol. B*, 23:2944–2949, 2005.

[16] J. C. Galas, C. Peroz, Q. Kou, and Y. Chen. Microfluidic dye laser intracavity absorption. *Appl. Phys. Lett.*, 89:224101, 2006.

[17] L. Lading, L. B. Nielsen, and T. Sevel. Comparing biosensors. In *Proceedings of IEEE Sensors 2002*, volume 1, pages 229–232. Institute of Electrical and Electronics Engineers, New York, 2002.

[18] B. Kuswandi, Nuriman, J. Huskens, and W. Verboom. Optical sensing systems for microfluidic devices: A review. *Anal. Chim. Acta*, 601:141–155, 2007.

[19] David Erickson, Sudeep Mandal, Allen H. J. Yang, and Bernardo Cordovez. Nanobiosensors: optofluidic, electrical and mechanical approaches to biomolecular detection at the nanoscale. *Microfluid. Nanofluid.*, 4:33–52, 2008.

[20] Zhenyu Li and Demetri Psaltis. Optofluidic dye lasers. *Microfluid. Nanofluid.*, 4:145–158, 2008.

[21] T. H. Maiman. Stimulated optical radiation in ruby. *Nature*, 187(4736):493–494, 1960.

[22] P. P. Sorokin and J. R. Lankard. Stimulated emission observed from an organic dye chloro-aluminum phthalocyanine. *IBM J. Res. Develop.*, 10:162–163, 1966.

[23] C. V. Shank. Physics of dye lasers. *Rev. Mod. Phys.*, 47:649–657, 1975.

[24] F. P. Schäfer (editor). *Dye Lasers*. Springer-Verlag, Berlin Heidelberg, third edition, 1990.

[25] P. P. Sorokin and J. R. Lankard. Flashlamp excitation of organic dye lasers – a short communication. *IBM J. Res. Develop.*, 11:148, 1967.

[26] H. Kogelnik and C. V. Shank. Stimulated emission in a periodic structure. *Appl. Phys. Lett.*, 18:152–154, 1971.

[27] C. V. Shank, J. E. Bjorkholm, and H. Kogelnik. Tunable distributed-feedback dye laser. *Appl. Phys. Lett.*, 18:395–396, 1971.

[28] H. Kogelnik and C. V. Shank. Coupled-wave theory of distributed feedback lasers. *J. Appl. Phys.*, 43:2327–2335, 1972.

[29] M. Nakamura, A. Yariv, H. W. Yen, S. Somekh, and H. L. Garvin. Optically pumped GaAs surface laser with corrugation feedback. *Appl. Phys. Lett.*, 22:515–516, 1973.

[30] M. Nakamura, H. W. Yen, A. Yariv, E. Garmire, and S. Somekh. Laser oscillation in epitaxial GaAs waveguides with corrugation feedback. *Appl. Phys. Lett.*, 23:224–225, 1973.

[31] B. Helbo, A. Kristensen, and A. Menon. A micro-cavity fluidic dye laser. *J. Micromech. Microeng.*, 13:307–311, 2003.

[32] B. Helbo, S. Kragh, B. G. Kjeldsen, J. L. Reimers, and A. Kristensen. Investigation of the dye concentration influence on the lasing wavelength and threshold for a micro-fluidic dye laser. *Sens. Actuator A: Phys.*, 111(1):21 – 25, 2004.

[33] S. Balslev and A. Kristensen. Microfluidic single mode laser using high order bragg grating and antiguiding segments. *Opt. Express*, 13(1):344–351, 2005.

[34] Klaus B. Mogensen, Jamil El-Ali, Anders Wolff, and Jörg P. Kutter. Integration of polymer waveguides for optical detection in microfabricated chemical analysis systems. *Appl. Opt.*, 42(19):4072–4079, 2003.

[35] D. Nilsson, S. Balslev, and A. Kristensen. A microfluidic dye laser fabricated by nanoimprint lithography in a highly transparent and chemically resistant cyclo-olefin copolymer (coc). *J. Micromech. Microeng.*, 15(2):296–300, 2005.

[36] D. V. Vezenov, B. T. Mayers, R. S. Conroy, G. M. Whitesides, P. T. Snee, Y. Chan, D. G. Nocera, and M. G. Bawendi. A low-threshold, high-efficiency microfluidic waveguide laser. *J. Am. Chem. Soc.*, 127(25):8952–8953, 2005.

[37] Z. Li, Z. Zhang, T. Emery, A. Scherer, and D. Psaltis. Single mode optofluidic distributed feedback dye laser. *Opt. Express*, 14(2):696–701, 2006.

[38] Zhenyu Li, Zhaoyu Zhang, Axel Scherer, and Demetri Psaltis. Mechanically tunable optofluidic distributed feedback dye laser. *Opt. Express*, 14:10494–10499, 2006.

[39] P. Lalanne and M. Hutley. Artificial media optical properties – subwavelength scale. In *Encyclopedia of Optical Engineering*, pages 62–71. Dekker, New York, 2003. DOI: 10.1081/E-EOE-120009537.

[40] Y. Cheng, K. Sugioka, and K. Midorikawa. Microfluidic laser embedded in glass by three-dimensional femtosecond laser microprocessing. *Opt. Lett.*, 29:2007–2009, 2004.

[41] M. Gersborg-Hansen, S. Balslev, N. A. Mortensen, and A. Kristensen. A coupled cavity micro fluidic dye ring laser. *Microelectron. Eng.*, 78-79:185–189, 2005.

[42] J. C. Galas, J. Torres, M. Belotti, Q. Kou, and Y. Chen. Microfluidic tunable dye laser with integrated mixer and ring resonator. *Appl. Phys. Lett.*, 86:264101, 2005.

[43] Q. Kou, I. Yesilyurt, and Y. Chen. Collinear dual-color laser emission from a microfluidic dye laser. *Appl. Phys. Lett.*, 88:091101, 2006.

[44] Ch. Peroz, J-C. Galas, L. Le Gratiet, and Y. Chen. Compact dye laser on a chip fabricated by ultraviolet nanoimprint lithography. *Appl. Phys. Lett.*, 89:243109, 2006.

[45] A. E. Vasdekis, G. E. Town, G. A. Turnbull, and I. D. W. Samuel. Fluidic fibre dye lasers. *Opt. Express*, 15(7):3962–3967, 2007.

[46] Siyka I. Shopova, Hongying Zhou, Xudong Fan, and Po Zhang. Optofluidic ring resonator based dye laser. *Appl. Phys. Lett.*, 90:221101, 2007.

[47] C. Karnutsch, M. Stroisch, M. Punke, U. Lemmer, J. Wang, and T. Weimann. Laser diode-pumped organic semiconductor lasers utilizing two-dimensional photonic crystal resonators. *IEEE Photonics Technol. Lett.*, 9–12:741–743, 2007.

[48] M. Gersborg-Hansen, S. Balslev, and N. A. Mortensen. Finite-element simulation of cavity modes in a micro-fluidic dye ring laser. *J. Opt. A: Pure Appl. Opt.*, 8:17–20, 2006.

[49] M. Gersborg-Hansen, L. H. Thamdrup, A. Mironov, and A. Kristensen. Combined electron beam and uv lithography in su-8. *Microelectron. Eng.*, 84:1058–1061, 2007.

[50] Morten Gersborg-Hansen and Anders Kristensen. Optofluidic third order distributed feedback dye laser. *Appl. Phys. Lett.*, 89:103518, 2006.

[51] M. Gersborg-Hansen and A. Kristensen. Tunability of optofluidic distributed feedback dye lasers. *Opt. Express*, 15:137 – 142, 2007.

[52] Morten Gersborg-Hansen, Søren Balslev, Niels Asger Mortensen, and Anders Kristensen. Bleaching and diffusion dynamics in optofluidic dye lasers. *Appl. Phys. Lett.*, 90:143501, 2007.

[53] R. G. Hunsperger. *Integrated Optics: Theory and Technology*. Springer-Verlag, Berlin Heidelberg, fifth edition, 2002.

[54] L. A. Coldren and S. W. Corzine. *Diode lasers and photonic integrated circuits*. John Wiley & Sons, New York, 1995.

[55] Søren Balslev. *Polymer dye lasers*. PhD thesis, Technical University of Denmark, January 2006. ISBN 87-89935-82-9. Available at `www.mic.dtu.dk/ak`.

[56] Jonathan P. Dowling, Michael Scalora, Mark J. Bloemer, and Charles M. Bowden. The photonic band edge laser: A new approach to gain enhancement. *J. Appl. Phys.*, 75(4):1896–1899, 1994.

[57] Comsol support and Femlab/Comsol Multiphysics documentation, `www.comsol.com`.

[58] J. D. Joannopoulos, R. D. Meade, and J. N. Winn. *Photonic Crystals: Molding the Flow of Light*. Princeton University Press, Princeton, 1995.

[59] J. Jin. *The Finite Element Method in Electromagnetics*. Wiley–IEEE press, New York, second edition, 2002.

[60] R. R. Birge and F. J. Duarte. *Kodak Laser Dyes*. Eastman Kodak Company, Rochester, NY 14650, 1987. Kodak publication JJ-169.

[61] C. Bojarski and E. Grabowska. Photoluminescence decay and quantum yield studies for rhodamine 6g in ethanol. *Acta Phys. Pol. A*, 60(3):397–406, 1981.

[62] F. L. Arbeloa, P. R. Ojeda, and I. L. Arbeloa. The fluorescence quenching mechanisms of rhodamine 6g in concentrated ethanolic solution. *J. Photochem. Photobiol. A: Chem.*, 45(3):313–323, 1988.

[63] T. Govindanunny and B. M. Sivaram. Solvent effects on the gain of rhodamine 6g. *Appl. Phys.*, 23(3):253–258, 1980.

[64] N. V. Korol'kova, A. I. Akimov, L. K. Denisov, and B. M. Uzhinov. Lasing efficiency of solutions of rhodamine dyes in different solvents. *Journal of Applied Spectroscopy*, 39(3):1022–1027, 1983. Translated from Zhurnal Prikladnoi Spektroskopii, 39(3): 406–412, 1983.

[65] I. Lopez Arbeloa and K. K. Rohatgi-Mukherjee. Solvent effect on photophysics of the molecular forms of rhodamine b. solvation models and spectroscopic parameters. *Chem. Phys. Lett.*, 128(5–6):474–479, 1986.

[66] T. R. Griffiths and D. C. Pugh. Solvent polarity studies. part 1. new z-values and relationships with other solvent polarity scales. *J. Solut. Chem.*, 8(3):247–258, 1979.

[67] P. Crozet and Y. Meyer. Rhodamine 6g laser in aqueous solution. *Comptes Rendus Hebdomadaires des Séances de l'Académie des Sciences Série B*, 271(14):718–721, 1970. In French.

[68] N. V. Korol'kova, L. K. Denisov, B. M. Uzhinov, and V. Yu. Traskin. Improvement in the laser efficiency of aqueous solutions of rhodamine 6g. *Journal of Applied Spectroscopy*, 33(2):842–845, 1980. Translated from Zhurnal Prikladnoi Spektroskopii, 33(2): 286–289, 1980.

[69] Wikipedia, the free encyclopedia, 2007. `http://en.wikipedia.org`.

[70] P. C. Beaumont, D. G. Johnson, and B. J. Parsons. Photophysical properties of laser-dyes – picosecond laser flash-photolysis studies of rhodamine-6g, rhodamine-b and rhodamine-101. *J. Chem. Soc.: Faraday Trans.*, 89:4185–4191, 1993.

[71] David J. Griffiths. *Introduction to Electrodynamics*. Prentice Hall, third edition, 1999.

[72] N. LaBianca and J. D. Gelorme. High aspect ratio resist for thick film applications. In *Proceedings of SPIE*, volume 2438, pages 846–852, 1995.

[73] M. Despont, H. Lorenz, N. Fahrni, J. Brugger, P. Renaud, and P. Vettiger. High-aspect-ratio, ultrathick, negative-tone near-uv photoresist for mems applications. In *Proceedings of the Tenth IEEE Annual International Workshop on Micro Electro Mechanical Systems (MEMS '97)*, pages 518–522, Nagoya, 1997.

[74] H. Lorenz, M. Despont, N. Fahrni, N. LaBianca, P. Renaud, and P. Vettiger. Su-8: a low-cost negative resist for mems. *J. Micromech. Microeng.*, 7:121–124, 1997.

[75] Su-8 2000 permanent epoxy negative photoresist. processing guidelines for: Su-8 2000.5, su-8 2002, su-8 2005, su-8 2007, su-8 2010 and su-8 2015. Retrieved on October 30, 2007 from `www.microchem.com`.

[76] Louis J. Guerin. The su8 homepage. Retrieved on November 1, 2007 from `www.geocities.com/guerinlj`.

[77] K. K. Tung, W. H. Wong, and E. Y. B. Pun. Polymeric optical waveguides using direct ultraviolet photolithography process. *Appl. Phys. A*, 80:621–626, 2005.

[78] A. Borreman, S. Musa, A. A. M. Kok, M. B. J. Diemeer, and A. Driessen. Fabrication of polymeric multimode waveguides and devices in su-8 photoresist using selective polymerization. In *Proceedings of the IEEE/LEOS Symposium Benelux Chapter*, pages 83–86, Amsterdam, the Netherlands, December 9 2002.

[79] B. Y. Shew, C. H. Kuo, Y. C. Huang, and Y. H. Tsai. Uv-liga interferometer biosensor based on the su-8 optical waveguide. *Sens. Actuator A: Phys.*, 120:383–389, 2005.

[80] B. Bilenberg, T. Nielsen, B. Clausen, and A. Kristensen. Pmma to su-8 bonding for polymer based lab-on-a-chip systems with integrated optics. *J. Micromech. Microeng.*, 14:814–818, 2004.

[81] W. C. Hu, K Sarveswaran, M Lieberman, and G. H. Bernstein. Sub-10 nm electron beam lithography using cold development of poly(methylmethacrylate). *J. Vac. Sci. Technol. B*, 22(4):1711–1716, 2004.

[82] Nano pmma and copolymer. Data for 950 kDa PMMA. Retrieved on October 31, 2007 from `www.microchem.com`.

[83] S. Y. Chou, P. R. Krauss, W. Zhang, L. J. Guo, and L. Zhuang. Sub-10 nm imprint lithography and applications. *J. Vac. Sci. Technol. B*, 15(6):2897–2904, 1997.

[84] S. M. Sze. *Semiconductor devices: Physics and Technology*. John Wiley & Sons, New York, 1985.

[85] P. Rai-Choudhury (editor). *Handbook of Microlithography, Micromachining, and Microfabrication. Volume 1: Microlithography.* SPIE Press Monograph, Volume PM39, 1997. Chapter 2 on electron beam lithography is available online at `www.cnfusers.cornell.edu/cnf_spietoc.html`.

[86] A. K. Nallani, Sang Won Park, and Jeong Bong Lee. Characterization of su-8 as a resist for electron-beam lithography. In *Proceedings of SPIE*, volume 5116, pages 414–423, 2003.

[87] Mirwais Aktary, Martin O. Jensen, Kenneth L. Westra, Michael J. Brett, and Mark R. Freeman. High-resolution pattern generation using the epoxy novolak su-8 2000 resist by electron beam lithography. *J. Vac. Sci. Technol. B*, 21:L5–L7, 2003.

[88] A. Pepin, V. Studer, D. Decanini, and Y. Chen. Exploring the high sensitivity of su-8 resist for high resolution electron beam patterning. *Microelectron. Eng.*, 73-74:233–237, 2004.

[89] S. Balslev, T. Rasmussen, P. Shi, and A. Kristensen. Single mode solid state distributed feedback dye laser fabricated by gray scale electron beam lithography on a dye doped su-8 resist. *J. Micromech. Microeng.*, 15:2456–2460, 2005.

[90] B. Bilenberg, S. Jacobsen, M. S. Schmidt, L. H. D. Skjolding, P. Shi, P. Boggild, J. O. Tegenfeldt, and A. Kristensen. High resolution 100 kv electron beam lithography in su-8. *Microelectron. Eng.*, 83:1609–1612, 2006.

[91] B. Bilenberg, M. Scholer, P. Shi, M. S. Schmidt, P. Boggild, M. Fink, C. Schuster, F. Reuther, C. Gruetzner, and A. Kristensen. Comparison of high resolution negative electron beam resists. *J. Vac. Sci. Technol. B*, 24:1776–1779, 2006.

[92] T. F. Krauss, R. M. de la Rue, and S. Brand. Two-dimensional photonic-bandgap structures operating at near-infrared wavelengths. *Nature*, 383:699–702, 1996.

[93] P. I. Borel, L. H. Frandsen, A. Harpoth, M. Kristensen, J. S. Jensen, and O. Sigmund. Topology optimised broadband photonic crystal y-splitter. *Electron. Lett.*, 41:69–71, 2005.

[94] SU-8 formulation 2002 from MicroChem. Corp., `www.microchem.com`, diluted with pure cyclopentanone to a 13 wt% solid content solution.

[95] L. J. Guo. Recent progress in nanoimprint technology and its applications. *J. Phys. D: Appl. Phys.*, 37(11):R123–R141, 2004.

[96] M. Beck, M. Graczyk, I. Maximov, E.-L. Sarwe, T. G. I. Ling, M. Keil, and L. Montelius. Improving stamps for 10 nm level wafer scale nanoimprint lithography. *Microelectron. Eng.*, 61-62:441–448, 2002.

[97] mr-I T85 from micro resist technology GmbH, `www.microresist.de`.

[98] Xunli Zhang and Stephen J. Haswell. Materials matter in microfluidic devices. *MRS Bull.*, 31:95–99, 2006.

[99] Microetcher II, Danville Engineering, `www.daneng.com`.

[100] M. Nordström, R. Marie, M. Calleja, and A. Boisen. Rendering su-8 hydrophilic to facilitate use in micro channel fabrication. *J. Micromech. Microeng.*, 14:1614–1617, 2004.

[101] N. R. Tas, J. Haneveld, H. V. Jansen, M. Elwenspoek, and A. van den Berg. Capillary filling speed of water in nanochannels. *Appl. Phys. Lett.*, 85(15):3274–3276, 2004.

[102] F. Persson, L. H. Thamdrup, M. B. L. Mikkelsen, S. E. Jaarlgard, P. Skafte-Pedersen, H. Bruus, and A. Kristensen. Double thermal oxidation scheme for the fabrication of sio_2 nanochannels. *Nanotechnology*, 18:245301, 2007.

[103] Henrik Bruus. *Theoretical Microfluidics*. Oxford Master Series in Physics number 18. Oxford University Press, Oxford, 2007.

[104] H. J. W. M. Hoekstra, G. J. M. Krijnen, and P. V. Lambeck. Efficient interface conditions for the finite-difference beam propagation method. *J. Lightwave Technol.*, 10(10):1352–1355, 1992.

[105] Zhenyu Li and Demetri Psaltis. Optofluidic distributed feedback dye lasers. *IEEE J. Sel. Topics Quantum Electron.*, 13(2):185–193, 2007.

[106] R. Rigler, Ü. Mets, J. Widengren, and P. Kask. Fluorescence correlation spectroscopy with high count rate and low-background – analysis of translational diffusion. *Eur. Biophys. J. Biophys. Lett.*, 22(3):169 – 175, 1993.

[107] Stephen C. de Rosa, Leonard A. Herzenberg, Leonore A. Herzenberg, and Mario Roederer. 11-color, 13-parameter flow cytometry: Identification of human naive t cells by phenotype, function, and t-cell receptor diversity. *Nat. Med.*, 7:245–248, 2001.

[108] Felipe Bernal Arango, Mads Brøkner Christiansen, Morten Gersborg-Hansen, and Anders Kristensen. Optofluidic tuning of photonic crystal band edge lasers. *Appl. Phys. Lett.*, 91:223503, 2007.

[109] Walter Reisner, Jason P. Beech, Niels B. Larsen, Henrik Flyvbjerg, Anders Kristensen, and Jonas O. Tegenfeldt. Nanoconfinement-enhanced conformational response of single dna molecules to changes in ionic environment. *Phys. Rev. Lett.*, 99:058302, 2007.

[110] Yuji Oki, Shinichi Miyamoto, Mitsuo Maeda, and Nilesh J. Vasa. Multiwavelength distributed-feedback dye laser array and its application to spectroscopy. *Opt. Lett.*, 27:1220–1222, 2002.

[111] Mitsuo Maeda, Yuji Oki, and Katsumi Imamura. Ultrashort pulse generation from an integrated single-chip dye laser. *IEEE J. Quantum Electron.*, 33:2146–2149, 1997.

[112] Yuji Oki, Katsuya Ohno, and Mitsuo Maeda. Tunable ultrashort pulse generation from a waveguided laser with premixed-dye-doped plastic film. *Jpn. J. Appl. Phys.*, 37:6403–6407, 1998.

APPENDIX

A. LIST OF PUBLICATIONS

International peer-reviewed journal publications

1. **M. Gersborg-Hansen**, S. Balslev, N. A. Mortensen, and A. Kristensen. A coupled cavity micro fluidic dye ring laser. *Microelectron. Eng.*, 78–79:185–189, 2005.

2. **M. Gersborg-Hansen**, S. Balslev, and N. A. Mortensen. Finite-element simulation of cavity modes in a micro-fluidic dye ring laser. *J. Opt. A: Pure Appl. Opt.*, 8:17–20, 2006.

3. **M. Gersborg-Hansen**, L. H. Thamdrup, A. Mironov, and A. Kristensen. Combined electron beam and UV lithography in SU-8. *Microelectron. Eng.*, 84:1058–1061, 2007.

4. **M. Gersborg-Hansen** and A. Kristensen. Optofluidic third order distributed feedback dye laser. *Appl. Phys. Lett.*, 89:103518, 2006.

5. **M. Gersborg-Hansen** and A. Kristensen. Tunability of optofluidic distributed feedback dye lasers. *Opt. Express*, 15:137–142, 2007.

6. **M. Gersborg-Hansen**, S. Balslev, N. A. Mortensen, and A. Kristensen. Bleaching and diffusion dynamics in optofluidic dye lasers. *Appl. Phys. Lett.*, 90:143501, 2007.

7. F. Bernal Arango, M. B. Christiansen, **M. Gersborg-Hansen**, and A. Kristensen. Optofluidic tuning of photonic crystal band edge lasers. *Appl. Phys. Lett.*, 91:223503, 2007.

INDEX